

AD-A123 947

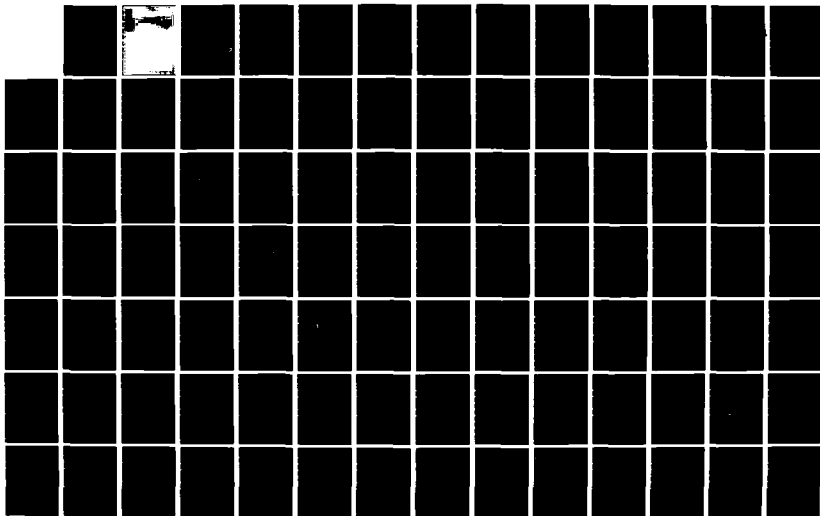
THEORETICAL STUDIES OF HIGH FIELD TRANSPORT IN III-V  
SEMICONDUCTORS(U) ILLINOIS UNIV AT URBANA COORDINATED  
SCIENCE LAB H SHICHIJO SEP 80 R-893 N00014-79-C-0424

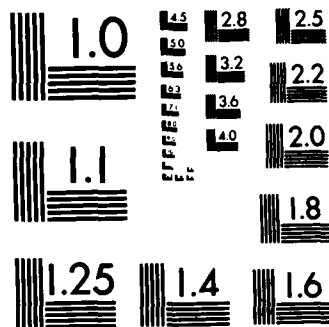
1/2

UNCLASSIFIED

F/G 20/12

NL





MICROCOPY RESOLUTION TEST CHART  
NATIONAL BUREAU OF STANDARDS-1963-A

REPORT DOCUMENTATION PAGE		READ INSTRUCTIONS BEFORE COMPLETING FORM
1. REPORT NUMBER	2. GOVT ACCESSION NO. AD - A123947	3. RECIPIENT'S CATALOG NUMBER
4. TITLE (and Subtitle)  THEORETICAL STUDIES OF HIGH FIELD TRANSPORT IN III-V SEMICONDUCTORS		5. TYPE OF REPORT & PERIOD COVERED  Technical Report
7. AUTHOR(s)  Hisashi Shichijo		6. PERFORMING ORG. REPORT NUMBER R-893, UIU-80-2225
9. PERFORMING ORGANIZATION NAME AND ADDRESS Coordinated Science Laboratory University of Illinois at Urbana-Champaign Urbana, Illinois 61801		8. CONTRACT OR GRANT NUMBER(s)  N00014-79-C-0424 N00014-79-C-0768
11. CONTROLLING OFFICE NAME AND ADDRESS  Joint Services Electronics Program		10. PROGRAM ELEMENT, PROJECT, TASK AREA & WORK UNIT NUMBERS
14. MONITORING AGENCY NAME & ADDRESS (if different from Controlling Office)		12. REPORT DATE September, 1980
		13. NUMBER OF PAGES 164
		15. SECURITY CLASS. (of this report)  Unclassified
		15a. DECLASSIFICATION/ DOWNGRADING SCHEDULE
16. DISTRIBUTION STATEMENT (of this Report)  Approved for public release, distribution unlimited.		
17. DISTRIBUTION STATEMENT (of the abstract entered in Block 20, if different from Report)		
18. SUPPLEMENTARY NOTES		
19. KEY WORDS (Continue on reverse side if necessary and identify by block number)  High field transport, 3-5 semiconductors, Monte Carlo simulation		
20. ABSTRACT (Continue on reverse side if necessary and identify by block number)  Two theoretical aspects of high field transport in III - V semiconductors have been studies. First, a new mechanism to obtain negative differential resistance in a GaAs-AlGaAs multilayered structure is described. The mechanism is based on the transfer of electrons in real space from a high mobility GaAs region to an adjacent low mobility AlGaAs region when a high electric field is applied parallel to the interface. It is analogous in many respects to the Gunn effect, except that this mechanism allows greater		

20. (contd.)

control of device characteristics. These characteristics can be adjusted by varying the doping densities, the layer thicknesses, and the Al mole fraction in the AlGaAs.

The mechanism is analyzed using the electron temperature model and the Monte Carlo simulation. The electron temperature model is exact in the high carrier density limit, whereas the Monte Carlo method is valid in the low density limit. Both methods clearly illustrate the degree of control possible with this mechanism over device characteristics. Comparisons are made between the two models. Miscellaneous effects which are neglected in the models are discussed. These include two-dimensional effects, band bending, statistical fluctuation, and quantum mechanical transmission at the interface. Switching characteristics have been analyzed, and the switching time is estimated to be approximately  $1 \times 10^{-12}$  sec. This fast transfer mechanism is attractive for microwave, switching and memory devices.

The second portion of the present work deals with the band structure dependence of high field transport and impact ionization in GaAs. An understanding of impact ionization is important because of its influence on the performance of avalanche photodetectors and IMPATT diodes. It also determines the ultimate performance limits of small semiconductor devices, such as CCDs and FETs.

A realistic band structure has been included in a Monte Carlo simulation of high field transport in GaAs. The band structure has been calculated using the empirical pseudopotential method. Partly due to the lack of information and partly for simplicity, we have made simplifying assumptions on the phonon scattering rate, the ionization threshold, and the ionization probability. Unlike previous theories of impact ionization, the method requires, in principle, no adjustable parameters as long as the band structure and the scattering mechanisms are known. The calculated drift velocity, mean free path, and impact ionization rate are in fair agreement with the experimental data. It is found that the contribution of ballistic electrons to the impact ionization rate is negligibly small. Within statistical uncertainty, we do not observe the anisotropy of the electron ionization rate in contradiction to the recent experimental results. Based on the results of the simulation, a general discussion of impact ionization is given.

UILU-ENG 80-2225

THEORETICAL STUDIES OF HIGH FIELD TRANSPORT  
IN III-V SEMICONDUCTORS

by

Hisashi Shichijo

This work was supported in part by the Joint Services Electronics  
Program (U.S. Army, U.S. Navy and U.S. Air Force) under Contract N00014-79-C-0424  
and in part by the Offices of Naval Research under Contract N00014-79-C-0768.

Reproduction in whole or in part is permitted for any purpose of the  
United States Government

Approved for public release. Distribution unlimited.



Accession For	
NTIS GRA&I	<input checked="checked" type="checkbox"/>
DTIC TAB	<input type="checkbox"/>
Unannounced	<input type="checkbox"/>
Justification	
By	
Distribution/	
Availability Codes	
Dist	Avail and/or Special
A	

THEORETICAL STUDIES OF HIGH FIELD TRANSPORT  
IN III-V SEMICONDUCTORS

BY

HISASHI SHICHIJO

B.E., University of Tokyo, 1976  
M.S., University of Illinois, 1978

THESIS

Submitted in partial fulfillment of the requirements  
for the degree of Doctor of Philosophy in Electrical Engineering  
in the Graduate College of the  
University of Illinois at Urbana-Champaign, 1980

Urbana, Illinois

- i -

THEORETICAL STUDIES OF HIGH FIELD TRANSPORT  
IN III - V SEMICONDUCTORS

Hisashi Shichijo, Ph.D.  
Coordinated Science Laboratory  
and  
Department of Electrical Engineering

Two theoretical aspects of high field transport in III - V semiconductors have been studied. First, a new mechanism to obtain negative differential resistance in a GaAs-AlGaAs multilayered structure is described. The mechanism is based on the transfer of electrons in real space from a high mobility GaAs region to an adjacent low mobility AlGaAs region when a high electric field is applied parallel to the interface. It is analogous in many respects to the Gunn effect, except that this mechanism allows greater control of device characteristics. These characteristics can be adjusted by varying the doping densities, the layer thicknesses, and the Al mole fraction in the AlGaAs.

The mechanism is analyzed using the electron temperature model and the Monte Carlo simulation. The electron temperature model is exact in the high carrier density limit, whereas the Monte Carlo method is valid in the low density limit. Both methods clearly illustrate the degree of control possible with this mechanism over device characteristics. Comparisons are made between the two models. Miscellaneous effects which are neglected in the models are discussed. These include two-dimensional effects, band bending, statistical fluctuation, and quantum mechanical transmission at the interface. Switching characteristics have been analyzed, and the switching time is estimated to be approximately  $1 \times 10^{-12}$  sec. This fast transfer mechanism is attractive for microwave, switching, and memory devices.

The second portion of the present work deals with the band structure dependence of high field transport and impact ionization in GaAs. An understanding of impact ionization is important because of its influence on the performance of avalanche photodetectors and IMPATT diodes. It also determines the ultimate performance limits of small semiconductor devices, such as CCDs and FETs.

A realistic band structure has been included in a Monte Carlo simulation of high field transport in GaAs. The band structure has been calculated using the empirical pseudopotential method. Partly due to the lack of information and partly for simplicity, we have made simplifying assumptions on the phonon scattering rate, the ionization threshold, and the ionization probability. Unlike previous theories of impact ionization, the method requires, in principle, no adjustable parameters as long as the band structure and the scattering mechanisms are known. The calculated drift velocity, mean free path, and impact ionization rate are in fair agreement with the experimental data. It is found that the contribution of ballistic electrons to the impact ionization rate is negligibly small. Within statistical uncertainty we do not observe the anisotropy of the electron ionization rate in contradiction to the recent experimental results. Based on the results of the simulation, a general discussion of impact ionization is given.



## ACKNOWLEDGEMENTS

The author would like to express his sincere appreciation to his thesis advisor, Professor Karl Hess, for introducing him to work on high field transport. His continual guidance, encouragement, and insight have been invaluable.

Special thanks also go to Professor E. G. Streetman for his helpful discussions and advice and for contributing many ideas to the problem of real space transfer.

The author is indebted to Professors T. H. Glisson, J. R. Hauser, and M. A. Littlejohn of North Carolina State University (Raleigh) for doing some of the Monte Carlo simulations and for their many valuable discussions. Without their assistance on the Monte Carlo program this work would not have been possible.

The author is grateful to Professor N. Holonyak, Jr. for his early guidance, helpful discussions and interest. He also thanks Professor G. E. Stillman for his valuable discussions on experimental aspect of impact ionization and his interest.

He is grateful to Professors J. D. Dow, M. Altarelli, Doctors O. F. Saukey, and H. Hjarlmarson for their helpful discussions on the band structure.

Special thanks go to J. D. Oberstar for his proofreading of the thesis, helpful comments, and good humor.

For their cooperation and assistance the author is grateful to M. Keever and J. Y. Tang.

He wishes to thank the staff members at CSL computer facility, and Mrs. V. Metze at MRL computer facility for their assistance in the use of DEC-10 and DEC-20.

The expert technical assistance of R. MacFarlane and R. T. Gladin is gratefully acknowledged. The author appreciates the typing provided by S. Brennecke and E. M. Kesler.

Financial support provided by the Joint Services Electronics Program (Contract No. N00014-79-C-0424) and by the Office of Naval Research (Contract No. N00014-79-C-0768) is gratefully acknowledged.

The author wishes to thank Professor T. Sugano of the University of Tokyo for his encouragement and interest.

For their continual support, patience, and encouragement he is thankful to his parents.

Finally, the author dedicates this work to his loving wife, Rie. Her love and understanding have made this work possible.

## TABLE OF CONTENTS

Chapter	Page
1. INTRODUCTION . . . . .	1
2. REAL SPACE ELECTRON TRANSFER IN GaAs-Al <sub>x</sub> Ga <sub>1-x</sub> As HETEROSTRUCTURES . . . . .	4
2.1 General Discussion . . . . .	4
2.2 Electron Temperature Model . . . . .	9
2.2.1 Description of the model . . . . .	9
2.2.2 Calculations . . . . .	10
2.2.3 Results . . . . .	15
2.2.4 Comparisons with the Gunn effect . . . . .	18
2.2.5 Influence of material parameters on the real space transfer . . . . .	21
2.3 Monte Carlo Simulation of Real Space Electron Transfer . . . . .	28
2.3.1 Introduction . . . . .	28
2.3.2 Simulation procedure . . . . .	29
2.3.3 Results . . . . .	33
2.3.4 Comparisons with the electron temperature model . . . . .	50
2.4 Two-dimensional Effects . . . . .	51
2.4.1 Size quantization . . . . .	51
2.4.2 Polar optical scattering in two dimensions . . . . .	53
2.4.3 Influence on the real space transfer mechanism . . . . .	56
2.5 Miscellaneous Effect . . . . .	58
2.5.1 Band bending . . . . .	58
2.5.2 Transmission coefficient at the interface . . . . .	61
2.5.3 Statistical fluctuation . . . . .	63

Chapter	Page
2.6 Switching Characteristics . . . . .	64
2.7 Summary . . . . .	69
3. BAND STRUCTURE DEPENDENT TRANSPORT AND IMPACT IONIZATION IN GaAs . . . . .	73
3.1 Introductory Remarks . . . . .	73
3.2 Summary of Experimental Results . . . . .	75
3.3 Previous Theories of Impact Ionization . . . . .	78
3.4 Band Structure of GaAs . . . . .	80
3.5 Ballistic Electron Transport and Phonon Scattering . . . . .	88
3.6 Simulation Method . . . . .	96
3.7 Results . . . . .	101
3.7.1 Contribution of ballistic electrons . . . . .	101
3.7.2 Transport properties and ionization rate . . . . .	104
3.8 Summary . . . . .	121
4. CONCLUSIONS . . . . .	124
REFERENCES . . . . .	125
APPENDIX 1. Total Scattering Rate and Angular Dependences of Various Scattering Mechanisms . . . . .	135
APPENDIX 2. Material Parameters Used in the Calculations . . . . .	159
APPENDIX 3. Wave Vector Relations . . . . .	161
VITA . . . . .	164

## 1. INTRODUCTION

The field of hot electron physics is now more than thirty years old. Following earlier work on dielectric breakdown in insulators, Shockley[1], in 1951, initiated experimental investigation of hot carrier effects in semiconductors. In the 60's the field saw one of its peaks with the prediction and the discovery of the Gunn effect. The historical background which led to this discovery is described by Hilsum in his excellent paper[2]. The recent revival of interest in this field is due to hot carrier effects which occur in submicron silicon MOSFETs and GaAs FETs. Oxide breakdown, hot electron emission from silicon into the gate-oxide, velocity overshoot, and ballistic transport in GaAs FETs are examples of such effects.

Among all the semiconductors the III-V compounds rank only behind silicon in technological importance, and are second to none with respect to basic research interests. One of the unique properties of the III-V semiconductors is their band structure which makes possible the construction of transferred electron devices (TEDs)[3]. The fascinating idea of electrons transferring in momentum space from one valley to another has attracted many physicists and engineers[2]. Another interesting property of III-V semiconductors is that they can be epitaxially grown lattice-matched to each other when proper binary, ternary or quaternary alloys are employed. This property has been fully utilized in optoelectronics devices. From the viewpoint of carrier transport, heterostructures can provide an entire new class of devices with unusual transport properties. The concept of a "superlattice" first proposed by Esaki and Tsu[4] in 1969 is one such example. It is expected that in the

future more and more heterostructures will be utilized in various semiconductor devices.

It is possible, for example, to realize electron transfer in real space utilizing heterostructures as proposed by Hess and co-workers[5]. The mechanism is basically analogous to the Gunn effect in momentum space. As a matter of fact, when the Gunn effect was discovered in 1963, the possibility of a similar effect in real space was on the minds of several scientists[6]. The actual realization, however, had to wait for the evolution of the molecular beam epitaxy (MBE) technique and the concept of modulation doping[4,7]. The real space transfer mechanism is based on the thermionic emission of hot electrons from the high mobility GaAs layer to the low mobility AlGaAs layer in the presence of a high electric field. This transfer leads to a negative differential resistance (NDR) just as in the Gunn effect. The advantage of the real space transfer mechanism, however, lies in its degree of control of device characteristics. Negative differential effects are important for their possible applications to microwave, switching, and memory devices. The present work also aims to contribute generally to the theory of high field transport in semiconductor heterostructures. Additionally, the theoretical techniques used to study this effect gives us the understanding and the tools to attack another interesting problem of semiconductor physics — the rigorous treatment of impact ionization in semiconductors.

Impact ionization is a very important hot carrier effect. It directly influences the performance of avalanche photodetectors[3] and IMPATT diodes[9]. It also determines the ultimate performance limits of small semiconductor devices, such as CCDs[10] and FETs[11]. Nevertheless, the

previous theories of impact ionization have been limited by various assumptions and also by the use of several adjustable parameters, such as the scattering mean free path. The effective mass approximation and small non-parabolicity correction have been used in spite of the fact that carriers gain more than 1 eV in energy (as measured from the bottom of the conduction band). In our work we have attempted to include a realistic band structure in the Monte Carlo simulation of high field transport in GaAs. This method can calculate not only the impact ionization rate but also other quantities of interest, such as drift velocity and distribution functions. The inclusion of a realistic band structure is expected to expand our understanding of high field transport to extremely high electric fields .

In Chapter 2 the real space electron transfer mechanism is analyzed using the electron temperature model and the Monte Carlo technique. Then, various effects which are neglected in the analysis are described. Some comments will also be made on the application of this mechanism.

In Chapter 3 a new Monte Carlo method using a realistic band structure is described. The method is applied to the study of high field transport in GaAs. On this basis, a detailed study of the band structure dependence of impact ionization in GaAs is given.

## 2. REAL SPACE ELECTRON TRANSFER IN GaAs-Al<sub>x</sub>Ga<sub>1-x</sub>As HETEROSTRUCTURES

### 2.1 General Discussion

The basic structure consists of alternating GaAs-Al<sub>x</sub>Ga<sub>1-x</sub>As layers, or other appropriate lattice-matched materials with dissimilar band-gap energies and carrier mobilities. Typical layer dimensions are from 100 Å to a few tenths of a micron. Such structures have been realized by utilizing molecular beam epitaxial (MBE)[12-14], vapor phase epitaxial (VPE)[15,16], or liquid phase epitaxial (LPE)[17,18] growth techniques. In this work we are concerned with GaAs-Al<sub>x</sub>Ga<sub>1-x</sub>As multilayers. For  $0 < x < 0.45$  the  $\Gamma$  direct gap of Al<sub>x</sub>Ga<sub>1-x</sub>As changes as[19]

$$E_g^{\Gamma} = 1.424 + 1.247x \text{ (eV)}. \quad (2.1)$$

In GaAs-Al<sub>x</sub>Ga<sub>1-x</sub>As heterostructures approximately 88 % of this band gap discontinuity is in the conduction band[20]. The potential barriers form a rectangular potential well for electrons. At thermal equilibrium electrons reside at the minimum of the potential wells, i.e., in the GaAs layers. Application of a high electric field parallel to the layer interfaces of this structure will result in heating of the electrons. When the mean kinetic energy of the electrons becomes comparable to the potential barrier height,  $\Delta E$ , they can be thermionically emitted into the AlGaAs. If the mobility of electrons in the GaAs layer is much higher than the mobility in the AlGaAs layer, the sample should exhibit negative differential resistance (NDR).



To properly describe real space electron transfer, it is necessary to account for the scattering mechanisms encountered by electrons being transported at high kinetic energies in the potential well. A mechanical analogue to real space transfer is provided by the example of a ball rolling down a chute. The ball will stay in the chute if its kinetic energy remains small. However, if the ball gains adequate kinetic energy, then an obstacle can scatter the ball out of the chute. A similar effect occurs in a layered heterostructures, where electrons drift in a potential well under the influence of a high electric field.

In order to realize large difference of mobilities in two materials modulation doping[7,22] of the layers may be utilized. Fig. 2.1 schematically shows the band structure, doping distributions, and electron mobility of modulation-doped GaAs-Al<sub>x</sub>Ga<sub>1-x</sub>As layers. The AlGaAs layers are intentionally doped to a density of  $10^{17} \sim 10^{18} \text{ cm}^{-3}$ , whereas the GaAs layers contain only unintentional background impurities ( $10^{14} \sim 10^{15} \text{ cm}^{-3}$ ). At thermal equilibrium the electrons reside in the GaAs layers. When separated more than 200 Å these electrons experience strongly reduced impurity scattering. Hess has shown that the differential scattering rate due to ionized impurities decreases exponentially with spatial distance[23]. This mobility enhancement by spatial separation of electrons from donors was first proposed by Esaki and Tsu[4], and later verified experimentally by Dingle et al.[7]. They have observed a mobility of 5000  $\text{cm}^2/\text{Vsec}$  at 300 K, and even higher mobilities ( $\sim 15000 \text{ cm}^2/\text{Vsec}$ ) at low temperatures. The AlGaAs layers can be made strongly compensated, and thereby the mobility in these layers can be very low ( $\sim 500 \text{ cm}^2/\text{Vsec}$  or less). In this manner a mobility ratio of ten or more can be realized in modulation doped structures.

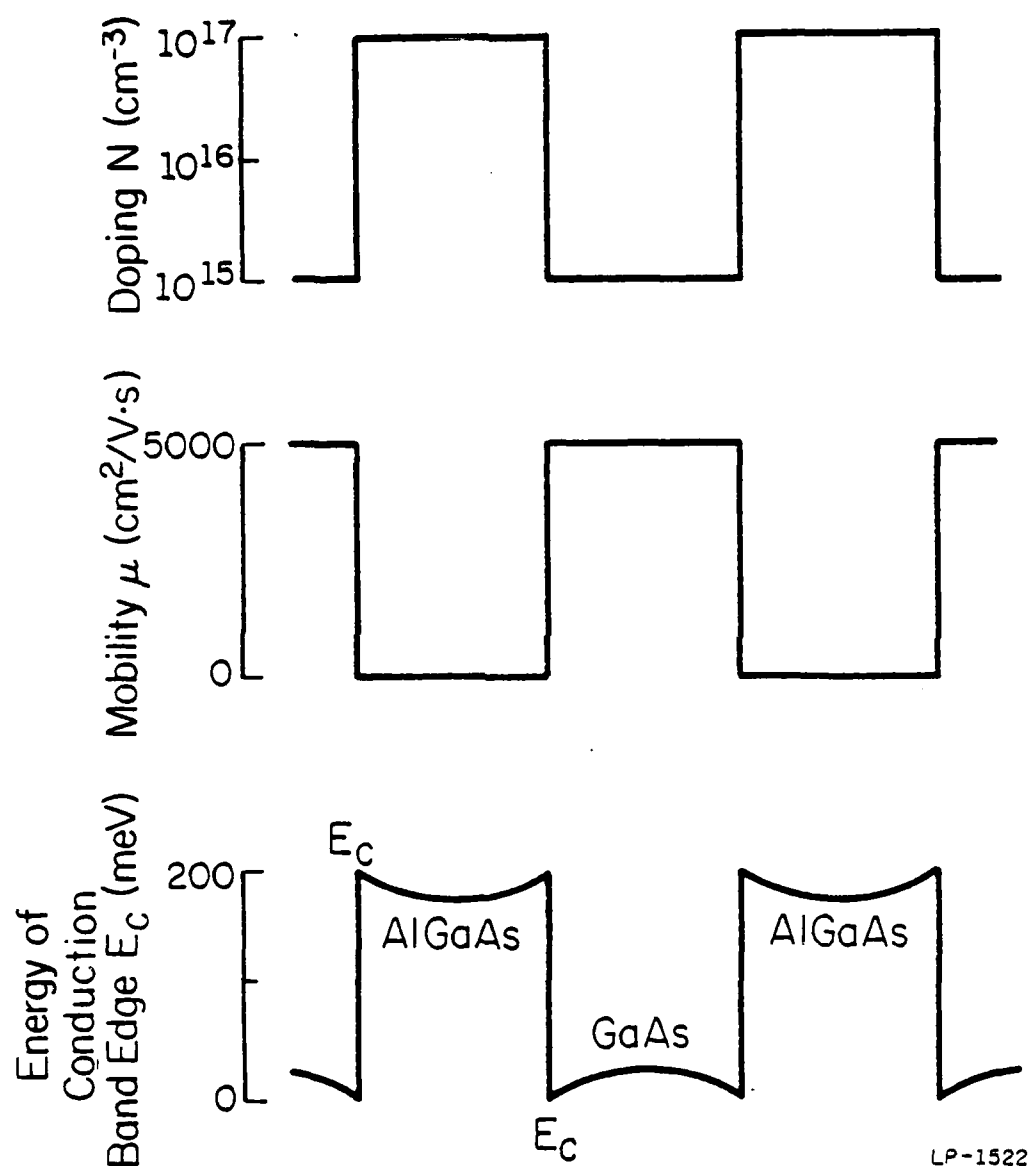


Fig. 2.1. Schematic diagrams of doping density, electron mobility, and conduction band energy of modulation-doped layers.

Since the carrier temperature is determined by the power balance equation:

$$e\mu F^2 = \frac{dE}{dt} \quad (2.2)$$

and the energy loss rates are similar in the two materials, the heating of carriers occurs only in the GaAs layer. These hot electrons transfer in space to the adjacent AlGaAs layers and then thermalize. Some of the cooler electrons in the AlGaAs layers can undergo reverse transfer into the GaAs layer. In order to take account of this energy and momentum exchange between the GaAs and the AlGaAs layers, one must solve the Boltzmann equation:

$$\frac{\partial f}{\partial t} + \frac{1}{\hbar} \vec{F} \cdot \vec{\nabla}_k f + \vec{v} \cdot \vec{\nabla}_r f = \frac{\partial f}{\partial t} \Big|_c \quad (2.3)$$

with appropriate boundary conditions. In addition to the spatial inhomogeneity of this system, there are several other factors which complicate the analysis:

- i) At high electric fields the energy distribution functions in polar semiconductors are highly non-Maxwellian.
- ii) There is an energy exchange between the layers because energetic carriers are flowing out of the GaAs and cold carriers are returning.
- iii) Electron-electron interactions must be taken into account.
- iv) The effects of higher L minima in two materials should be considered.
- v) There are several other effects which make the analysis

extremely difficult, such as two dimensional effects, band bending, reflection and trapping of electrons at the interfaces, etc.

To this end we have chosen two methods; the electron temperature model and the Monte Carlo method. The electron temperature model assumes nearly Maxwellian distributions in the two materials. The Monte Carlo method is a one particle simulation of electron transport in a simplified potential profile. Each method applies only under certain conditions. Detailed discussion of the two models, assumptions, and the results of the calculations are presented in the next two sections.

In both methods we have deliberately chosen typical layer widths larger than 400 Å. This avoids the complications arising from size quantization effect and other two dimensional effects. Some of the two dimensional effects are discussed in Section 2.4. The choice of large layer widths also allows the use of the semiclassical Boltzmann equation. Otherwise one must resort to a quantum mechanical treatment. With large layer widths, the potential fluctuations due to the statistical distribution of the impurities can also be neglected. Other simplifying assumptions in the models are taken up and reexamined in Section 2.5.

## 2.2 Electron Temperature Model[24]

### 2.2.1 Description of the model

In polar semiconductors the energy distribution of electrons can be highly non-Maxwellian, since polar optical scattering is inelastic and is not randomizing (see Fig. A.3 in Appendix 1). To make the analysis explicitly tractable, however, we assume a Maxwellian form for the isotropic part of the distribution function. This assumption is partly justified by the fact that the electron density is high in the GaAs layer at the start of the electron transfer, since the GaAs layer collects electrons from the neighboring AlGaAs layers. Typically the GaAs layer will have an electron density of  $10^{18} \sim 10^{19} \text{ cm}^{-3}$ . Electron-electron collisions will, therefore, randomize the energy gained in the electric field direction and establish a Maxwellian distribution. Above the band edge of the AlGaAs the electrons in the GaAs will follow a "cooler" distribution because of the reverse transfer of cooler electrons from the AlGaAs. This will be shown as a result of Monte Carlo simulations in Section 2.3.3 (Fig. 2.25). However, since the GaAs layer is sufficiently narrow, we can use a single electron temperature in the GaAs.

If there were no interaction between the GaAs and AlGaAs layers, the electron temperature in the AlGaAs layer would be constant and close to the lattice temperature,  $T_0$ . However, this is not a realistic assumption. Due to the transfer of hot electrons from the GaAs layer, electrons close to the GaAs layer will have considerably higher temperature than the lattice temperature. As electrons move away from the interface they thermalize to the equilibrium. Therefore, we need to consider the position dependence of the electron temperature in order to account for the power flow

perpendicular to the interface.

Fig. 2.2 shows the model used in the calculations. We assume a position-dependent electron temperature,  $T_L(x)$ , and a position-dependent quasi-Fermi level,  $E_{F2}(x)$ , in the AlGaAs layer. Similar methods have recently been employed by other workers to analyze thermionic emission in metal-GaAs contacts[25]. Both the concept of the electron temperature and of quasi-Fermi levels require high carrier densities in order to be valid. In the thin GaAs layer we assume a position-independent electron temperature,  $T_e$ , and quasi-Fermi level,  $E_{F1}$ . With this assumption we only need to solve the position dependence of the electron temperature and the quasi-Fermi level in the AlGaAs layers. The thermal conduction of hot electrons from the GaAs layer into the AlGaAs layers is then accounted for by the slope of  $T_L(x)$  at the interface boundary. Although at the boundary the slope of  $T_e$  in the GaAs layer is zero (since we have assumed  $T_e$  to be constant), we assume that the same amount of energy as given by the slope of  $T_L(x)$  is extracted from the GaAs.

### 2.2.2 Calculations

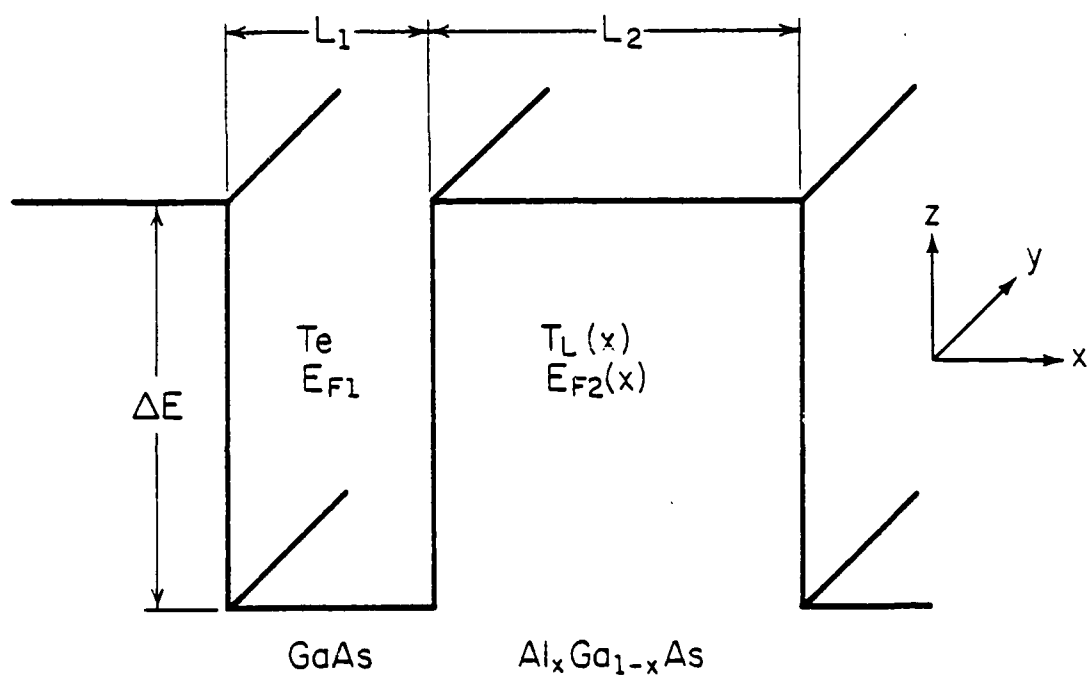
We proceed to assume a distribution function of a form:

$$f = f_0(\epsilon, x) + g(\epsilon, x)k_y + h(\epsilon, x)k_x, \quad (2.4)$$

where  $f_0(\epsilon, x)$  is a Maxwellian distribution:

$$f_0(\epsilon, x) = \exp\left[\frac{E_{F2}(x) - \epsilon}{kT_L(x)}\right] \quad (2.5)$$

in the AlGaAs layer. The coordinate system is shown in Fig. 2.2. The



LP-1539

Fig. 2.2. Simplified electron-temperature model with coordinate system used for the calculations.

electric field is in the y-direction. The second term of Eq. (2.4) represent the drift term of the distribution along the electric field as is usually used for a spatially uniform system[26]. The third term is to take into account the spatial nonuniformity. It represents the displacement of the distribution perpendicular to the electric field. This term is essential to account for the energy flow normal to the field direction. The isotropic part of the distribution function in the GaAs layer is given by a form similar to Eq. (2.5) in terms of  $T_e$  and  $E_{F1}$ , but without the position dependence.

As is normally done, we then separate the variables into equations for the spatially symmetric part and the drift terms[26]. The method of moments[27] is then utilized to obtain the differential equations for  $T_L(x)$  and  $E_{F2}(x)$ . The set of equations obtained is given below:

$$\begin{aligned} & \left( \frac{2\hbar\omega_o}{\pi m_2^*} \right)^{1/2} eE_o \frac{\exp(Z_o - Z_L) - 1}{\exp(Z_o) - 1} Z_L^{1/2} \exp(Z_L/2) K_o(Z_L/2) \\ & = e\mu_2 F^2 + \frac{5\mu_2}{2e} (kT_L)^{-3/2} \exp(-E_{F2}/kT_L) \frac{d^2}{dx^2} \left[ (kT_L)^{7/2} \exp(E_{F2}/kT_L) \right] \end{aligned} \quad (2.6)$$

and

$$\frac{d^2}{dx^2} \left[ (kT_L)^{5/2} \exp(E_{F2}/kT_L) \right] = 0 \quad (2.7)$$

where  $Z_L = \frac{kT_L}{\hbar\omega_o}$ ,  $Z_o = \frac{kT_o}{\hbar\omega_o}$ ,  $T_o$  is the lattice temperature,  $\mu_2$  is the mobility in the AlGaAs layer,  $F$  is the applied electric field, and  $K_o$  is the Bessel function of the zeroth order. The position dependences of  $E_{F2}(x)$  and  $T_L(x)$  have been omitted in the notations. The left side of Eq. (2.6) is the rate of energy loss due to polar optical scattering[26],



and the first term on the right side is the power input from the applied electric field. The second term on the right represents the energy flow from the GaAs due to the transfer of hot electrons. Applying energy conservation at the boundary, we then obtain a similar power balance equation relating  $T_e$  and  $F$  in the GaAs layer;

$$\left(\frac{2\hbar\omega_o}{\pi m_1^*}\right)^{1/2} eE_o \frac{\exp(Z_o - Z_e) - 1}{\exp(Z_o) - 1} Z_e^{1/2} \exp(Z_e/2) K_o(Z_e/2) \\ = e\mu_1 F^2 + \frac{5\mu_2}{2eL_1} k^2 T_L(0) \frac{dT_L(0)}{dx} \quad (2.8)$$

where  $Z_e = \frac{kT_e}{\hbar\omega_o}$ , and  $\mu_1$  is the mobility in the GaAs when only polar optical scattering is operative. This mobility is given by;

$$\mu_1 = \frac{3\sqrt{\pi}}{2E_o} \left(\frac{2\hbar\omega_o}{m_1^*}\right)^{1/2} \frac{1}{N_q} Z_e^{-3/2} \exp(-Z_e/2) \left\{ [\exp(Z_o - Z_e) + 1] K_1(Z_e/2) \right. \\ \left. + [\exp(Z_o - Z_e) - 1] K_o(Z_e/2) \right\}^{-1} \quad (2.9)$$

where  $K_1$  is the Bessel function of the first order, and  $N_q$  is given by

$$N_q = \frac{1}{\exp(\hbar\omega_o/k_B T_o) - 1} \quad (2.10)$$

The second term on the right side of Eq. (2.8) represents the power flowing out of the GaAs into the AlGaAs layers.  $T_L(0)$  and  $dT_L(0)/dx$  are evaluated at the boundary  $x = 0$ . We have used the fact that this power flow is due only to those electrons in the GaAs with energy higher than the AlGaAs band edge. Combining Eqs. (2.6) and (2.7), we can eliminate  $E_{F2}(x)$  and obtain the differential equation in terms of  $T_L(x)$  only:

$$\frac{d^2 T_L(x)}{dx^2} = \frac{2e^2}{5k^2 T_L(x)} \left[ F^2 - \frac{2\hbar\omega_0}{\mu_2 \sqrt{\pi m_2}} E_0 \frac{\exp(Z_0 - Z_L)^{-1}}{\exp(Z_L) - 1} Z_L^{1/2} \right. \\ \left. \times \exp(Z_L/2) K_0(Z_L/2) \right]. \quad (2.11)$$

This equation is now solved numerically with the boundary condition;  $T_L(0) = T_e$ , and  $dT_L(x)/dx = 0$  at  $T_L = T_0$ .

To determine the quasi-Fermi levels,  $E_{F1}$  and  $E_{F2}(x)$ , we need two additional conditions. One is obtained from the condition  $j_x = 0$ . We simplify this condition to the balance of the thermionic currents in both directions at the interface. Under collision-free transport conditions the thermionic current  $j_{1-2}$ , from the GaAs to the AlGaAs, is given after Bethe[28] by;

$$j_{1-2} = \frac{em_1^*}{2\pi^2 \hbar^3} (kT_e)^2 \exp\left[\frac{E_{F1} - \Delta E}{kT_e}\right]. \quad (2.12)$$

The current  $j_{2-1}$  flowing from the AlGaAs to the GaAs layer is;

$$j_{2-1} = \frac{em_2^*}{2\pi^2 \hbar^3} (kT_L)^2 \exp\left[\frac{E_{F2} - \Delta E}{kT_L}\right], \quad (2.13)$$

where  $T_L$  is evaluated at  $x = 0$ . Under steady-state conditions we have  $j_{1-2} = j_{2-1}$ . The other additional condition arises from conservation of the total number of electrons,  $N = N_1 + N_2$ .  $N_1$  and  $N_2$  are calculated using the electron temperature and quasi-Fermi level in each layer.

### 2.2.3 Results

From Eq. (2.8) we obtain the variation of electron temperature,  $T_e$ , with the electric field in the GaAs layer. The result is shown in Fig. 2.3 with the mobility in the AlGaAs layer as a parameter. The dashed curve is for bulk GaAs, with only polar optical scattering operative. This corresponds to treating the GaAs and the AlGaAs layers independently (in other words,  $\mu_2 = 0$ ). As is well known[29,30], at an electric field of about 3.4 kV/cm the electron temperature goes to infinity and "polar runaway" occurs. When the transport of hot electrons is taken into account, however, the electron temperature does not increase as rapidly. The rate of increase is slower for higher mobility in the AlGaAs, because of the larger power out-flow. This situation is quite analogous to the Gunn effect[30,31] where intervalley scattering supplies an additional energy loss mechanism[32].

Fig. 2.4 shows the position dependence of both the electron temperature,  $T_L(x)$ , and the Fermi level,  $E_{F2}(x)$ , for several values of electric field. The dashed line indicates the GaAs potential well of 250 meV depth. The interface is set at  $x = 0$ . It can be seen that both  $T_L(x)$  and  $E_{F2}(x)$  approach their equilibrium values within a distance on the order of  $0.1 \mu$ . The small spikes in the quasi-Fermi levels which occur at the boundary arise from the imposed condition of thermionic current balance and from the small difference in effective masses. These spikes are of no physical significance. The rapid decrease of the quasi-Fermi level in the GaAs with higher fields indicates the depletion of electrons in this layer, and hence the transfer of electrons into the AlGaAs. The variation of the fraction of electrons in the GaAs layer with increased field is illustrated

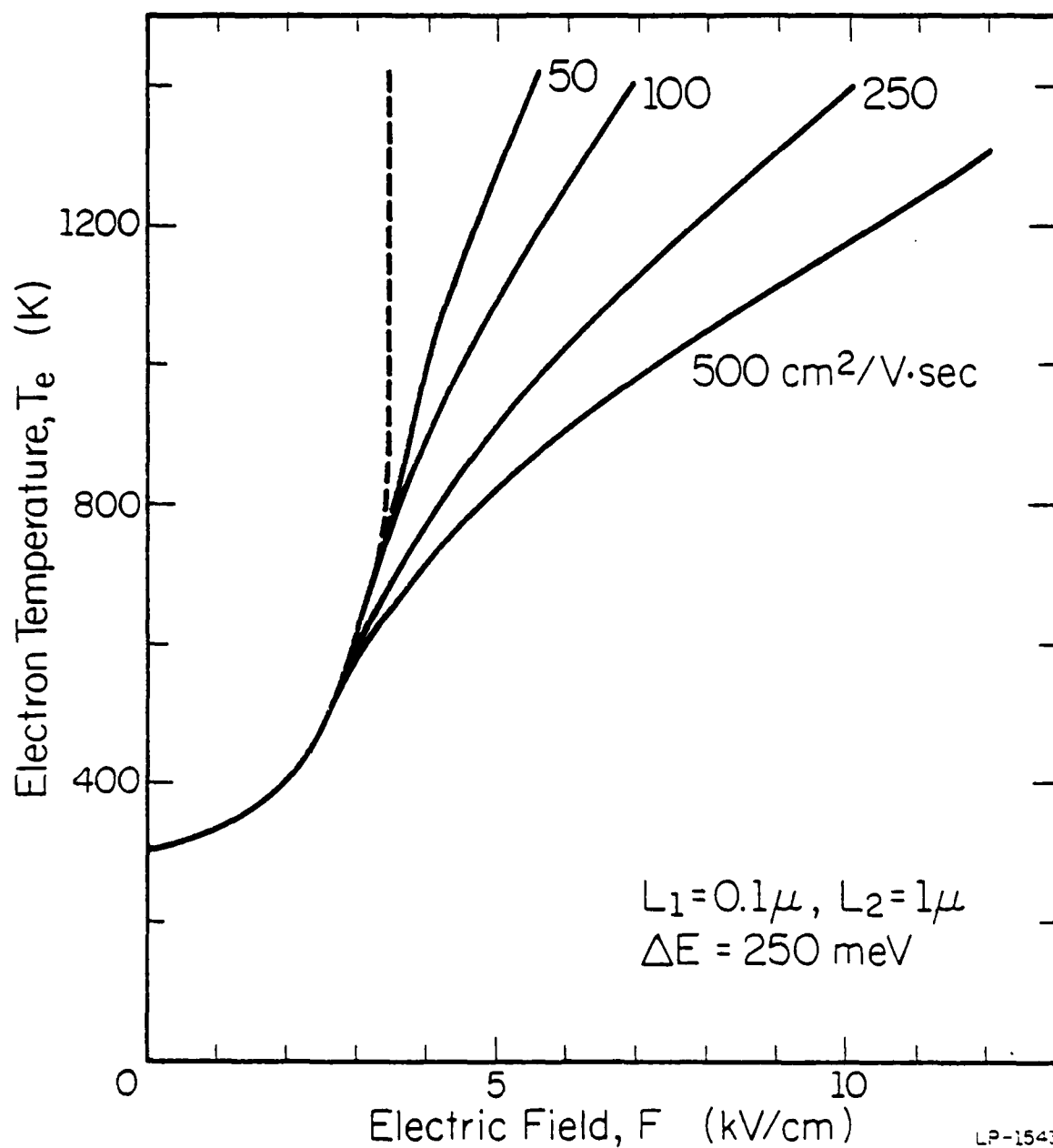
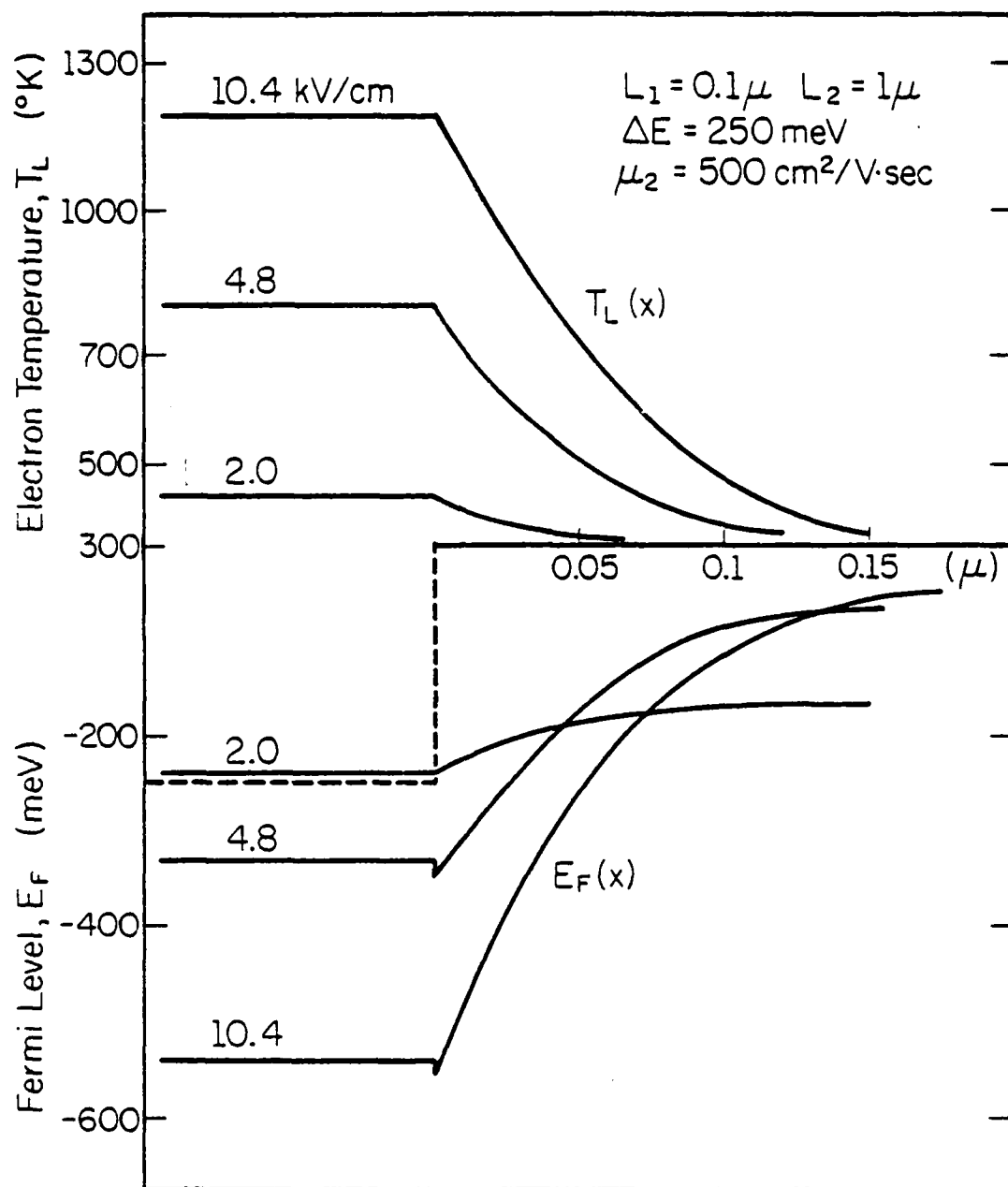


Fig. 2.3. Variation of electron temperature in the GaAs layer with applied field for various mobilities in the  $\text{Al}_x\text{Ga}_{1-x}\text{As}$  layer.



P-1540

Fig. 2.4. Electron temperature and quasi-Fermi level as functions of position. The GaAs potential well is shown in the dashed line. The interface between the GaAs and the  $\text{Al}_{0.1}\text{Ga}_{0.9}\text{As}$  is set at  $x = 0$ .

in Fig. 2.5. The transfer is larger for smaller mobility values, a consequence of the greater carrier heating for smaller mobility as seen in Fig. 2.3. Here again the analogy with the Gunn effect should be noted[32].

The current-voltage characteristics are straight forward to calculate from this model. The results of the calculations are shown in Fig. 2.6. The magnitude of the NDR changes dramatically with the mobility in the AlGaAs layer. For purposes of comparison we include in Fig. 2.6 (insert) the velocity-field characteristics calculated by Fawcett et al.[33] in 1970 for the Gunn effect. The parameter for their curves was the intervalley deformation potential. Since no reliable data on the strength of intervalley scattering was available in 1970, the intervalley deformation potential was used as a parameter.

#### 2.2.4 Comparisons with the Gunn effect

The two sets of curves in Fig. 2.6 show surprisingly similar features. Actually our discussion of real space transfer almost parallels that of the Gunn effect, but with two crucial differences. First, in our mechanism electrons leave the high mobility GaAs layer by thermionic emission and are transferred in real space to the low mobility AlGaAs layer. In the Gunn effect, on the other hand, electrons transfer from one valley of high mobility to another of low mobility in momentum or k-space. Second and most important is the fact that our device characteristics can be controlled to a greater degree than with a device utilizing the Gunn effect. As already seen in Fig. 2.6 (insert), the curves for the Gunn effect have as a parameter the intervalley deformation potential, which is a material property and cannot be changed. The intervalley deformation potential between the  $\Gamma$  and L valleys is now known to be around  $1 \times 10^3$

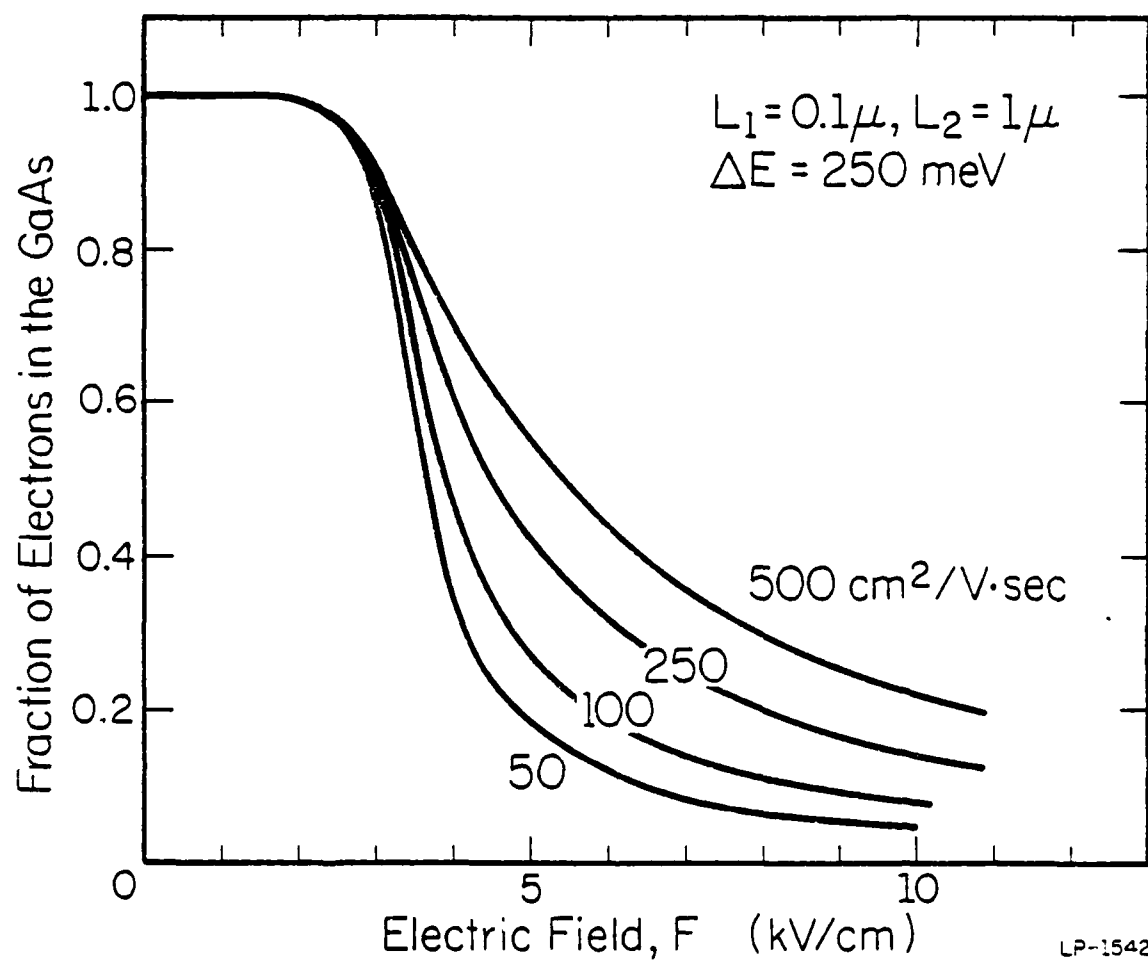


Fig. 2.5. Fraction of electrons in the GaAs layer as a function of electric field for various mobilities in the  $\text{Al}_x\text{Ga}_{1-x}\text{As}$  layer.

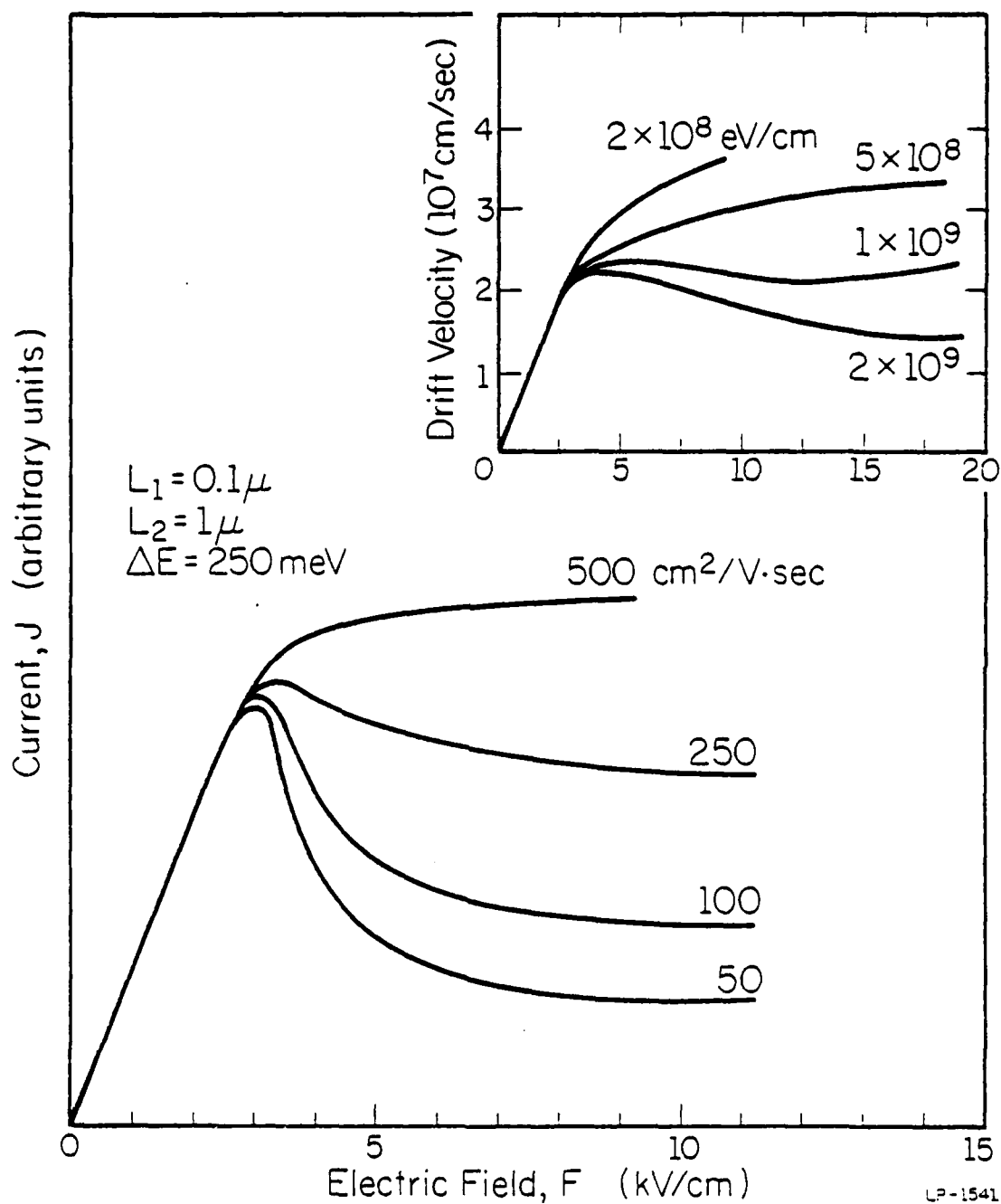


Fig. 2.6. Current-voltage characteristics for a real-space transfer device with various values of electron mobility in the  $\text{Al}_x\text{Ga}_{1-x}\text{As}$  layer. The inset shows the velocity-field characteristics of the Gunn effect in GaAs for various intervalley deformation potentials [33].



eV/cm in GaAs[34]. On the other hand, the parameter in Fig. 2.6 for the real space transfer process is the mobility of the AlGaAs layer, which can be controlled by adjusting the doping of the layer. The characteristics can also be changed by varying other device parameters, such as the layer dimensions and the potential barrier height.

#### 2.2.5 Influence of material parameters on the real space transfer

The potential barrier height can be controlled by changing the Al mole fraction of the AlGaAs. The effect of this parameter on the current-voltage characteristics is shown in Fig. 2.7. For this particular set of parameters the threshold field for the onset of NDR can be varied between 2 and 3 kV/cm and the peak-to-valley ratio between 1.3 and 2.0. Fig. 2.8 shows the fraction of electrons in the GaAs for the same parameter. The transfer of electrons is more abrupt for the deeper potential well, which results in larger peak-to-valley ratio as shown in Fig. 2.7. This occurs because the deeper the potential well is, the more the electrons can be heated before they begin to transfer, and hence the larger gradient of carrier temperature results at the interface at the beginning of transfer. In this electron temperature model we do not take into account the effects of the conduction band L minima, which are known to be located approximately 330 meV above the  $\Gamma$  minimum of GaAs[34,36]. We have deliberately chosen values of  $\Delta E$  such that the L minima are above the band edge of the AlGaAs. The effects of the L minima will be discussed more extensively in Section 2.3.

The layer dimensions can be varied by changing the crystal growth parameters. Fig. 2.9 shows the electron temperature in the GaAs as a function of electric field for several thicknesses of the GaAs layers. The

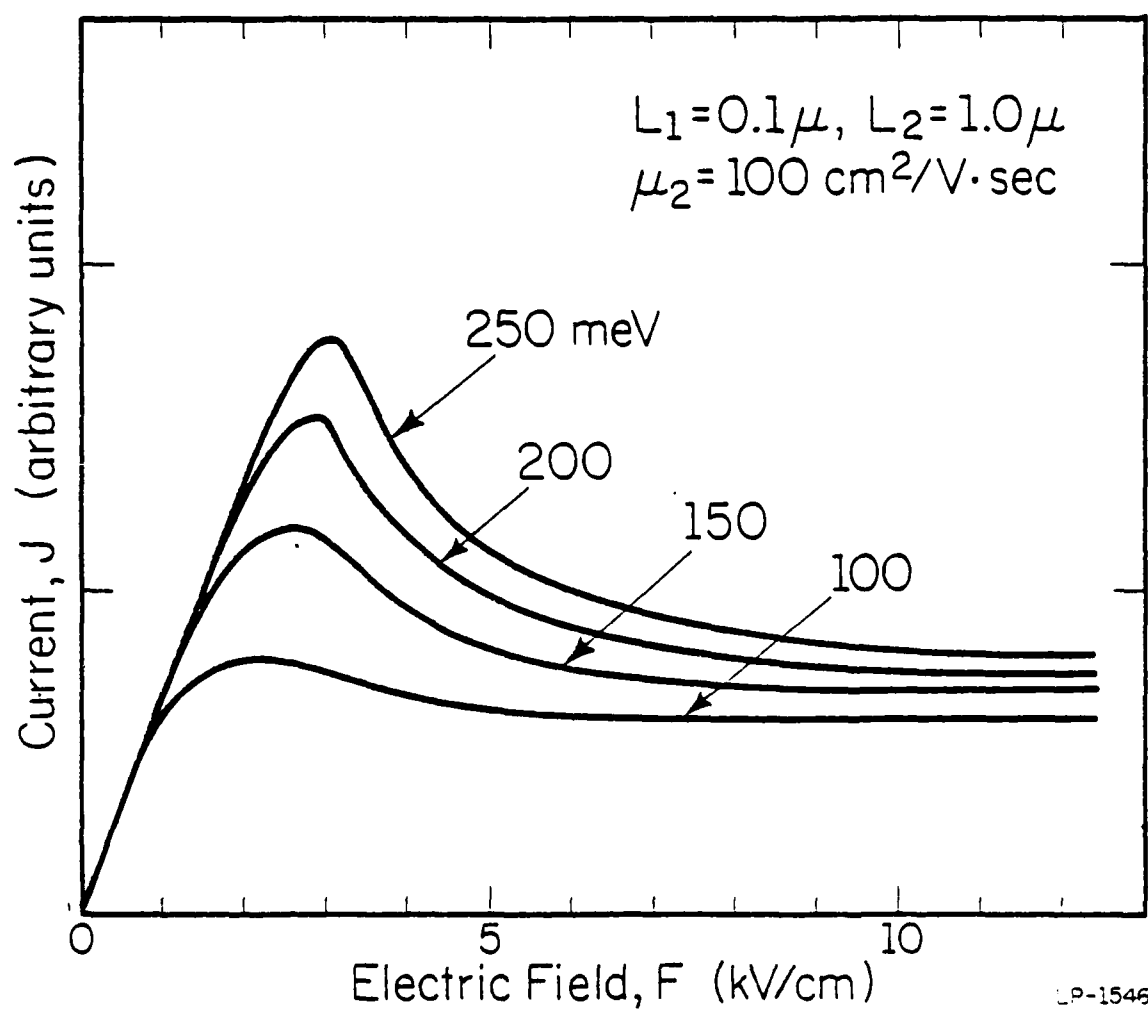


Fig. 2.7. Current-voltage characteristics for various potential barrier heights. Note that the GaAs L minima are above the conduction band edge of the  $\text{Al}_x\text{Ga}_{1-x}\text{As}$  in the cases shown.

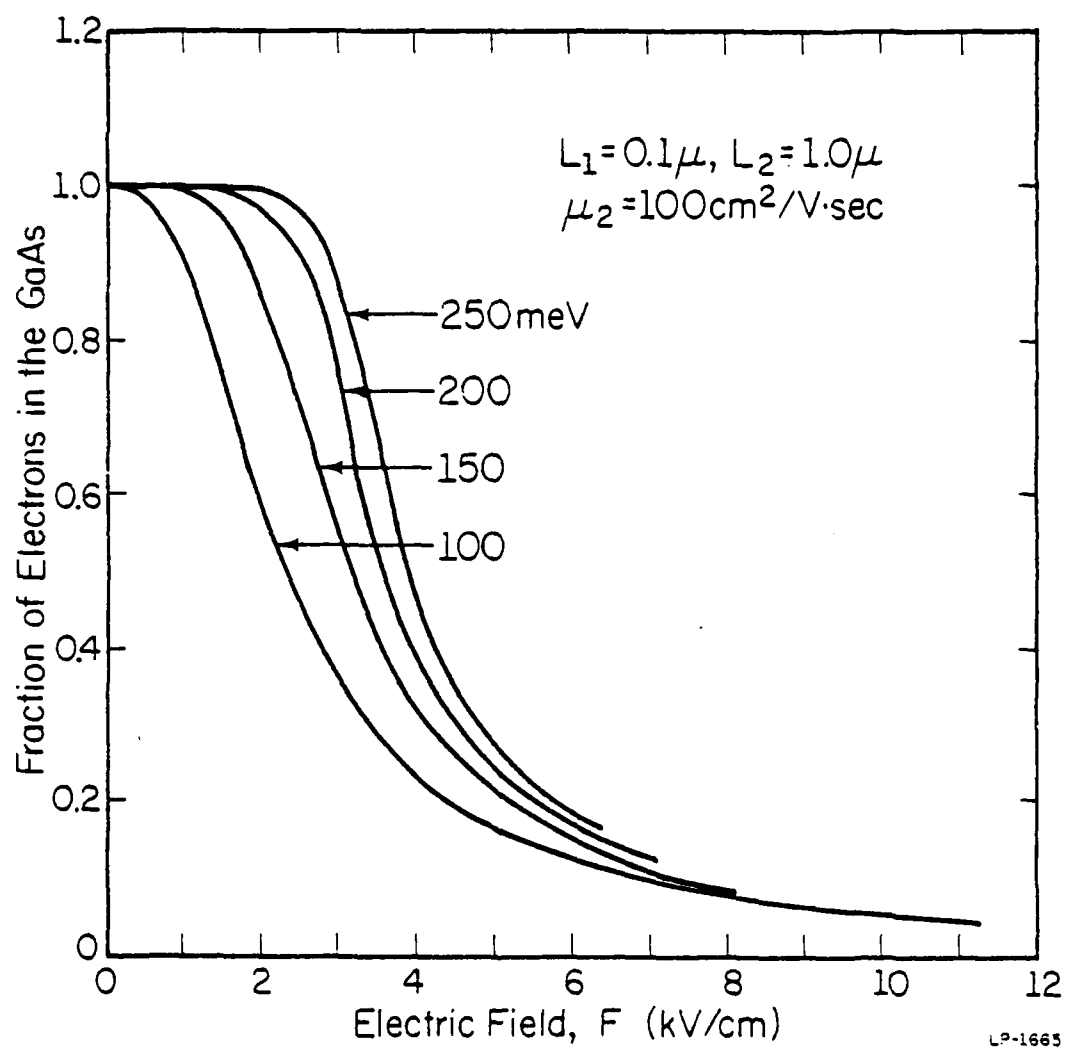


Fig. 2.8. Fraction of electrons in the GaAs layer as a function of electric field for various potential barrier heights.

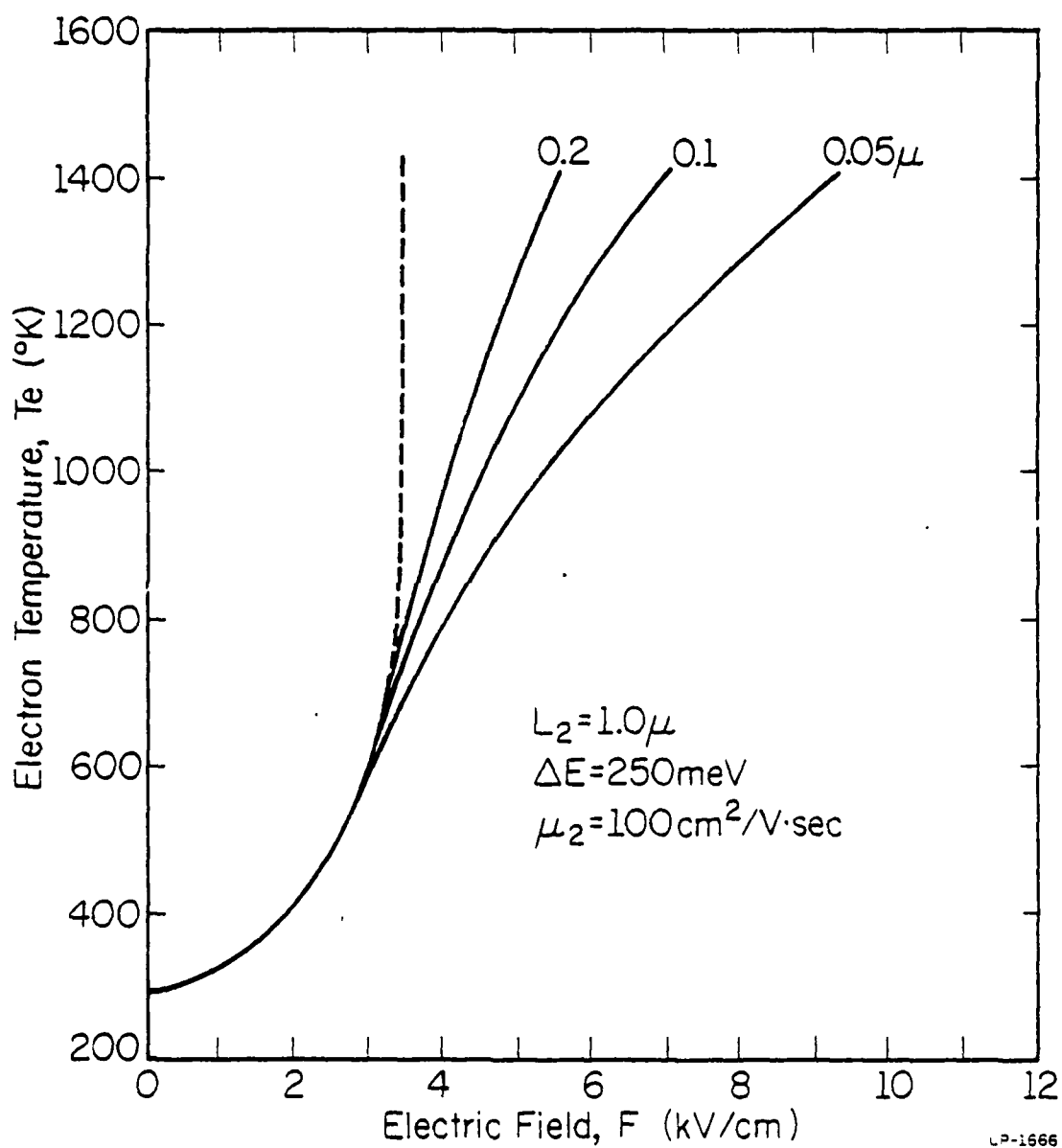


Fig. 2.9. Variation of electron temperature in the GaAs layer with applied field for various thicknesses of the GaAs layer.

degree of carrier heating is smaller for thinner GaAs layers because of the larger cooling effect of the surrounding AlGaAs layers. Fig. 2.10 shows the effect of changing the GaAs thickness on the current-voltage characteristics.

The lattice temperature dependence of the current-voltage characteristics is another interesting subject[35]. Fig. 2.11 shows the result of the calculation in the temperature range 77 ~ 400 K. In this calculation the electron mobility in the AlGaAs layer is assumed to be constant at  $100 \text{ cm}^2/\text{Vsec}$ . In heavily doped materials, and in particular, compensated materials, the mobility is known to vary very little with temperature[37]. Since the mobility in the GaAs layer increases considerably as the temperature decreases, the larger peak-to-valley ratio results at lower temperature. According to our calculation, the peak-to-valley ratio improves from 1.56 at 400 K to 7.75 at 77 K. This suggests that the experimental manifestation of the real space transfer mechanism can be more easily realized at lower temperature.

Although the electron temperature model is based on several simplifying assumption, some of which are difficult to justify, it provides a qualitative method with which to analyze the real space transfer mechanism. The model is exact in the high carrier density limit. The Monte Carlo method is easily tractable in the other extreme, i.e. the low density limit. As will be seen the results obtained from both method show surprisingly similar features (such as dependence on barrier height, AlGaAs mobility, etc.). This suggests that these features are in fact general and do not depend on the assumptions of the model.

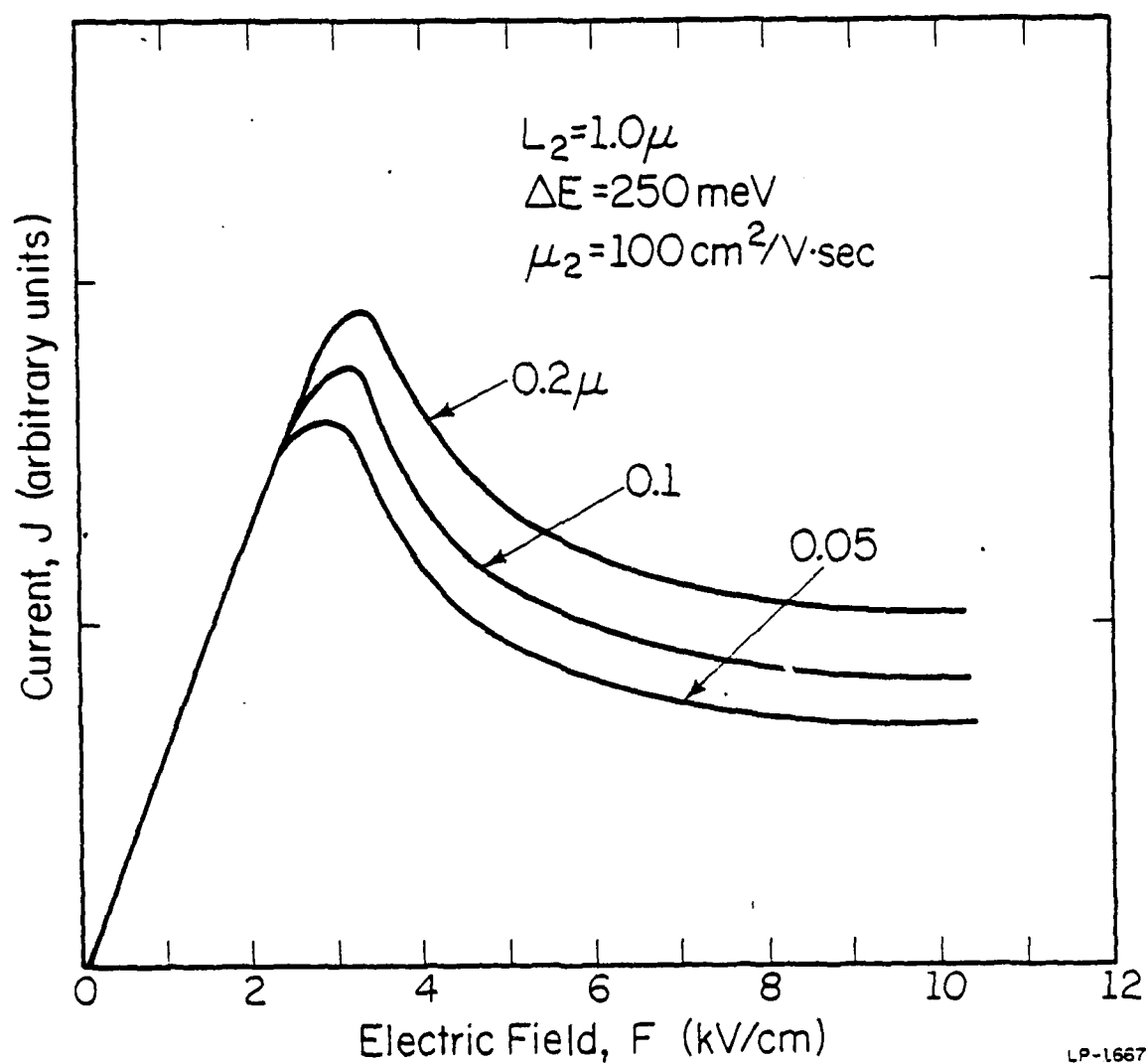


Fig. 2.10. Current-voltage characteristics for various thicknesses of the GaAs layer.

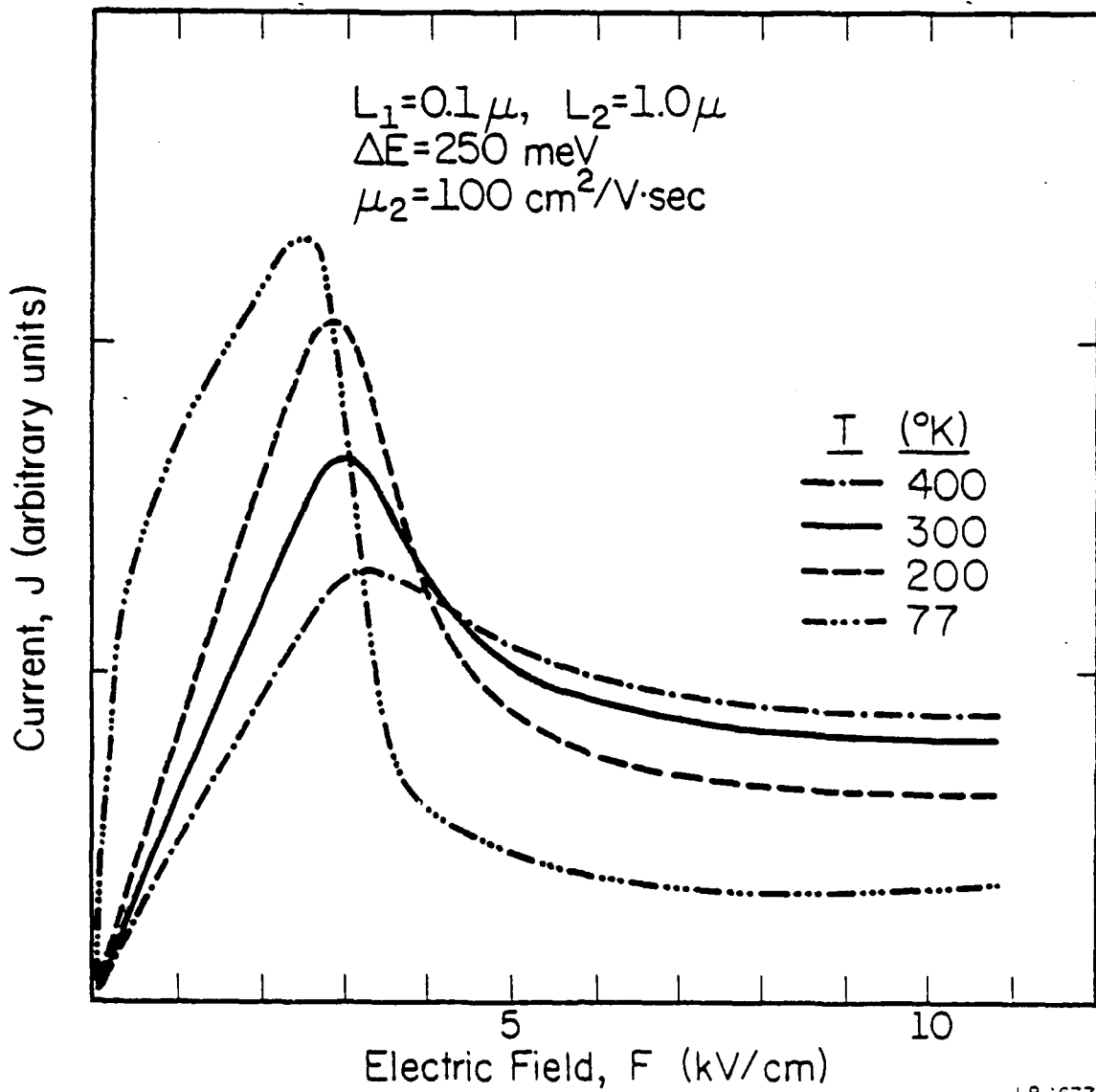


Fig. 2.11. Current-voltage characteristics for various lattice temperature.

## 2.3 Monte Carlo Simulation of Real Space Electron Transfer

### 2.3.1 Introduction

The Monte Carlo method[38] used in transport theory is based on a computer simulation of the carrier motion of an individual electron in an electric field. Physical quantities of interest (such as drift velocity) are obtained as proper statistical averages among sample members of an ensemble. The Monte Carlo procedure has been shown to yield a distribution function which is a solution of the Boltzmann equation[33] and thus provides a powerful method to solve the Boltzmann equation under quite general conditions. It has been applied with great success to the study of high field transport, and in particular, to the Gunn effect[33].

The Monte Carlo method follows a carrier experiencing successive drift and scattering event. The scattering event and the duration of each drift are determined by random numbers. The simulation is repeated a sufficient number of times to minimize statistical fluctuations.

The effectiveness of the Monte Carlo method lies in its simple principle and its flexibility. The inclusion of various complex scattering mechanisms, time dependence, and physical boundaries in position space can be done with minor elaboration of the algorithm. It is this flexibility that makes the Monte Carlo method especially useful for the simulation of real space transfer.



### 2.3.2 Simulation procedure

Fig. 2.12 shows the flow chart for the Monte Carlo simulation of real space transfer in GaAs-AlGaAs heterostructures. The quantities  $\vec{r}$ ,  $\vec{k}$ , and  $E$  denote the position vector, the k-vector, and the energy of the electron respectively. The appearance of  $r_n$  in the flow chart means that a random number uniformly distributed between 0 and 1 is necessary at that stage.

The lower right portion of the flow chart is specific to the simulation of real space transfer mechanism. The spatial configuration is shown in Fig. 2.13. The model assumes an abrupt potential barrier of height  $\Delta E$  in the GaAs. Band bending effects are neglected as in the electron temperature model. The basic cell from  $x = 0$  to  $x = d_1 + d_2$  is cyclically repeated in the simulation. The calculation of the transmission coefficient is described in detail in Section 2.5.2.

All the formula and material constants necessary for the calculation of the scattering rates are given in Appendices 1 and 2. After the scattering rate of each mechanism has been calculated, the total scattering rate is obtained by summing over all the possible scattering mechanisms at each value of electron energy. The probability table is then constructed, which is used in the determination of the scattering mechanism. This table contains the relative probability of each scattering mechanism at every value of electron energy. The total scattering rate is stored in memory in the form of the slope and the intercept which linearly interpolate the rate between two neighboring energy points. This table of the slope and the intercept is used in the look-up scheme to calculate the total scattering rate at an arbitrary electron energy[39]. The integration

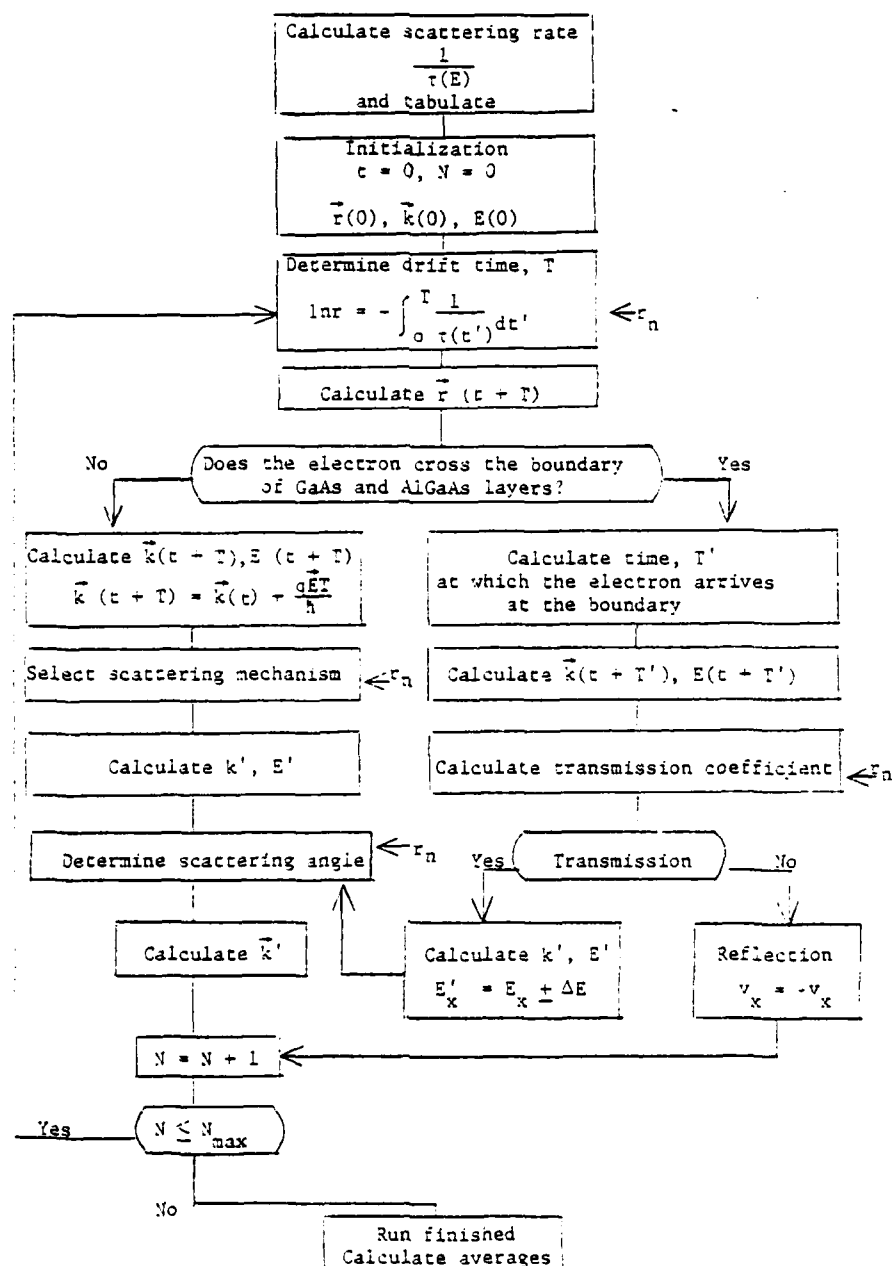


Fig. 2.12. Flow chart for the Monte Carlo simulation of real space transfer.

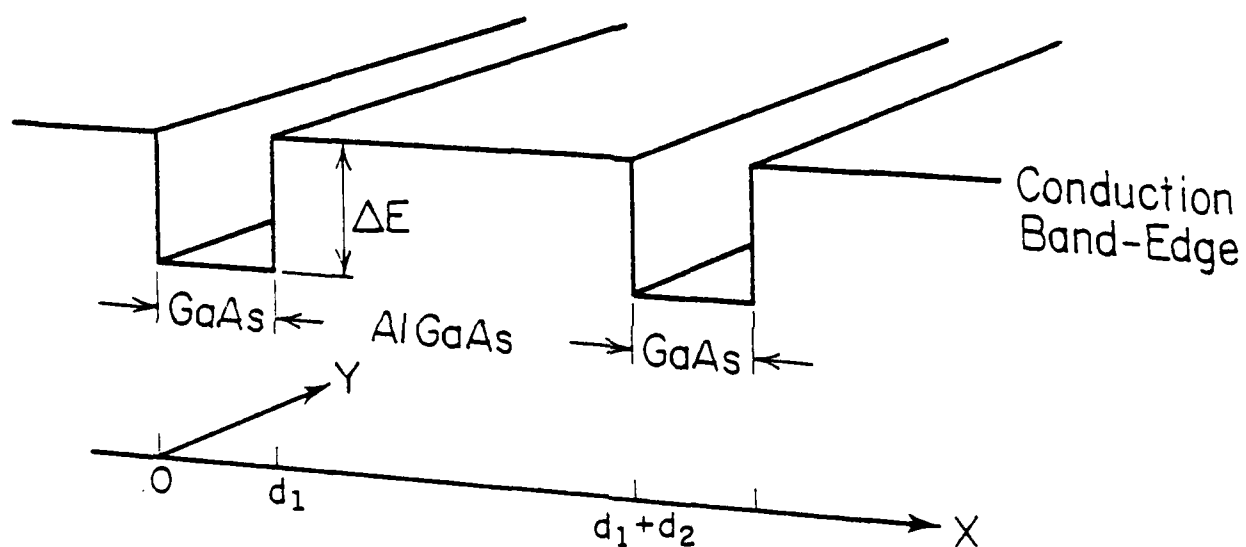


Fig. 2.13. Material configuration used to simulate real space transfer.

$$\int_0^T \frac{1}{\tau(t')} dt' \quad (2.14)$$

is performed by using the trapezoidal rule with a time step which is 1/10 th the average drift time.

The simulation begins by releasing an electron with thermal energy from the center of the GaAs well and in a randomly selected direction. The electron then undergoes scattering interactions. The scattering mechanism considered in the calculations[64] include acoustic phonon scattering, optical phonon scattering, piezoelectric scattering, equivalent and non-equivalent intervalley scattering, ionized impurity scattering, and random potential alloy scattering[73] in the AlGaAs. In some of the simulations only polar optical scattering and intervalley scattering in the GaAs and ionized impurity scattering and polar optical scattering in the AlGaAs are used to minimize the computer time. This does not affect the essential features of the results, since these scattering mechanisms are the most dominant ones. Some comparisons will be made between these two cases in the next section. In all of the simulations only the  $\Gamma(000)$  and  $L(111)$  conduction bands are considered for GaAs, and only the  $\Gamma(000)$  conduction band is considered in AlGaAs.

A typical simulation consists of approximately 100,000 to 250,000 interactions to obtain accurate velocity estimates. The average drift velocities in the individual materials and the average velocity in the heterostructures are calculated using standard velocity estimators[33]. For the ohmic range (in the GaAs at low field and in the low-mobility AlGaAs) the diffusion coefficient is calculated first from a maximum

likelihood estimate:

$$\langle (y - v_d t)^2 \rangle = 2Dt \quad (2.15)$$

where  $v_d$  is the drift velocity, and  $t$  is the duration of sampling. Then the Einstein relation is used to calculate the mobility. This method has been found to reduce the uncertainty in the calculated drift velocity at low electric field[40,41].

### 2.3.3 Results

Fig. 2.14 shows an example of the electron trajectory in real space for low (2 kV/cm) and high (6 kV/cm) electric fields obtained by the Monte Carlo method. The narrow region between two lines represents the GaAs layer, whereas the region outside are the AlGaAs layers. At low electric field (2 kV/cm) the electron stays inside the potential well as it drifts along the well, since the average electron energy ( $\sim 0.06$  eV) is much smaller than the potential barrier height (0.2 eV). The mean free path of scattering for this electric field in undoped GaAs is approximately 600 Å. Therefore the electron is reflected by the interface more often than it is scattered by a phonon. In our simulation we have assumed a specular reflection at the wall with no loss of velocity in the field direction. In reality the interface scattering may play an important role in determining the mobility in the GaAs potential well. When the electric field is high (6 kV/cm) the electron gains enough kinetic energy ( $\sim 0.17$  eV) so that it can be scattered out to the AlGaAs layer as shown on the right side of Fig. 2.14. Since the electron mobility in the AlGaAs is much lower, the electron moves much slower in this layer, and the mean free path is much shorter. There is a possibility, of course, that the electron will move

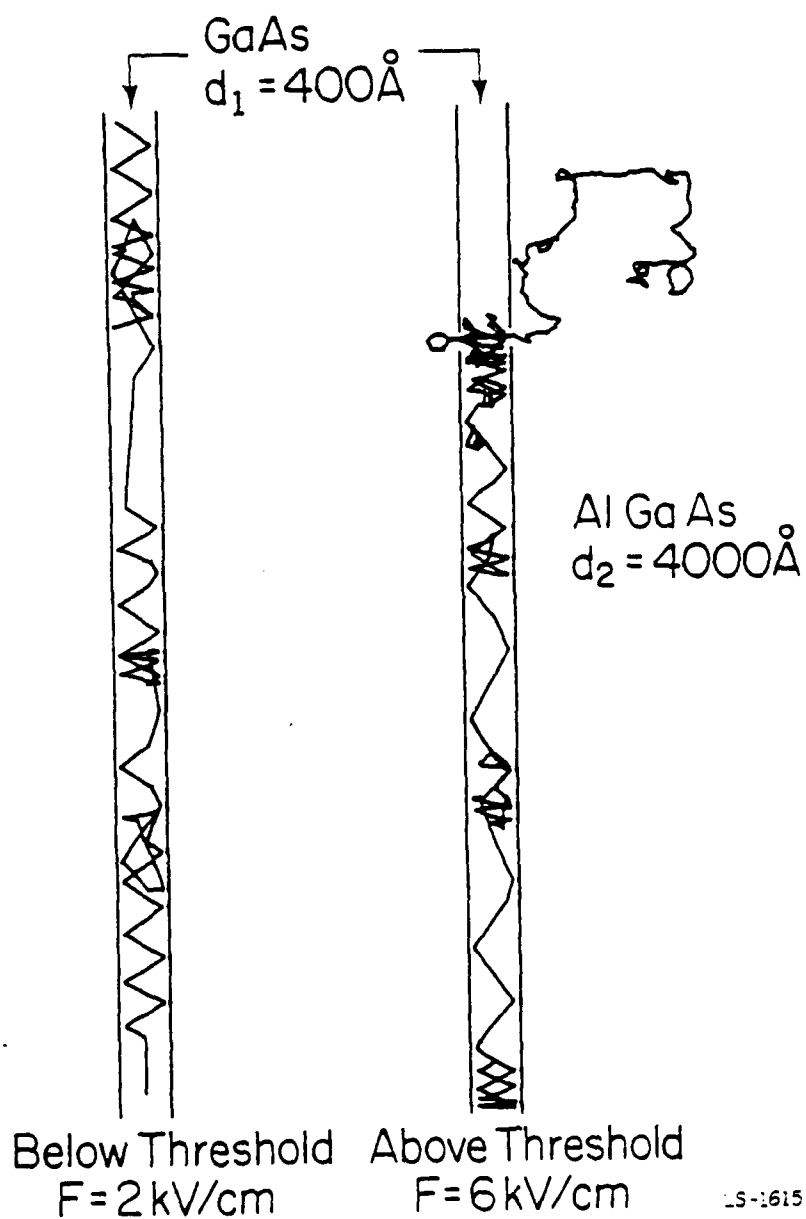


Fig. 2.14. Trajectory of an electron in real space for electric fields below and above the threshold for the real space transfer mechanism.

back into the GaAs potential well after it moves in the AlGaAs layer for a while. This is also illustrated in the figure. When observed over a sufficiently long time this individual electron's motion should be representative of all the electrons in the GaAs-AlGaAs structure. This provides a one particle picture of real space transfer.

The velocity-field characteristic of a real space transfer (RST) device obtained by the Monte Carlo method is shown in Fig. 2.15. This simulation has been done by Glisson et al.[64] including all the scattering mechanisms. For comparison the bulk characteristics of the GaAs and the AlGaAs are shown. The GaAs has no ionized impurities, and shows the usual Gunn effect at 4 kV/cm. The low-field mobility is  $3000 \text{ cm}^2/\text{Vsec}$ . The AlGaAs is strongly compensated with an impurity density of  $1 \times 10^{19} \text{ cm}^{-3}$  and a free electron density of  $1 \times 10^{17} \text{ cm}^{-3}$ . This gives an electron mobility of approximately  $500 \text{ cm}^2/\text{Vsec}$  in this material. The transport in the AlGaAs remains essentially ohmic for the range of electric field shown in the figure. The impurity density should be considered as a parameter for varying the mobility in the AlGaAs layer. In reality it may not be necessary to dope the layer with this high impurity density if there is another alternative way to grow a low-mobility material. The Al content in the AlGaAs is chosen to give a potential barrier of 0.2 eV ( $x = 0.18$ ) in the RST device. The real space transfer structure shows NDR at 2.4 kV/cm with a peak velocity of  $1.6 \times 10^7 \text{ cm/sec}$ .

For comparison we show in Fig. 2.16 the calculated velocity-field characteristics with only polar optical and intervalley scatterings in the GaAs and polar optical and ionized impurity scatterings in the AlGaAs. In this case we have fewer mechanisms for energy and momentum loss. As a

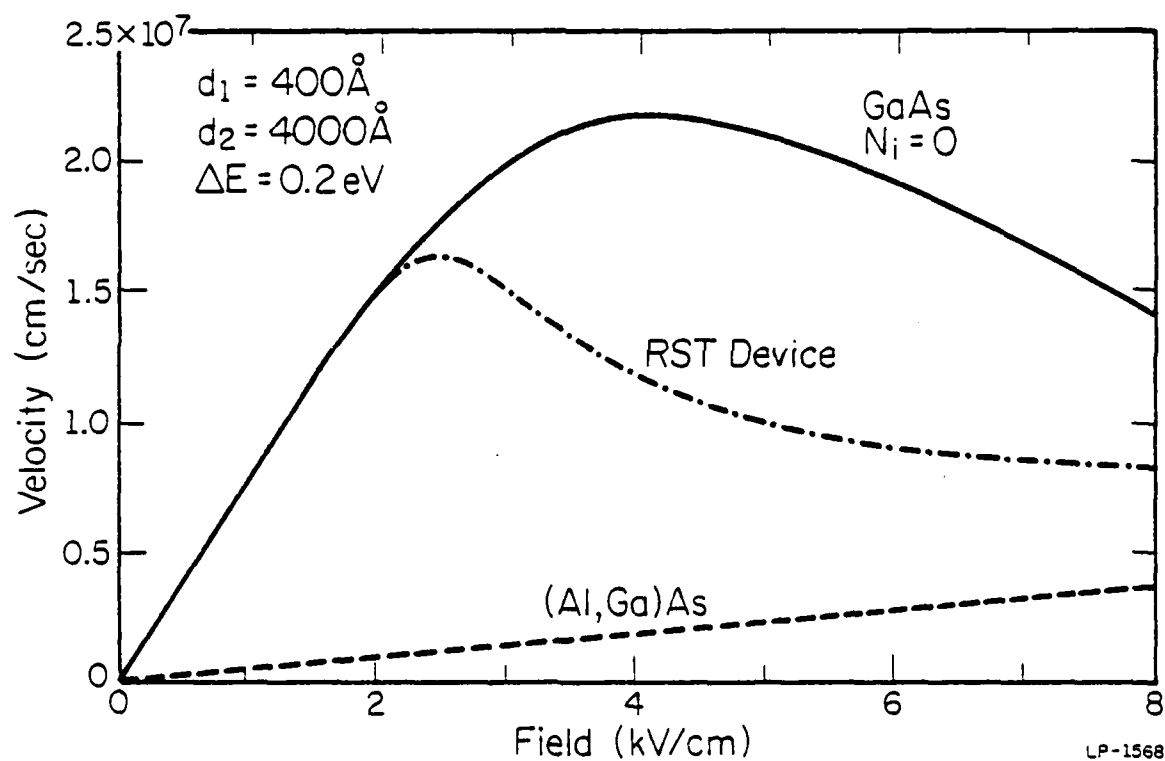
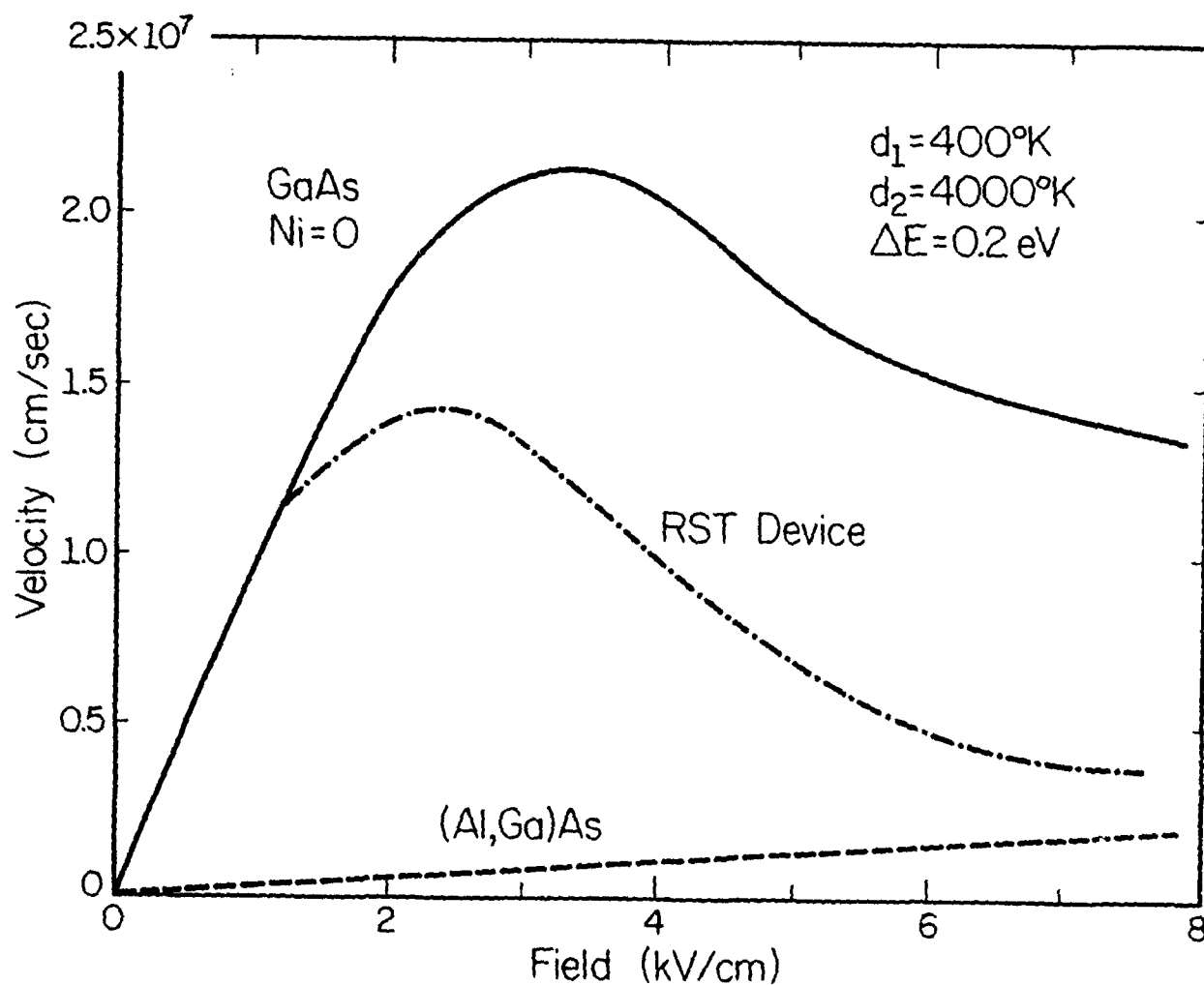


Fig. 2.15. Velocity-field characteristic for real space transfer device compared with GaAs and AlGaAs including all the scattering mechanisms [64]. Here  $N_I = 1 \times 10^{19} \text{ cm}^{-3}$ ,  $n = 1 \times 10^{17} \text{ cm}^{-3}$ , and  $\mu_2 = 500 \text{ cm}^2/\text{Vsec}$  in the AlGaAs.





LP-1727

Fig. 2.16. Velocity-field characteristic for real space transfer device compared with GaAs and AlGaAs including only dominant scattering mechanisms. Here  $N_I = 4 \times 10^{18} \text{ cm}^{-3}$ ,  $n = 1 \times 10^{17} \text{ cm}^{-3}$ , and  $\mu_2 = 270 \text{ cm}^2/\text{Vsec}$  in the AlGaAs.

result, the Gunn effect occurs at a slightly lower electric field. The low field mobility for GaAs and the RST device is slightly higher for the same reason. The usual Brooks-Herring formula for ionized impurity scattering[27] has been used in this calculation, whereas Glisson et al. have assumed a cut-off distance for the screened Coulomb interaction. The Brooks-Herring formula gives a mobility of only  $270 \text{ cm}^2/\text{Vsec}$  for a lower impurity density of  $4 \times 10^{18} \text{ cm}^{-3}$  (and the same free electron density of  $1 \times 10^{17} \text{ cm}^{-3}$ ). The reason for the discrepancy is that for very high dopings the average distance between impurities becomes smaller than the Debye screening distance. As a result, the Brooks-Herring formula (which only considers an isolated impurity) overestimates the interaction. For the analysis of real space transfer, however, this discrepancy is irrelevant because the characteristics are determined mainly by the mobility. As long as the mobilities are similar, the two results are expected to be similar.

Fig. 2.17 shows the relative numbers of electrons in the GaAs and the AlGaAs layers using the same parameter values as shown in Fig. 2.15. It can be seen that even for fields well above threshold a substantial fraction of electrons remains in the GaAs. These residual electrons in the GaAs layer might hinder the application of this mechanism to switching devices since they constitute a considerably large current in the "off" state. The ratio of electrons in the two materials can be improved, however, by reducing further the mobility in the AlGaAs. In Fig. 2.18 the mobility is reduced to about  $50 \text{ cm}^2/\text{Vsec}$  by increasing the impurity density to  $1 \times 10^{20} \text{ cm}^{-3}$ . In this case less than  $10^{-3}$  of the electrons remain in the GaAs at  $3 \text{ kV/cm}$ . The peak velocity of  $1.6 \times 10^7 \text{ cm/sec}$ , threshold field of  $2.3 \text{ kV/cm}$ , peak-to-valley ratio of 4, and a negative mobility magnitude above threshold of greater than  $1 \times 10^4 \text{ cm}^2/\text{Vsec}$  are very

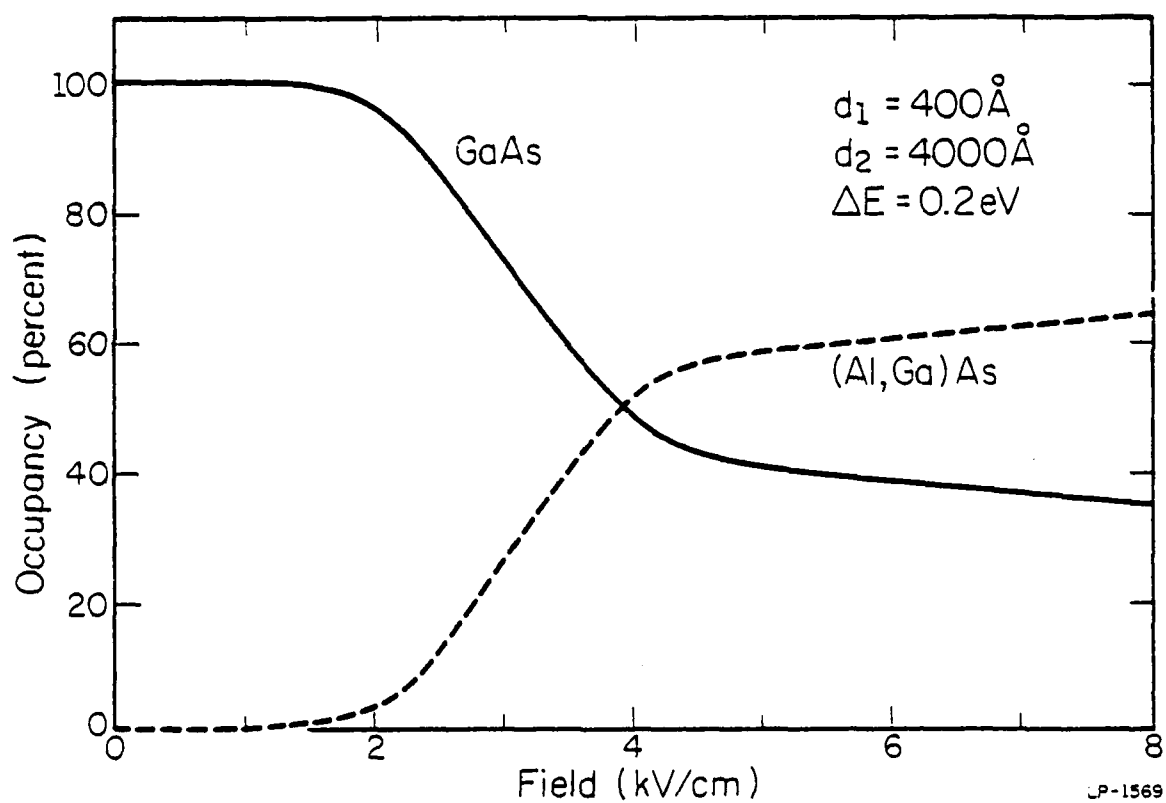


Fig. 2.17. Relative occupancy of electrons in GaAs and AlGaAs versus field for the same parameters as in Fig. 2.15 [64].

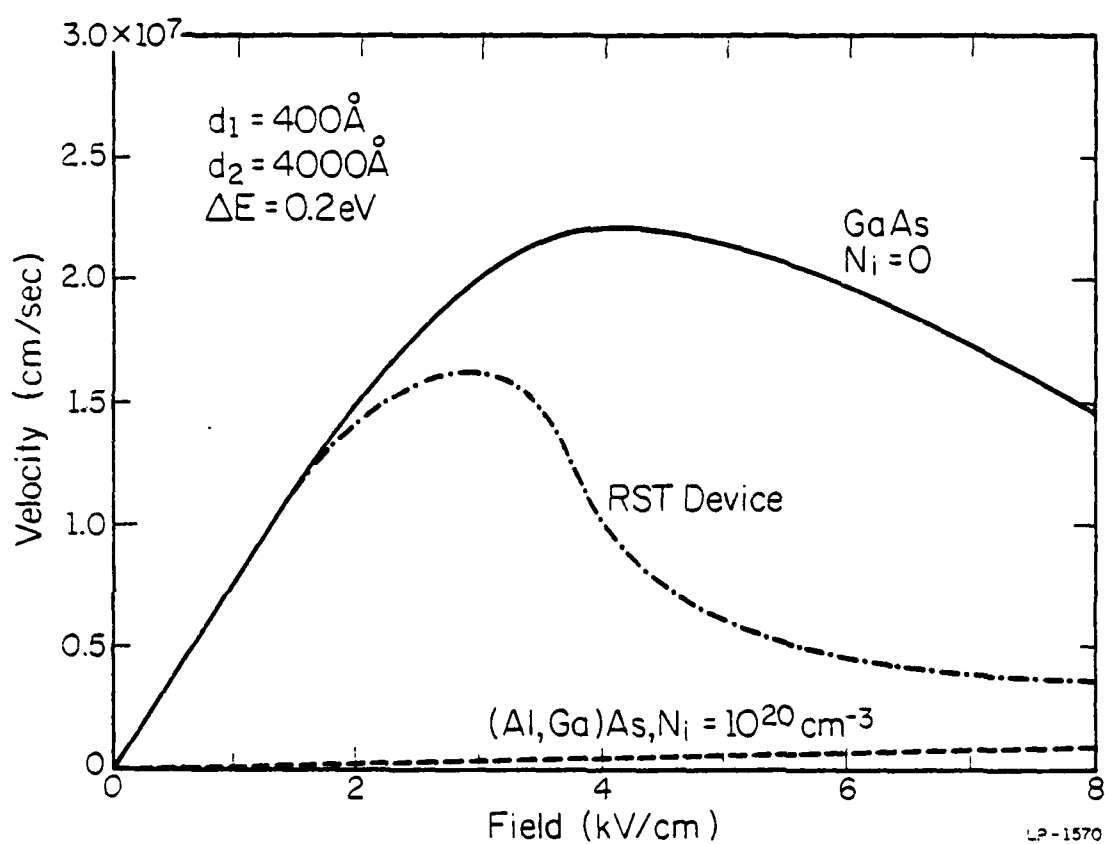


Fig. 2.18. Velocity-field characteristic for real space transfer device. All the parameters are the same as in Fig. 2.15, except  $\mu_2 = 50 \text{ cm}^2/\text{Vsec}$  in the AlGaAs [64].

attractive parameters for Gunn-type device considerations. On the other hand, if the AlGaAs mobility is increased, a substantial number of electrons remain in the GaAs. Now the transport property of the structure is determined by both the GaAs and the AlGaAs. This is illustrated in Fig. 2.19 for an AlGaAs mobility of  $4000 \text{ cm}^2/\text{Vsec}$ . The curve shows the saturating characteristic and a peak velocity of  $2 \times 10^7 \text{ cm/sec}$  with very small negative resistance. This illustrates the possibility of artificially creating the velocity-field characteristics using a layered heterostructure.

As in the electron temperature model it is possible to study the effects of changing various device parameters with the Monte Carlo simulation. For example, the effect of varying the potential barrier height (Al mole fraction) is shown in Fig. 2.20. Although the peak velocity increases with the barrier height, the magnitude of the negative differential resistance shows a maximum for a barrier height of about 0.2 eV. This result should be compared with the one obtained from the electron temperature model (Fig. 2.7). Fig. 2.21 shows the effect of changing the layer dimensions. By increasing the ratio of the AlGaAs and the GaAs layer width the peak velocity decreases whereas the peak-to-valley ratio increased. The larger peak-to-valley ratio results from the larger fraction of electrons in the AlGaAs as shown in Fig. 2.22. Again, Fig. 2.21 should be compared with Fig. 2.10 from the electron temperature model.

So far we have not mentioned the effects of L valley in the GaAs. The L valley is known to be located approximately 0.33 eV above the  $\Gamma$  minimum[34,36]. If the barrier height,  $\Delta E$ , is close to this energy, it is

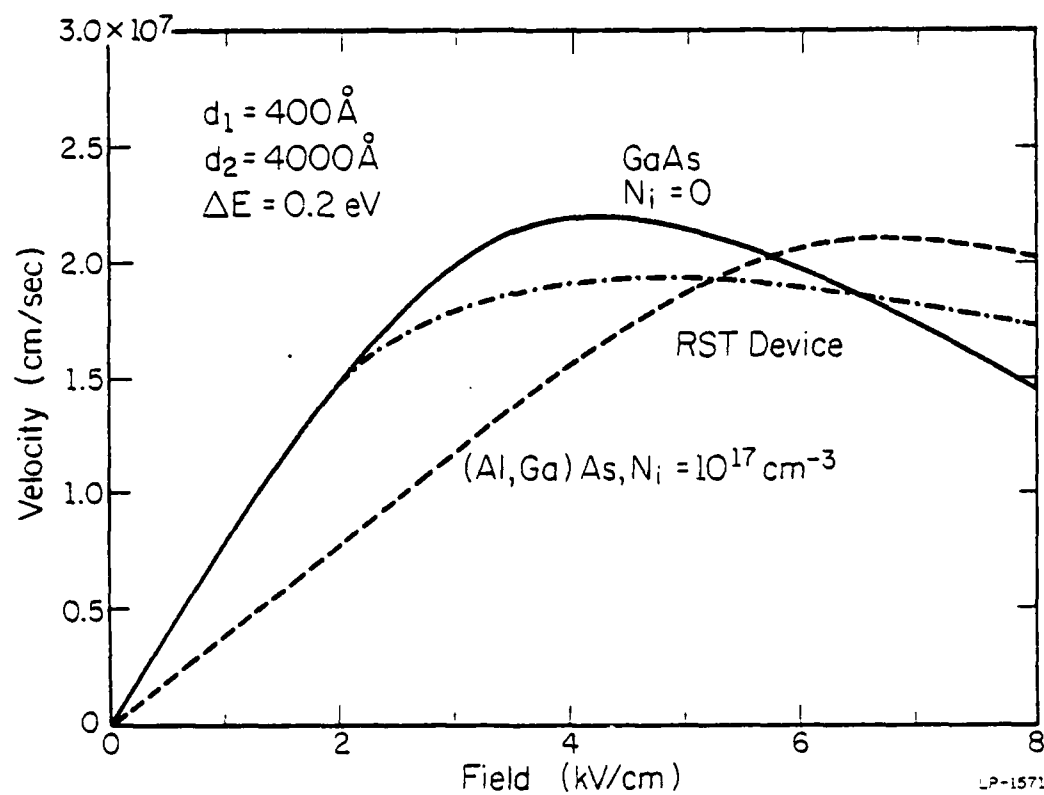


Fig. 2.19. Velocity-field characteristic for real space transfer device. All the parameters are the same as in Fig. 2.15, except  $\mu_2 = 4000 \text{ cm}^2/\text{Vsec}$  in the AlGaAs [64].

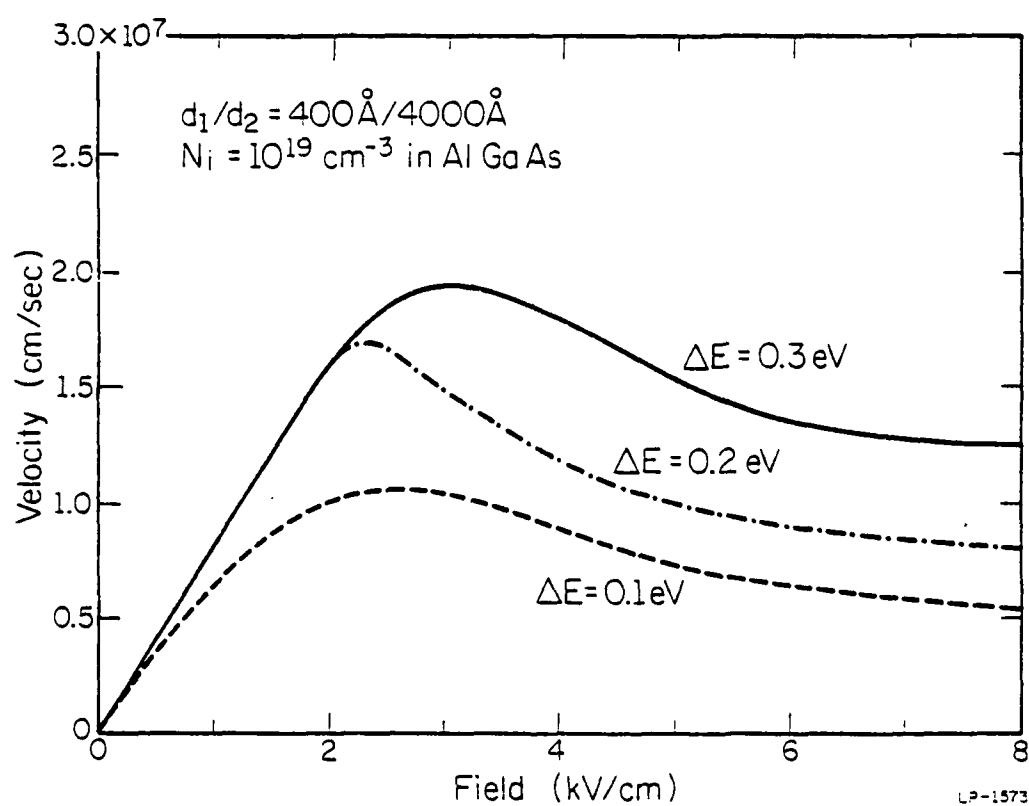


Fig. 2.20. Velocity-field characteristics for real space transfer device with potential barrier height as a parameter [64].

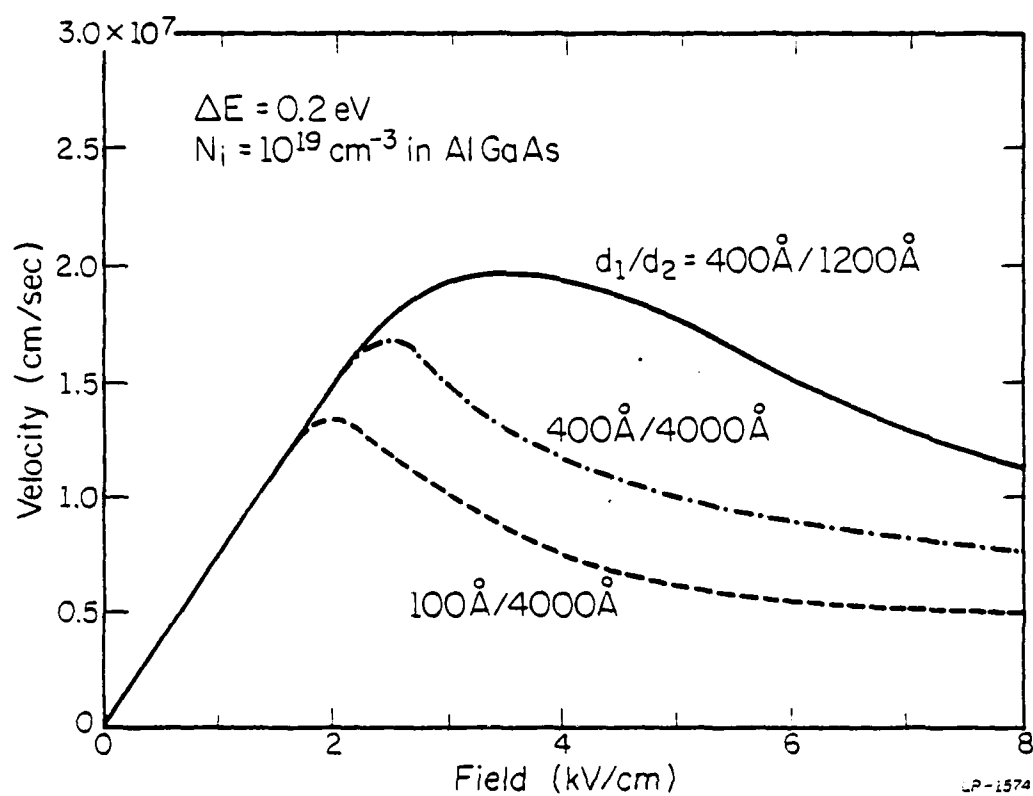


Fig. 2.21. Velocity-field characteristics for real space transfer device with AlGaAs thickness as a parameter [64].



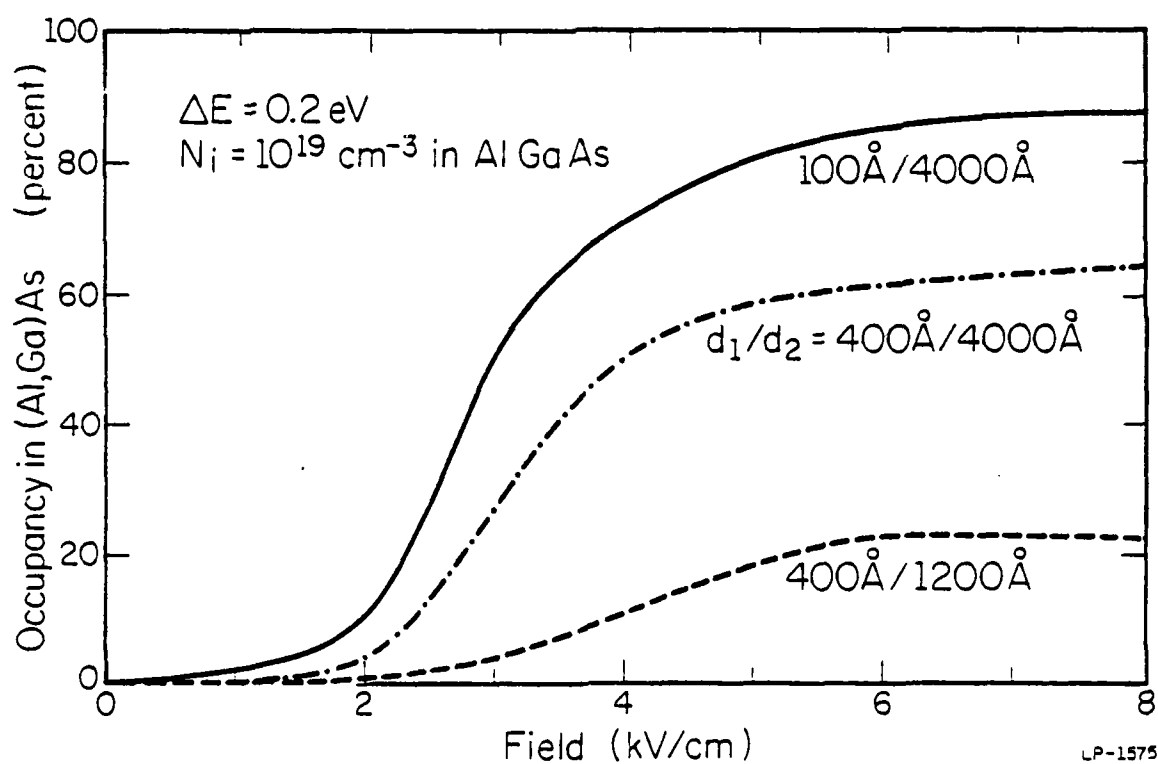


Fig. 2.22. Relative occupancy of electrons in AlGaAs, with AlGaAs thickness as a parameter.

possible for some of the hot electrons to transfer to the L valley of GaAs rather than to the AlGaAs layer. This is illustrated in Fig. 2.23 which shows the relative populations of the  $\Gamma$  and L valleys in the GaAs and AlGaAs for the parameters used in Fig. 2.16. With this set of parameters ( $\Delta E = 0.2$  eV) approximately 20 % of the electrons are transferred to the L valley at 3 kV/cm. If the band edge of the AlGaAs is aligned with the location of the L valley ( $\Delta E = 0.33$  eV), the effect is expected to be larger. The result of this calculation is shown in Fig. 2.24. Now more than 40 % of electrons transfer to the L valley. This figure also shows that the transfer to the L valley is slightly more efficient than real space transfer to the AlGaAs layer. For the real space transfer mechanism to be dominant, the barrier height should be lower than  $\sim 0.25$  eV. The effect of the L valley in the AlGaAs is expected to be very small, since the electrons in the low mobility AlGaAs will not heat up as much.

The Monte Carlo simulations also provide the distribution function by setting up an energy histogram[33]. Fig 2.25 shows the distribution function sampled at the GaAs side of the interface. At lower fields ( $\sim 1$  kV/cm) the curve is almost a straight line indicating that the distribution is approximately Maxwellian. As the field increases, however, a significant structure appears above 0.2 eV which corresponds to the conduction band edge of AlGaAs. Since the mobility in the AlGaAs layer is much lower, the AlGaAs electrons do not heat up as much as those in the GaAs layer. These cooler electrons can be transferred back to the GaAs layer causing a bump in the distribution function. It is also noted that the effective electron temperature (inverse slope of the distribution function) is smaller at higher energies due to these cooler electrons from the AlGaAs. This situation is quite analogous to that in the Gunn effect,

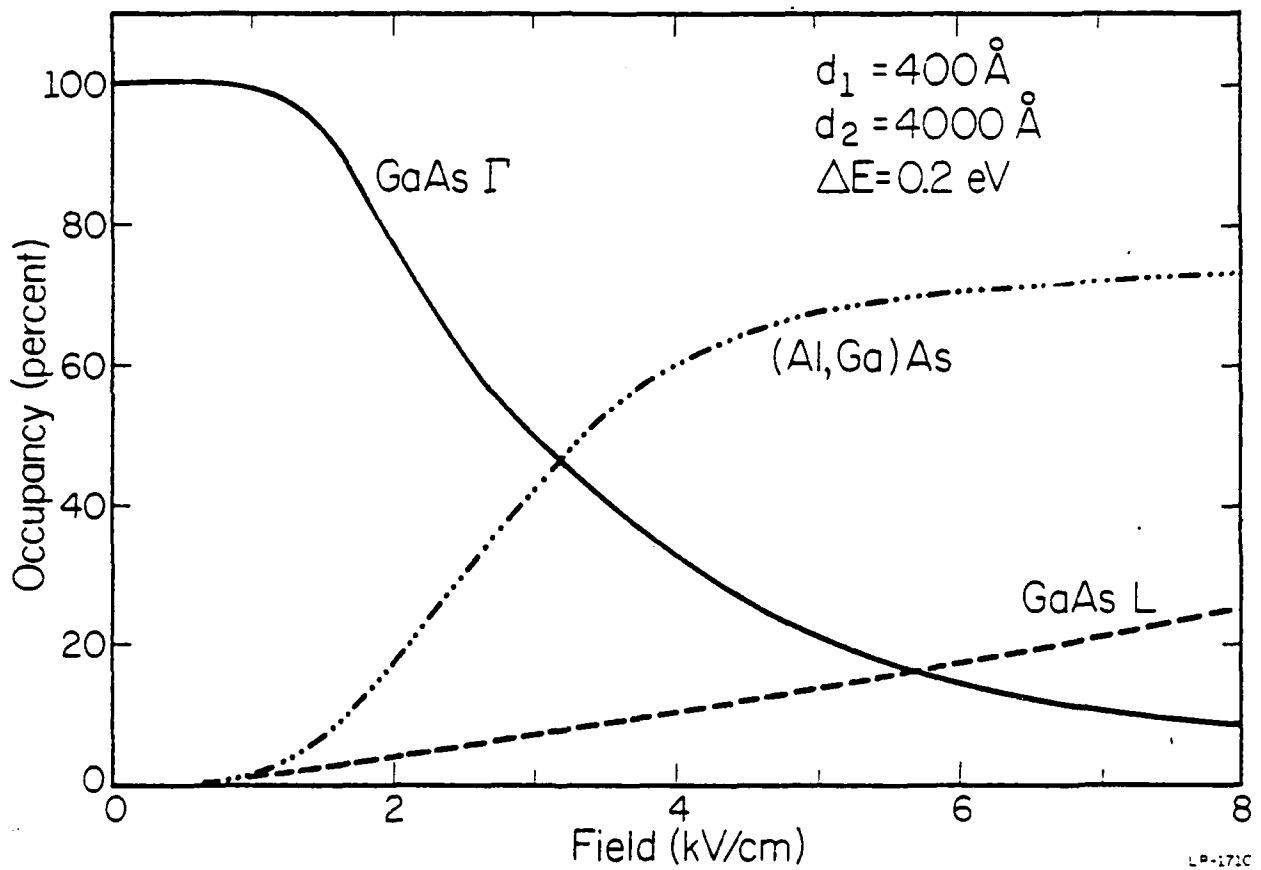
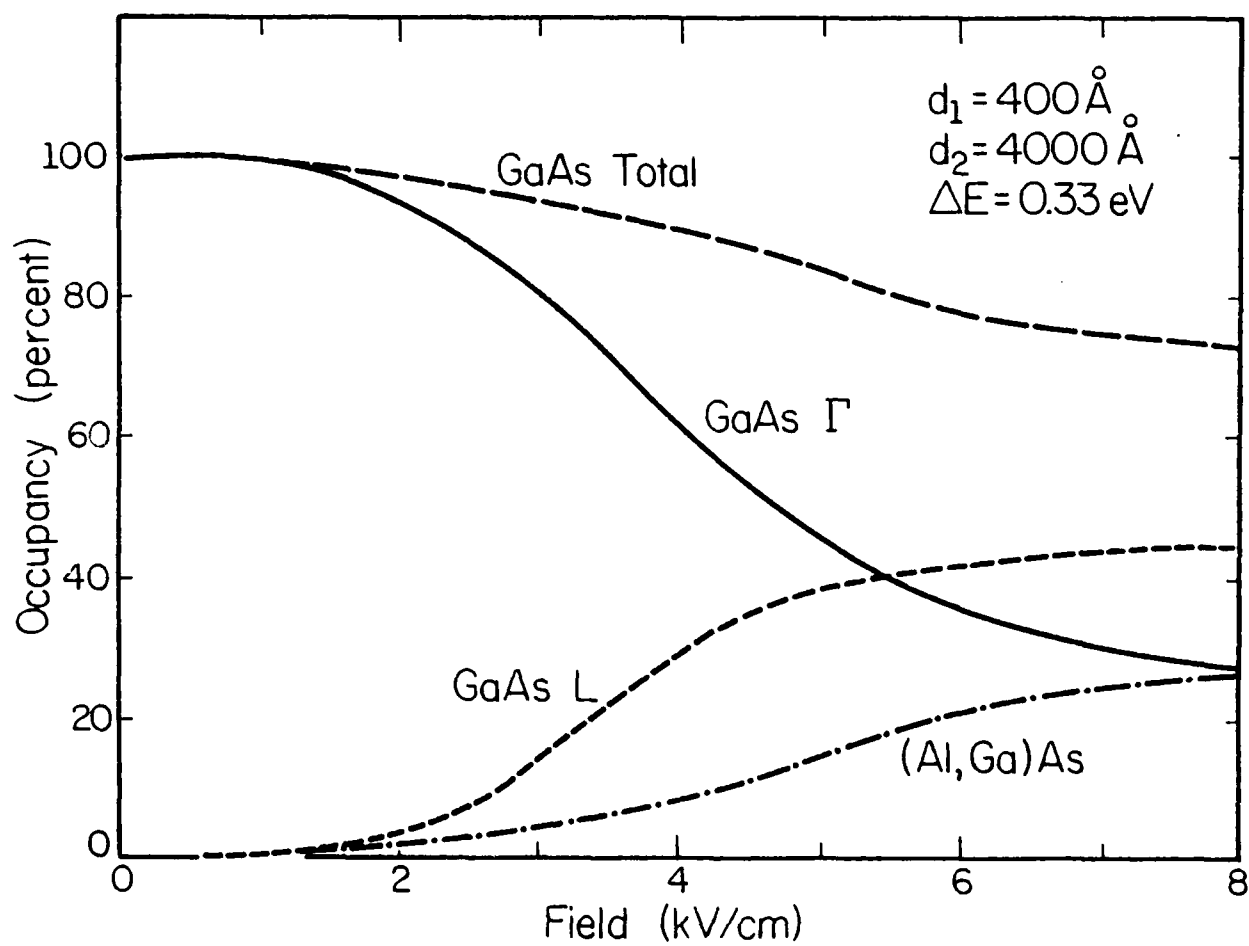


Fig. 2.23. Relative occupancy of electrons in the  $\Gamma$  and L valleys of GaAs and AlGaAs versus field for the same parameters as in Fig. 2.16.



LP-1728

Fig. 2.24. Relative occupancy of electrons in the  $\Gamma$  and L valleys of GaAs and AlGaAs versus field. All the parameters are same as in Fig. 2.20, except  $\Delta E = 0.33 \text{ eV}$ .

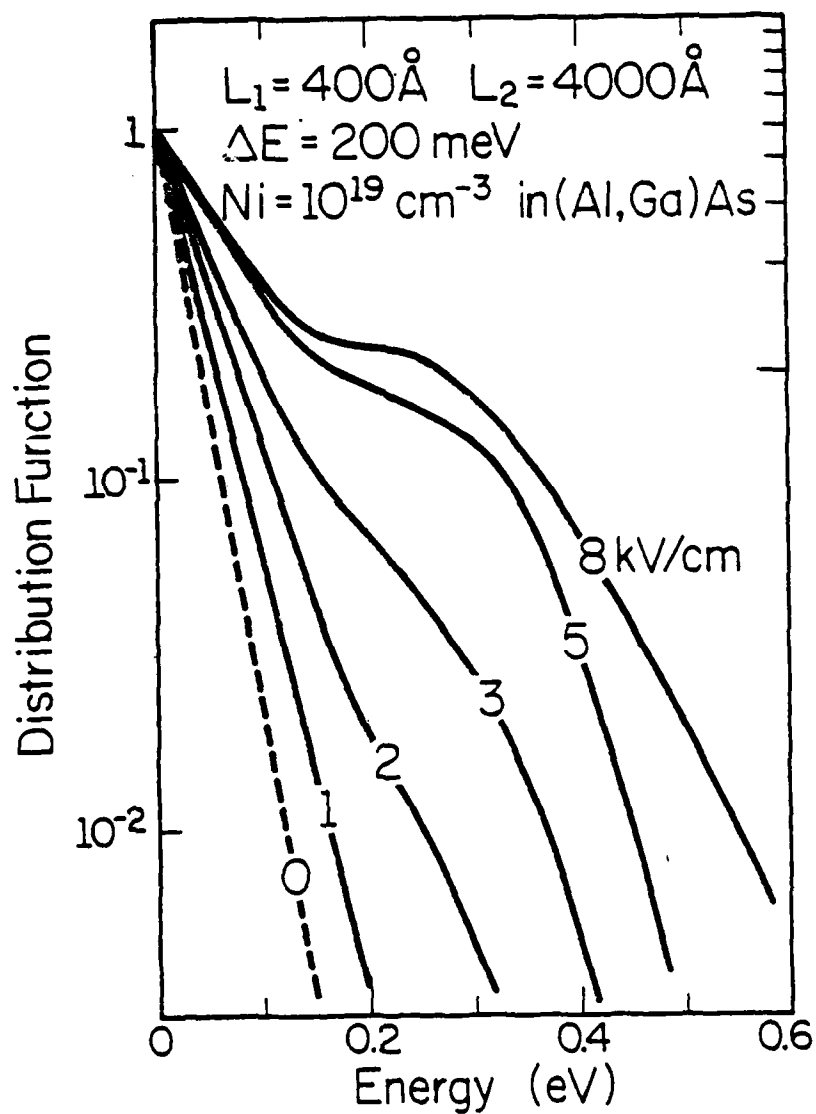


Fig. 2.25. Distribution functions for electrons in the GaAs at the GaAs-AlGaAs interface.

where cooler electrons from the low-mobility L valleys cause a bump in the distribution function in the  $\Gamma$  valley (compare Fig. 2.25 with Fig. 3 of Ref. 33). Also, the degree of the deviation from the straight line indicates the degree of validity of the electron temperature model, which is discussed in more detail in the next section.

#### 2.3.4 Comparisons with the electron temperature model

As seen in Fig. 2.25 the distribution function can be considerably non-Maxwellian at high electric fields. In this case the electron temperature model, which assumes a single carrier temperature in the GaAs, is not adequate. Moreover, the electron temperature model is based on more assumptions (such as the existence of the quasi-Fermi level) than the Monte Carlo simulations. The most fundamental difference between the two models is that the Monte Carlo method is a one particle simulation without carrier-carrier interaction being taken into account, whereas the electron temperature model assumes strong carrier-carrier interaction which yields the Maxwellian distribution. This results in a different power flow rate as is explained below.

In quite general situations the diffusion of energy can be accomplished in two different ways. The first is by actual carrier transport. When a carrier moves, it takes its energy (kinetic energy) with it, thereby reducing the total energy left behind. The other is by the thermal diffusion[42]. This is due to the electron temperature gradient and is analogous to conventional thermal diffusion of gas particles in a temperature gradient. These two effects can be easily demonstrated for one-dimensional case by multiplying the Boltzmann equation (Eq. (2.3)) by the energy and integrating. One then obtains[42,43]

$$\frac{\partial n\langle E \rangle}{\partial t} = \vec{j} \cdot \vec{F} + n \left\langle \frac{dE}{dt} \right\rangle + \frac{\partial}{\partial x} \left\{ \kappa \frac{\partial T_e}{\partial x} + \frac{j}{e} \frac{\langle \tau E^2 \rangle}{\langle \tau E \rangle} \right\}, \quad (2.16)$$

where  $\kappa$  is the thermal conductivity of the electrons given by

$$\kappa = 2nk_B D. \quad (2.17)$$

Eq. (2.16) is the usual power balance equation with two additional terms (inside the brackets) due to the inhomogeneity of the system. The first term represents the thermal diffusion, and the second term the carrier transport effect. In the electron temperature model both of these effects are included. In the Monte Carlo simulation, however, only carrier transport is included, since thermal diffusion is a many-particle effect. From these arguments we can speculate that the power flow out of the GaAs is larger in the electron temperature model than in the Monte Carlo method. This speculation is born out by the comparison in Fig. 2.26, which shows the velocity-field characteristics from the two models using the identical set of parameters. The Monte Carlo simulation shows a large negative differential resistance, whereas the electron temperature model result doesn't even show velocity saturation. In reality the characteristic is expected to be intermediate between the two, which one is closer depends on the carrier density in the system.

## 2.4 Two-dimensional Effects

### 2.4.1 Size quantization

In both the electron temperature model and the Monte Carlo simulation we have considered layer dimensions of typically 400 Å or larger to avoid the complexity arising from two-dimensional effects. When the layer

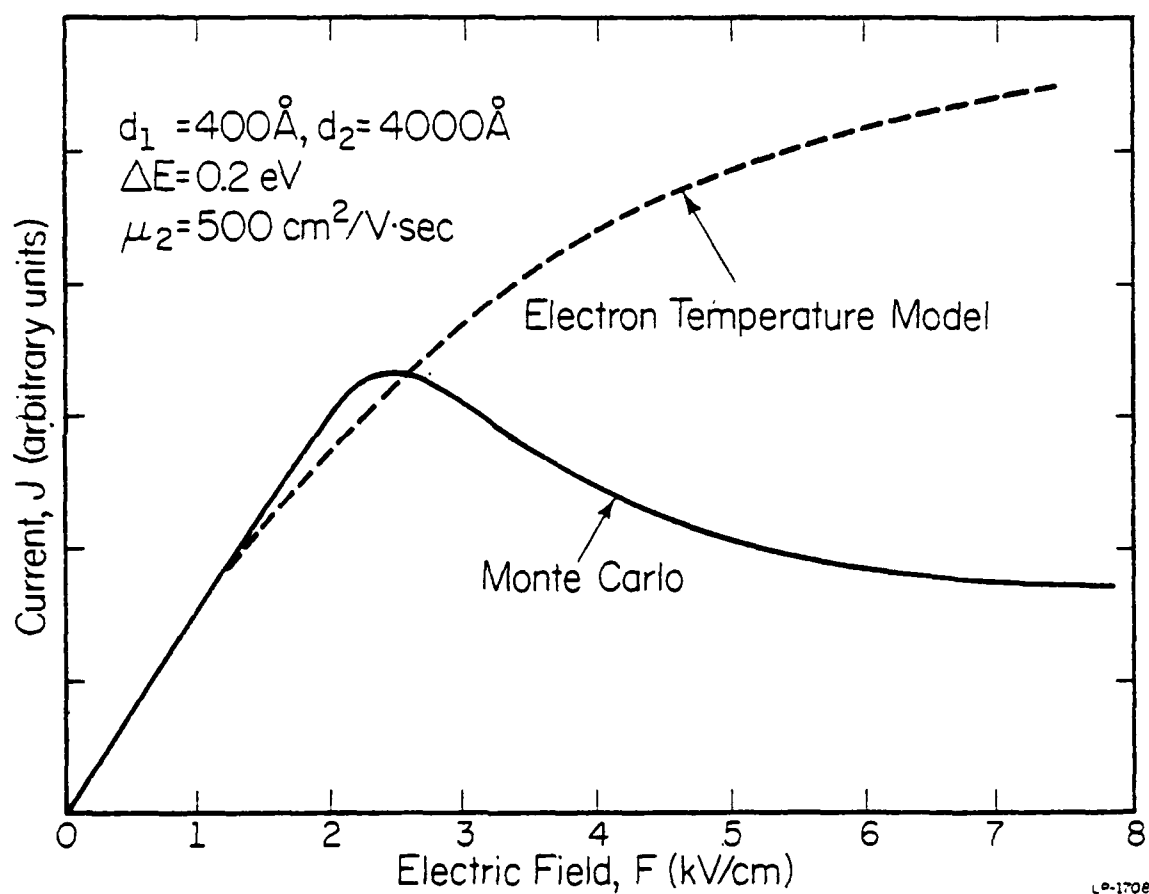


Fig. 2.26. Comparison of current-voltage characteristics using the electron temperature model and the Monte Carlo method.



dimension is comparable to the DeBroglie wavelength of a carrier, bound states are formed and the energy levels become discrete due to the restriction of the carrier motion in the direction normal to the layer (referred to as the z-direction in this section). The energy levels (for a infinitely deep well) are then given by[44]

$$E = E_n + \frac{\hbar^2}{2m^*}(k_x^2 + k_y^2) \quad (2.18)$$

$$E_n = \frac{\hbar^2}{2m^*} \left( \frac{n\pi}{L_z} \right)^2 \quad (2.19)$$

where  $L_z$  is the layer thickness. Each value of  $E_n$  is connected to a continuum of levels, called a subband. In GaAs-AlGaAs heterostructure this quantum size effect (QSE) is expected to appear for layer dimensions below 500 Å[44]. The quantization of carrier motion can also occur at the GaAs-AlGaAs interface due to band bending[45,46]. Electrons or holes in such a system can be considered as two-dimensional. The modification of scattering rate due to this two-dimensionality and its influence on the real space transfer mechanism are discussed in the next two sections.

#### 2.4.2 Polar optical scattering in two dimensions

Polar optical scattering is the most dominant scattering mechanism at low energies in GaAs. We show here how the two-dimensional effects modify the scattering rate of this mechanism. Other mechanisms have been considered by Hess[23]. There is also a considerable amount of work on two-dimensional scattering in connection with silicon MOS inversion layers[47-49].

For polar optical scattering we assume that the phonon modes are three-dimensional, since the GaAs and  $\text{Al}_x\text{Ga}_{1-x}\text{As}$  are chemically similar, especially for a small value of  $x$ . We then start with the Hamiltonian[50]

$$H_{\text{el-ph}} = \sum_{\vec{q}} \frac{C}{q} \left( a_{\vec{q}} e^{i\vec{q} \cdot \vec{r}} - a_{\vec{q}}^{\dagger} e^{-i\vec{q} \cdot \vec{r}} \right), \quad (2.20)$$

where  $\vec{q}$  is a three-dimensional phonon vector,  $a_{\vec{q}}$  and  $a_{\vec{q}}^{\dagger}$  are boson operators, and  $C$  is given by

$$C = -i \left[ \frac{e\hbar^2 \omega_0}{2V} \left( \frac{1}{\epsilon_{\infty}} - \frac{1}{\epsilon_0} \right) \right]^{\frac{1}{2}}. \quad (2.21)$$

We only consider the ground state for the electron whose wavefunction is given by

$$\psi_e = \sqrt{\frac{2}{LA}} \sin \frac{\pi z}{L} e^{i\vec{k}_{\parallel} \cdot \vec{r}_{\parallel}} \quad (2.22)$$

where  $\vec{k}_{\parallel}$  and  $\vec{r}_{\parallel}$  denote the components parallel to the interface,  $L$  is the layer thickness, and  $A$  is the interface area. We can then calculate the matrix element of the electron-phonon interaction:

$$M = \langle \vec{k}', N_q + 1 | H_{\text{el-ph}} | \vec{k}, N_q \rangle. \quad (2.23)$$

Assuming  $q_z L \lesssim 1$ , we obtain, for the phonon emission,

$$|M|^2 = \frac{|C|^2}{q^2} (N_q + 1). \quad (2.24)$$

The total scattering rate is calculated as

$$\begin{aligned}
\frac{1}{\tau} &= \frac{2\pi}{\hbar} \sum_{q, q_z} (N_q + 1) \frac{|C|^2}{q^2} \delta(\epsilon_{\vec{k}-\vec{q}} - \epsilon_{\vec{k}} + \hbar\omega_0) \\
&= \frac{2\pi}{\hbar} \frac{V}{(2\pi)^3} \int d\vec{q}_{//} \int dq_z (N_q + 1) \frac{|C|^2}{q_{//}^2 + q_z^2} \delta(\epsilon_{\vec{k}-\vec{q}} - \epsilon_{\vec{k}} + \hbar\omega_0).
\end{aligned}
\tag{2.25}$$

Performing the  $q_z$  integration with  $q_z \ll k_{//}$ , we get [23]

$$\frac{1}{\tau} = \frac{e^2 \omega_0}{8\pi \epsilon_0} \left( \frac{1}{\epsilon_\infty} - \frac{1}{\epsilon_0} \right) \int_0^\infty \int_0^{2\pi} dq d\phi (N_q + \frac{1}{2} \mp \frac{1}{2}) \delta(\epsilon_{\vec{k} \pm \vec{q}} - \epsilon_{\vec{k}} \mp \hbar\omega_0), \tag{2.26}$$

where upper and lower signs correspond to phonon absorption and emission, respectively, and the notation has been changed ( $\vec{k}_{//} \rightarrow \vec{k}$ , and  $\vec{q}_{//} \rightarrow \vec{q}$ ). To find an explicit expression for  $\tau$ , we perform the integration over the  $\delta$ -function [51], and obtain:

$$\begin{aligned}
\frac{1}{\tau_{ab}} &= \frac{2eE_0 N_q}{\sqrt{2m^*E}} \int_0^{\pi/2} \frac{d\phi}{\sqrt{\cos^2 \phi + \frac{\hbar\omega_0}{E}}} \\
&= \frac{2eE_0 N_q}{\sqrt{2m^*E}} \frac{1}{\sqrt{1 + \frac{\hbar\omega_0}{E}}} K\left(\sqrt{\frac{1}{1 + \frac{\hbar\omega_0}{E}}}\right),
\end{aligned}
\tag{2.27}$$

for phonon absorption, and

$$\begin{aligned}
\frac{1}{\tau_{em}} &= \frac{2eE_o(N_q + 1)}{\sqrt{2m^*E}} \int_0^{\pi/2} \frac{d\theta}{\sqrt{1 - \left(1 - \frac{\hbar\omega_o}{E}\right) \sin^2\theta}} \\
&= \frac{2eE_o(N_q + 1)}{\sqrt{2m^*E}} K\left(\sqrt{1 - \frac{\hbar\omega_o}{E}}\right) \quad (2.28)
\end{aligned}$$

for phonon emission. In these expressions  $E_o$  is the effective field strength for GaAs (see Append. 1), and  $K(x)$  is the complete elliptic integral of the first kind.

In Fig. 2.27 these results are compared with the polar optical scattering rate in three dimensions. As seen from the figure, the two-dimensional scattering rates are considerably higher (for both phonon emission and absorption) than in the three-dimensional case for any electron energies. An enhancement of polar optical scattering rate has been experimentally verified by Holonyak et al.[52] using photopumped multiple quantum-well GaAs-AlGaAs heterostructures.

#### 2.4.3 Influence on the real space transfer mechanism

The enhancement of the polar optical scattering rate alone is expected to increase the threshold electric field for NDR onset by a factor of 2 at room temperature[5]. It is rather difficult, however, to assess all the effects of two-dimensionality on the real space transfer mechanism because of its complexity. For a realistic device, we should take into account the existence of subbands. The energy levels of these subbands can be calculated using a variational principle[53,54] or a self-consistent method[53]. The intervalley and the polar optical scattering rates must be

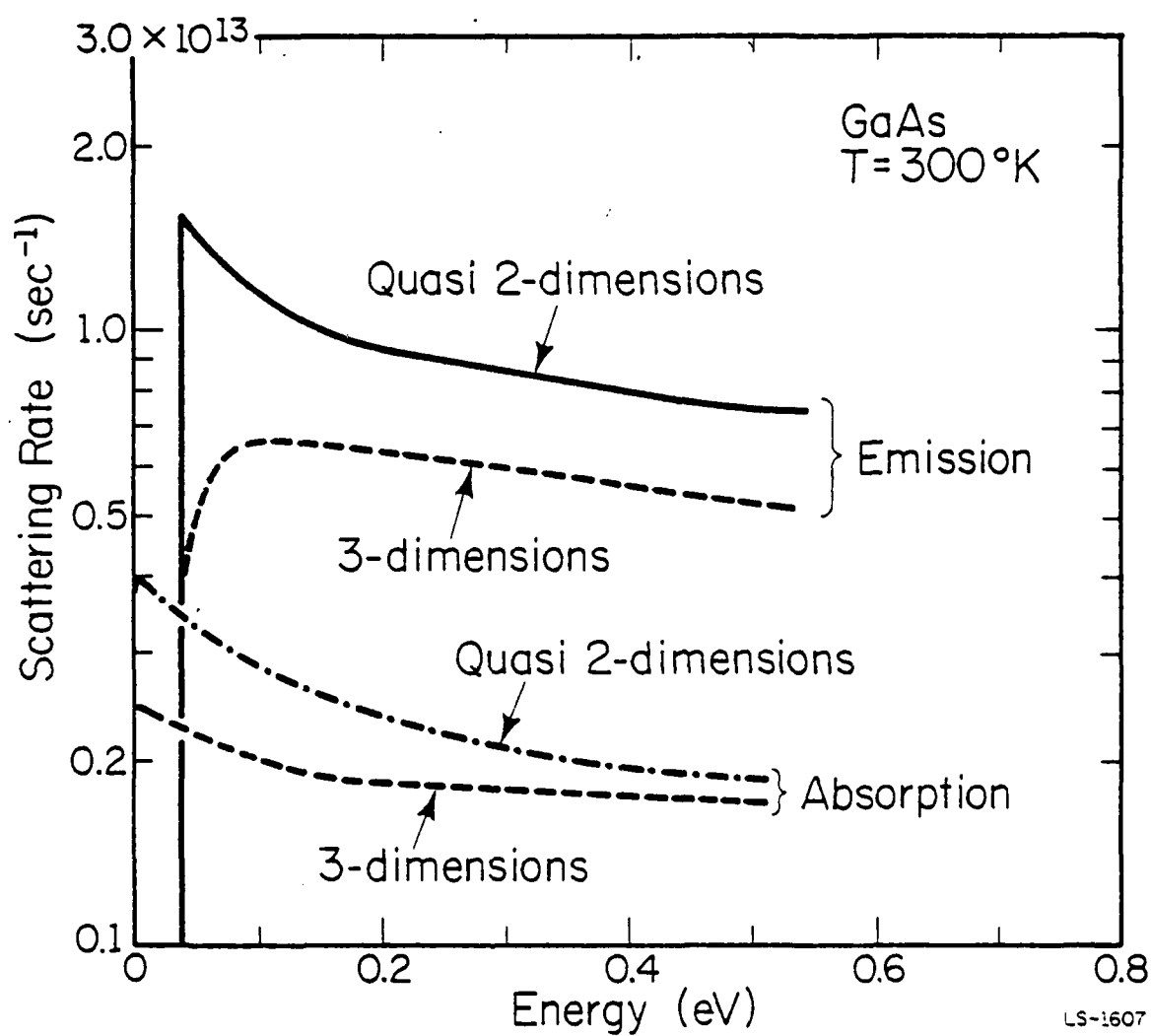


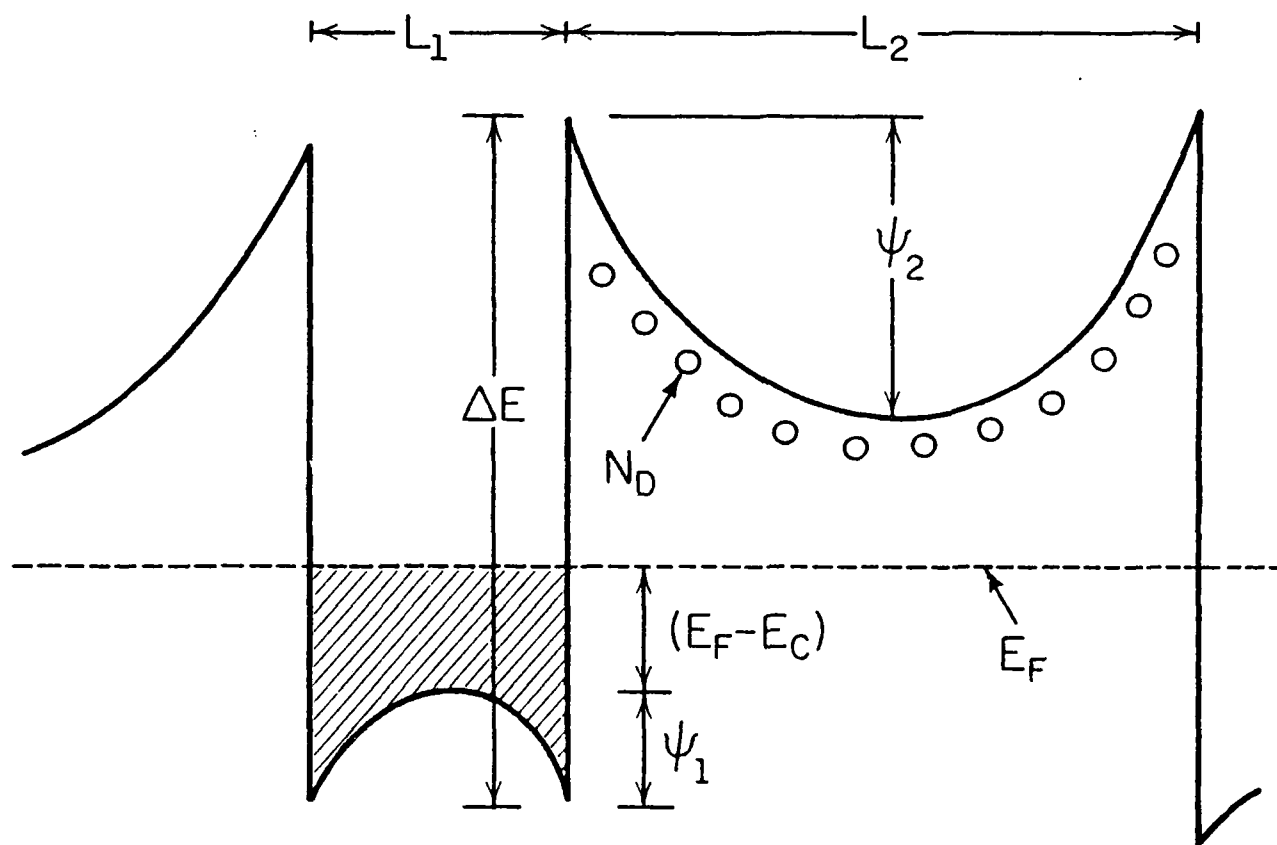
Fig. 2.27. Polar optical scattering rate in GaAs as a function of electron energy in quasi two dimensions and in three dimensions.

obtained including those subbands. It is then possible to calculate the transport property in the two-dimensional system using the electron temperature model[55], or the Monte Carlo technique[56]. The transition from two to three dimensions is necessary at the electron energy equal to the band edge of AlGaAs to account for the real space transfer mechanism. The quantization at the GaAs-AlGaAs interface due to band bending[46] is irrelevant to the real space transfer, because when the carriers become hot they are no longer bound at the interface.

## 2.5 Miscellaneous Effects

### 2.5.1 Band bending

Band bending effects have been neglected both in the electron temperature model and the Monte Carlo simulation for the sake of simplicity, although it is possible to include these effects in the Monte Carlo simulation in the form of a position-dependent electric field. The actual potential profile including band bending is schematically shown in Fig. 2.28. The electric field created by the ionized donors tends to attract energetic electrons and pull them from the GaAs into the AlGaAs. Hence, it is expected to enhance transfer out of the well and impede transfer back into the well. An exact treatment to calculate the band bending should employ a self-consistent method[53] to account for the rearrangement of the electrons. However, a rough estimate can be given rather easily if we neglect two-dimensional effects and assume a uniform carrier distribution (valid only for small band bending).



LP-1703

Fig. 2.28. Band edge variation of GaAs-AlGaAs modulation-doped heterostructure.

Using the depletion approximation[9], we obtain (Fig. 2.28)

$$\psi_2 = \frac{e}{8\epsilon} N_D L_2^2 \quad (2.29)$$

and

$$\psi_1 = \frac{e}{8\epsilon} n L_1^2 = \frac{e}{8\epsilon} N_D L_2 L_1, \quad (2.30)$$

where  $n$  is the carrier density in the GaAs. Here we have used the relation

$$n = N_D L_2 / L_1 \quad (2.31)$$

at the start of the transfer. In order to have all the electrons in the GaAs layer before the real space transfer, we want to have

$$\psi_2 < \Delta E - (E_F - E_c) - \psi_1. \quad (2.32)$$

Using Eqs. (2.29) and (2.30), and  $n = N_c \exp\left(\frac{E_F - E_c}{k_B T}\right)$ , we can rewrite this inequality as

$$L_2^2 < \frac{8\epsilon}{e N_D} \left( \Delta E - \frac{k_B T}{e} \ln \frac{N_D L_2}{N_c L_1} \right) - L_2 L_1. \quad (2.33)$$

If we replace the inequality by the equality, we can find the maximum allowable layer dimension to have all the electrons in the GaAs.

Assuming  $L_2/L_1 = 5$ ,  $N_D = 1 \times 10^{16} \text{ cm}^{-3}$  and  $\Delta E = 0.25 \text{ eV}$ , we obtain  $L_1 = 240 \text{ \AA}$ ,  $L_2 = 0.12 \text{ \mu}$ , and  $\psi_2 = 25 \text{ meV}$ . In order to have low-mobility AlGaAs, the layer must be doped higher than  $1 \times 10^{16} \text{ cm}^{-3}$ . Then the band bending effect is certainly not negligible. By utilizing compensation doping of the AlGaAs, the mobility can be lowered without large band bending effects. In any case, to obtain a more realistic picture of the



real space transfer mechanism, band bending effects should be examined in the Monte Carlo simulation. Tunneling through the barrier may also be significant for large band bending. Furthermore, in stead of trying to eliminate the band bending effects, there might be a possibility of charge storage device utilizing this effect.

#### 2.5.2 Transmission coefficient at the interface

It is well known[57,58] that when an electron collides with a potential step, either reflection or transmission may occur with finite probability. Therefore, at the GaAs-AlGaAs interface some electrons are transmitted, while others are reflected during the transfer. Wu and Yang[59] have calculated the transmission coefficient across heterojunction interfaces taking into account the difference of effective masses on the two sides of the junction. Their treatment is not correct, however, because the effective mass concept is not valid at an abrupt potential step. A more rigorous calculation has been done by Osbourn and Smith[60] using the empirical tight-binding approximation. Their result, as compared with Wu and Yang's result, is shown in Fig. 2.29. The figure shows the transmission coefficient at the interface as a function of electron energy for a wave vector perpendicular to the interface. Osbourn and Smith's result in terms of wave vectors has been replotted using the relation

$$E_{\perp} = \frac{\hbar^2 k_{\perp}^2}{2m^*} \quad (2.34)$$

Their calculation gives smaller transmission coefficient than obtained by Wu and Yang's calculation as pointed out by Price[61]. In actual heterojunctions the interface is not atomically abrupt, but is graded over

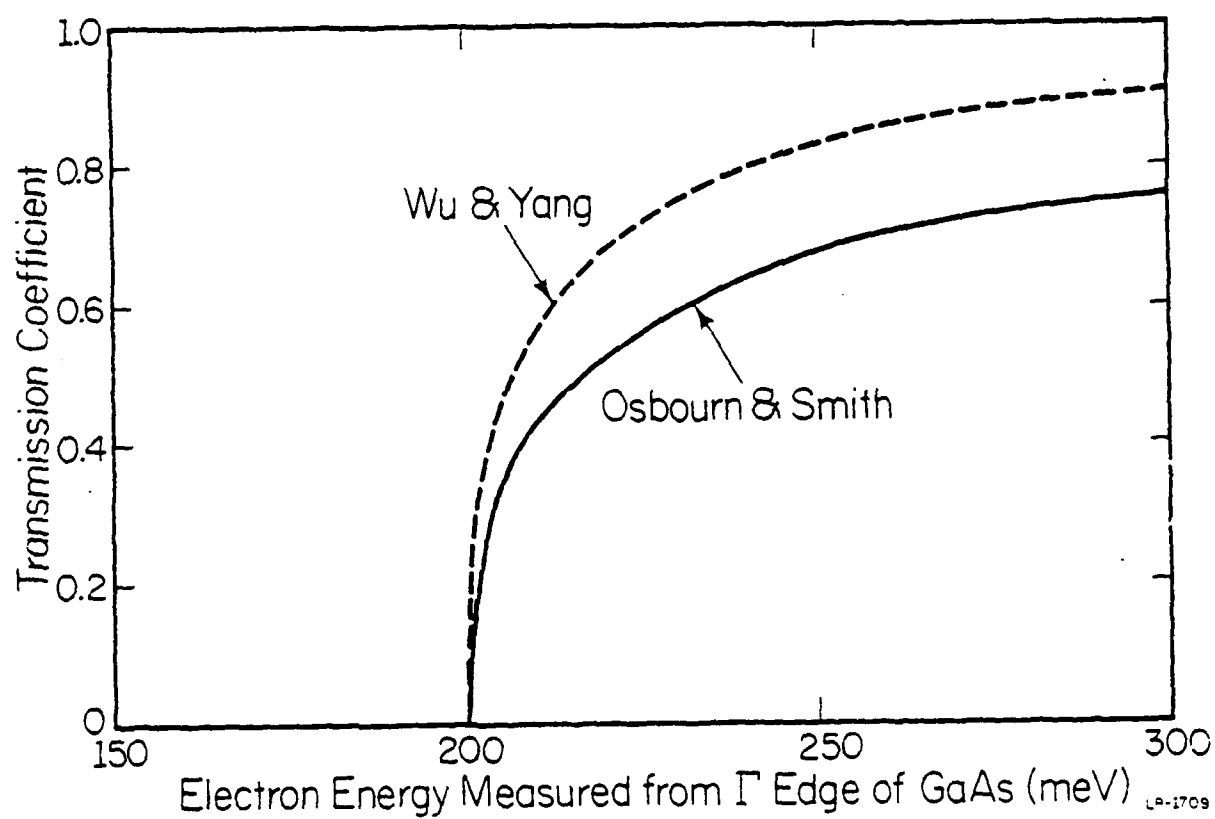


Fig. 2.29. Transmission coefficients at the GaAs-Al<sub>0.2</sub>Ga<sub>0.8</sub>As interface calculated by Wu and Yang [59] and by Osbourn and Smith [60].

more than 15 Å even for MBE grown heterojunctions[62]. This compositional grading has been shown to increase the transmission coefficient slightly[63].

Glisson et al.[64] have compared a classical transmission model and the quantum-mechanical transmission using the formula by Wu and Yang in the Monte Carlo simulations. In the classical model, the transmission coefficient is a step function, being unity at the conduction band edge of the AlGaAs. Within the statistical error of the simulation they have observed no substantial differences in the results between these two transmission models. If the results by Osbourn and Smith are used, there may be a small difference. Intuitively, the inclusion of the quantum-mechanical transmission is nearly equivalent to slightly increasing the barrier height in the classical model. In any case, the effect is expected to be small.

### 2.5.3 Statistical fluctuation

Due to the small layer dimensions, the statistical fluctuations of the electron density and the impurity density might be substantial[65]. For example, if we assume  $L_1 = 400$  Å,  $N_1 = 1 \times 10^{18} \text{ cm}^{-3}$ , and the device area of  $100 \text{ } \mu\text{m}$  by  $100 \text{ } \mu\text{m}$ , the total number of electrons will be  $N = 4 \times 10^4$  electrons, which is rather small for a total number of carriers. The average distance between electrons in this case is 100 Å. For the impurity density, we take  $L_2 = 2000$  Å,  $N_2 = 2 \times 10^{17} \text{ cm}^{-3}$ , and the same device area. Then the total number of impurities in the AlGaAs is  $4 \times 10^3$ . The average distance between impurities is 170 Å.

Of course, this problem can be circumvented by utilizing many stacked layers. By the MBE technique, for example, it is possible to grow more than 100 stacked layers[44].

## 2.6 Switching Characteristics

When considering the application of the NDR mechanism to microwave and switching devices, one of the most important questions to ask is how fast does the mechanism occur, or, how fast does it respond to the applied electric field. We first consider the transfer time of the electrons from the GaAs into the AlGaAs layer. Under collision-free transport conditions, the transfer is due to the thermionic emission current, which is given by[29] (see Eq. (2.12))

$$j_{1-2} = en_1 \left( \frac{kT_e}{2\pi m_1^*} \right)^{1/2} \exp\left(-\frac{\Delta E}{kT_e}\right), \quad (2.35)$$

where  $n_1$  is the electron density in the GaAs, and  $\Delta E$  is the potential barrier height. Comparing Eq. (2.35) with

$$-\frac{1}{eL_1} j_{1-2} = \frac{dn_1}{dt} = -\frac{n_1}{\tau_{1-2}} \quad (2.36)$$

gives the time constant  $\tau_{1-2}$  as

$$\tau_{1-2} = \left( \frac{2\pi m_1^*}{kT_e} \right)^{1/2} L_1 \exp\left(\frac{\Delta E}{kT_e}\right). \quad (2.37)$$

Substituting the typical values,  $\Delta E = 0.2$  eV,  $kT_e = 0.17$  eV, and  $L_1 = 100$  Å, we get  $\tau_{1-2} = 4.8 \times 10^{-13}$  sec, which is an attractively short time. Since the time required for heating of the electrons is much larger ( $\sim 5 \times$

$10^{-12}$  sec) than  $\tau_{1-2}$ , the switch-on time is limited by the heating of carriers.

Depending on the impurity density in the AlGaAs layer, the transfer time from the AlGaAs to the GaAs after switching off the electric field will be limited either by diffusion (high density) or by thermionic emission (low density). For the diffusion limited case, the situation is similar to charge transfer in charge-coupled devices, where electrons move by diffusion from one gate to another of lower potential energy. Using this analogy, we obtain the transfer time,  $\tau_{2-1}$ , from the AlGaAs to the GaAs, given by [5,66]

$$\tau_{2-1} = \frac{4L_2^2}{\pi^2 D} \quad , \quad (2.38)$$

where  $D$  is the diffusion constant in the AlGaAs. This formula is valid only as long as the diffusion concept applies, and mean free path for phonon scattering,  $\lambda_{ph}$ , is smaller than  $L_1$ . If  $\lambda_{ph}$  is longer than  $L_1$ , the probability of an electron being captured in the well is reduced by  $L_1/\lambda_{ph}$ . Then we have

$$\tau_{2-1} = \frac{4L_2^2 \lambda_{ph}}{\pi^2 D L_1} \quad . \quad (2.39)$$

For typical values such as  $L_1 = 400 \text{ \AA}$ ,  $L_2 = 2000 \text{ \AA}$ ,  $\lambda_{ph} = 1000 \text{ \AA}$ , and  $D = \mu_2 kT_L / e = 10 \text{ cm}^2/\text{sec}$ , we obtain  $\tau_{2-1} = 4 \times 10^{-11} \text{ sec}$ . This gives an estimate of the switch-off time for the diffusion limited case.

If the transport is collision-free, the time  $\tau_{2-1}$  can be estimated in a similar way as for  $\tau_{1-2}$ . We then obtain

$$\tau_{2-1} = \frac{eN_c L_2 m_0}{A^* T_L^2 m^*} \exp\left(\frac{e\phi}{kT_L}\right), \quad (2.40)$$

where  $A^*$  is the Richardson constant ( $120 \text{ A/cm}^2\text{K}^2$ ),  $m^*$  is the effective mass in the AlGaAs,  $m_0$  is the free electron mass,  $\phi$  is the potential created by the donors in the AlGaAs ( $\psi_2$  in Fig. 2.25), and  $N_c$  is the effective density of states in the AlGaAs. If we assume  $e\phi/kT_L = 2$ , we obtain  $\tau_{2-1} = 2.2 \times 10^{-12}$  sec. Therefore the switch-off time is also determined by the cooling time of electrons in the GaAs.

Of course, these numbers only give rough estimates of the transfer time. A more rigorous calculation can be done by a transient Monte Carlo method[67] including the real space transfer mechanism. It is also interesting to compare the real space transfer time and the transfer to the L valleys, and observe the relative population as a function of time, especially for a large potential barrier height ( $\Delta E \sim 0.3 \text{ eV}$ ).

An example of an actual device configuration for a switching device is shown in Fig. 2.30[68]. The GaAs and the AlGaAs layers are contacted separately, so that voltages can be applied independently to the two materials. Such structures can be realized using the MBE technique. There will be a negligible current in the AlGaAs until an appreciable fraction of electrons are emitted from the GaAs. Fig. 2.31 illustrates this switching effect calculated by the electron temperature model. The electric field to the AlGaAs is kept constant at  $12 \text{ kV/cm}$ . The GaAs and the AlGaAs currents can be switched on and off by the electric field applied to the GaAs layer.

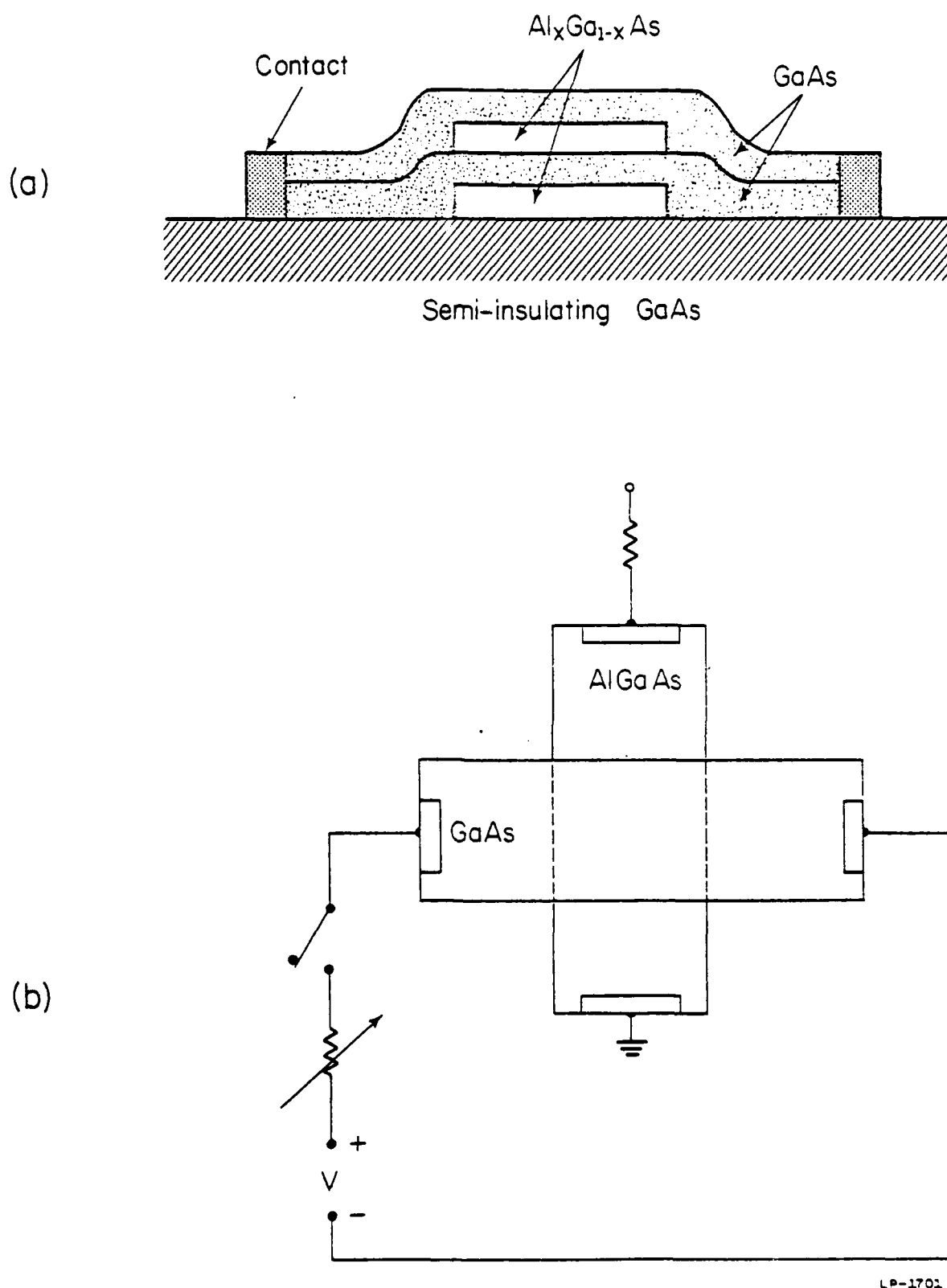


Fig. 2.30. Schematic configurations showing (a) a device structure and (b) an electrical circuit of a switching device utilizing the real-space transfer mechanism [68].

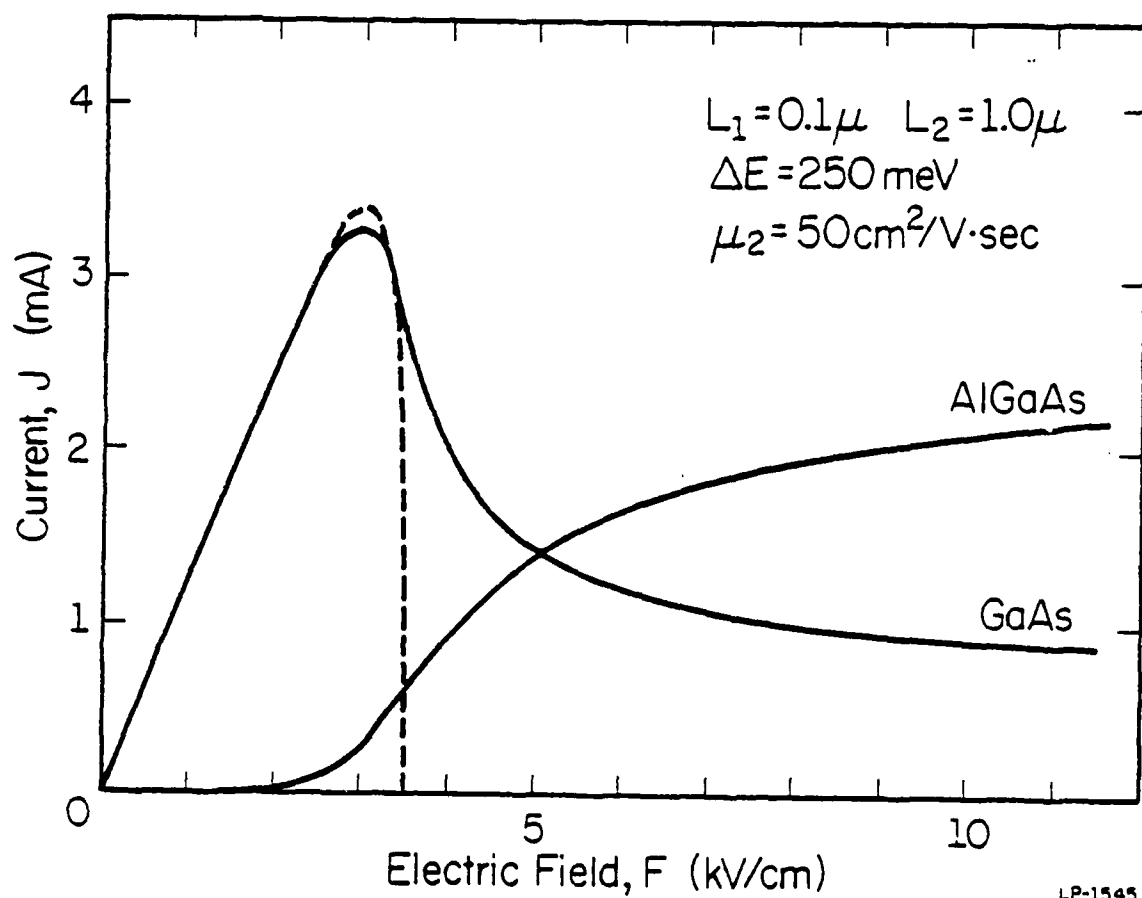


Fig. 2.31. Switching characteristics of a real-space transfer device. The GaAs and the AlGaAs layers are contacted separately. The electric field to the AlGaAs layers is kept constant at 12 kV/cm. Each layer can be switched on and off by the applied field to the GaAs layer.



The dotted curve is obtained in the case of no thermal conduction. Fig. 2.32 illustrates another aspect of the switching characteristics. Here the same electric field is applied to both the GaAs and the AlGaAs layers. The figure shows how the current in the AlGaAs increases as the field increases with the AlGaAs mobility as a parameter.

The possible problems which might be encountered in the application of the real space transfer mechanism to switching devices include the remaining electrons in the GaAs, and the existence of traps at the interfaces and in the AlGaAs layer. Electrons remaining in the GaAs layer above threshold field cause a large power consumption. Traps cause the loss of carriers and/or slower switching speed.

## 2.7 Summary

In this chapter we have described the mechanism of real space electron transfer which can occur in GaAs-AlGaAs heterostructures. A negative differential resistance results from the transfer of electrons from a high-mobility GaAs region to an adjacent low-mobility AlGaAs region under the influence of a high electric field. The mechanism is analogous in many respects to the Gunn effect, except that the device characteristics can be controlled primarily through doping densities, layer thicknesses, and the Al mole fraction in the AlGaAs. We have analyzed the mechanism using two different methods, the electron temperature model and the Monte Carlo simulation. Both methods clearly illustrate the degree of control of the device characteristics. Some comparisons have also been made between the two models. The electron temperature model has been shown to give a larger power flow to adjacent layers than the Monte Carlo simulation.

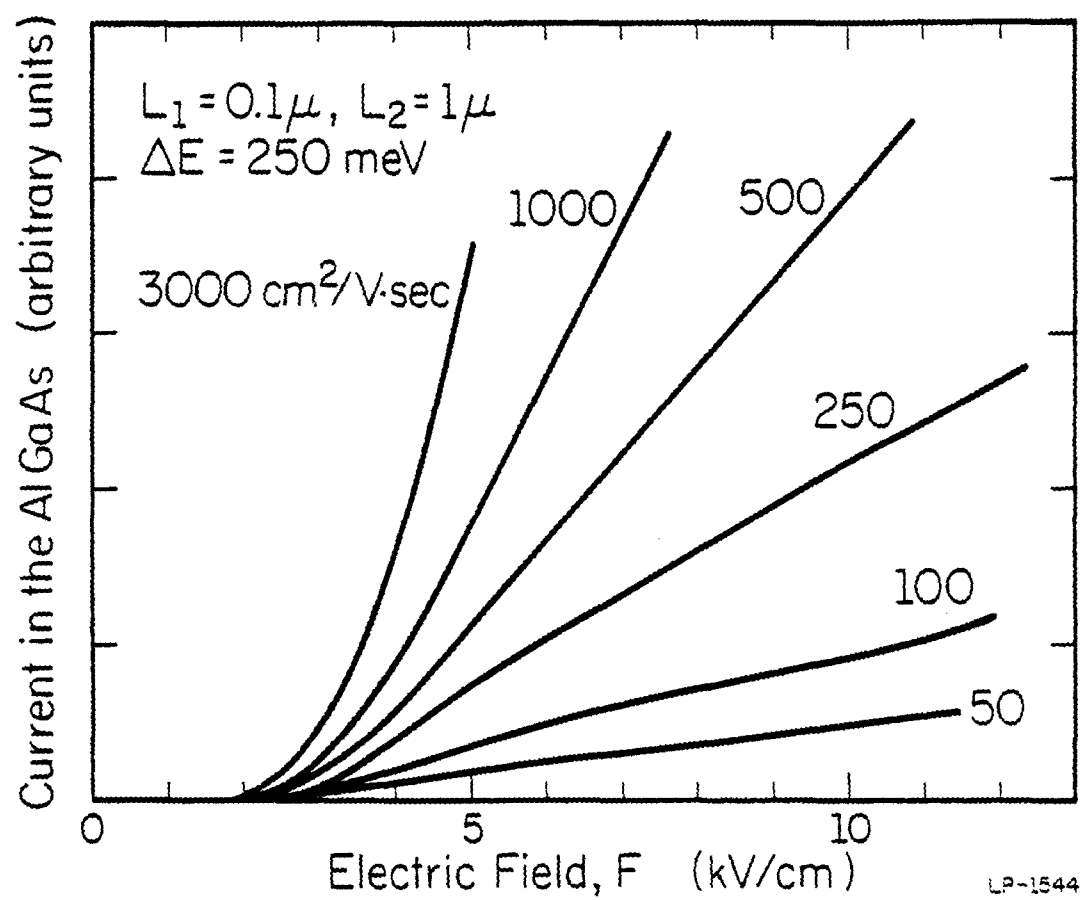


Fig. 2.32. Current in the AlGaAs layer versus electric field with AlGaAs mobility as a parameter.

Two dimensional effects might be important in actual devices, although they have been neglected in the two methods. More work needs to be done on this subject. Other effects, such as band bending and quantum-mechanical transmission have been discussed. These effects might also influence the actual device characteristics. Especially, band bending effects should be included in the Monte Carlo simulations. Switching characteristics including the switching speed have been examined. The switching speed is estimated to be on the order of  $1 \times 10^{-12}$  sec, which is an attractively short time for device applications.

There is also a possibility of enhancing the transfer-out from the GaAs, such as simultaneous application of an electric field and a magnetic field parallel to the interface to divert the electron trajectory. Monte Carlo simulations including a magnetic field effect should be easy. The possibility of charge storage (resembling charge-coupled devices) utilizing band bending effects should also be pursued. Finally, we note that a similar mechanism is important in other semiconductor devices. For example, in silicon MOS devices hot electrons move to the Si-SiO<sub>2</sub> interface, causing some unwelcome effects[70,71]. In the same way, electrons are emitted into substrate in FETs causing higher output conductance[72].

Regarding experimental work on the real space transfer mechanism, Keever et al.[69] have recently carried out measurements of the current-voltage characteristics of GaAs-AlGaAs heterojunctions. They have observed current saturation and negative differential resistance in qualitative agreement with the Monte Carlo simulation discussed here. Their results tend to support the general concept of real space transfer

described in this chapter. In any case, there is no question that hot electron effects in semiconductor heterostructures will attract more interest in the future.

### 3. BAND STRUCTURE DEPENDENT TRANSPORT AND IMPACT IONIZATION IN GaAs

#### 3.1 Introductory Remarks

A large number of semiconductor devices depend on high-energetic (hot) electrons for their operation. Impact ionization is an essential mechanism in the operation of many semiconductor devices, such as photodetectors and IMPATT diodes. At present, however, the theoretical understanding of this effect is provided by a number of theories[74-79] which contain several adjustable parameters whose physical significance is not well known. Currently the most widely used theory of impact ionization has been given by Baraff[76]. The adjustable parameters of his theory are the threshold energy for ionization, the optical phonon energy, the ionization mean free path, and the mean free path for optical phonon scattering. Although some attempts have previously been made to determine these parameters theoretically[30,81], a "complete" theory of impact ionization, which is capable of calculating these quantities (and therefore the ionization rate) from first principles, has not been developed. The main reason is that any theory applicable at high electric field (causing ionization) must abandon the effective mass approximation or simple extensions using non-parabolicity constant, and instead include a realistic band structure. The surprising success of Baraff's theory in explaining the electric field dependence of the ionization rate is due to the adjustable parameters, which can smear out the band structure effects. The inclusion of the band structure in analytical solutions of the Boltzmann equation, however, is impractical. It is also difficult to include realistic scattering mechanisms. For example, the inclusion of both small angle scattering and randomizing scattering mechanisms in the same analytical framework is

difficult, not to mention several different mechanisms. As a consequence all the previous theories are only applicable to specific materials. For instance, Dumke's theory[78] is only applicable to InSb or InAs, whereas Baraff's[76] or Chwang's[79] treatment is only valid for nonpolar materials, such as Si or Ge.

As we have seen in the analysis of real space transfer, the Monte Carlo method provides an alternative to the solution of the Boltzmann equation. The method can take into account a large variety of scattering mechanisms, and therefore, is applicable to both polar and nonpolar semiconductors. It can calculate the quantities of interest such as drift velocity, mean free path, average electron energy without any a priori assumptions on the form of the distribution function. Some attempts have previously been made to calculate the impact ionization rate by the Monte Carlo method[33,84], but without including a realistic band structure. In this chapter we describe a Monte Carlo method that includes a realistic band structure as calculated by the empirical pseudopotential method[35]. This method should provide a tool for understanding electronic transport in very high fields, which has not been possible with conventional methods utilizing effective mass theory. Of course, we do not yet have all the necessary information to perform a rigorous calculation at such high fields. For example, not much is known about the selection rules for scatterings at the non-symmetric points, the changes of the ionization matrix, and the scattering rate at high energies. Because of this lack of information, we must still use a simpler model than is possible with this technique. These simplifications should not be considered as restrictions of the method itself. As more information becomes available in the future, the method can be improved with ease to accommodate new information. In

spite of the simplifications, the results we obtain provide insight into how the various parameters in previous theories are connected and into how the band structure influences the impact ionization rate. In particular, the method is applied to study the electron initiated ionization in GaAs. Finally the results also give us information about the accuracy of the pseudopotential band structure at high energies.

### 3.2 Summary of Experimental Results

Before we discuss the theory of impact ionization, it is instructive to summarize the available experimental data. Various experimental techniques to measure the ionization rate are described in detail in a review paper by Stillman and Wolfe[3]. Their article also contains some of the experimental data on the electron initiated ionization rate in GaAs. Fig. 3.1 summarizes more recent data[36-90]. The experimental data usually shows a  $1/E$  or  $1/E^2$  dependence of the ionization rate. As can be seen from the figure, the data of different workers scatter almost by an order of magnitude.

Of special interest are the results of Pearsall et al.[39], who measured the electron ionization rate with the electric field applied in three different crystallographic directions. Their data are replotted in Fig. 3.2. They have measured the highest ionization rate in the  $\langle 110 \rangle$  direction and the lowest in the  $\langle 111 \rangle$  direction. They have attributed this difference to ballistic electrons and electron tunneling to upper conduction band[39,91]. Although these data raise an interesting question as to how the band structure actually influences the ionization rate, their notion of ballistic electrons seems to be incorrect, as is shown in this work. More systematic and reliable data are necessary to make a comparison

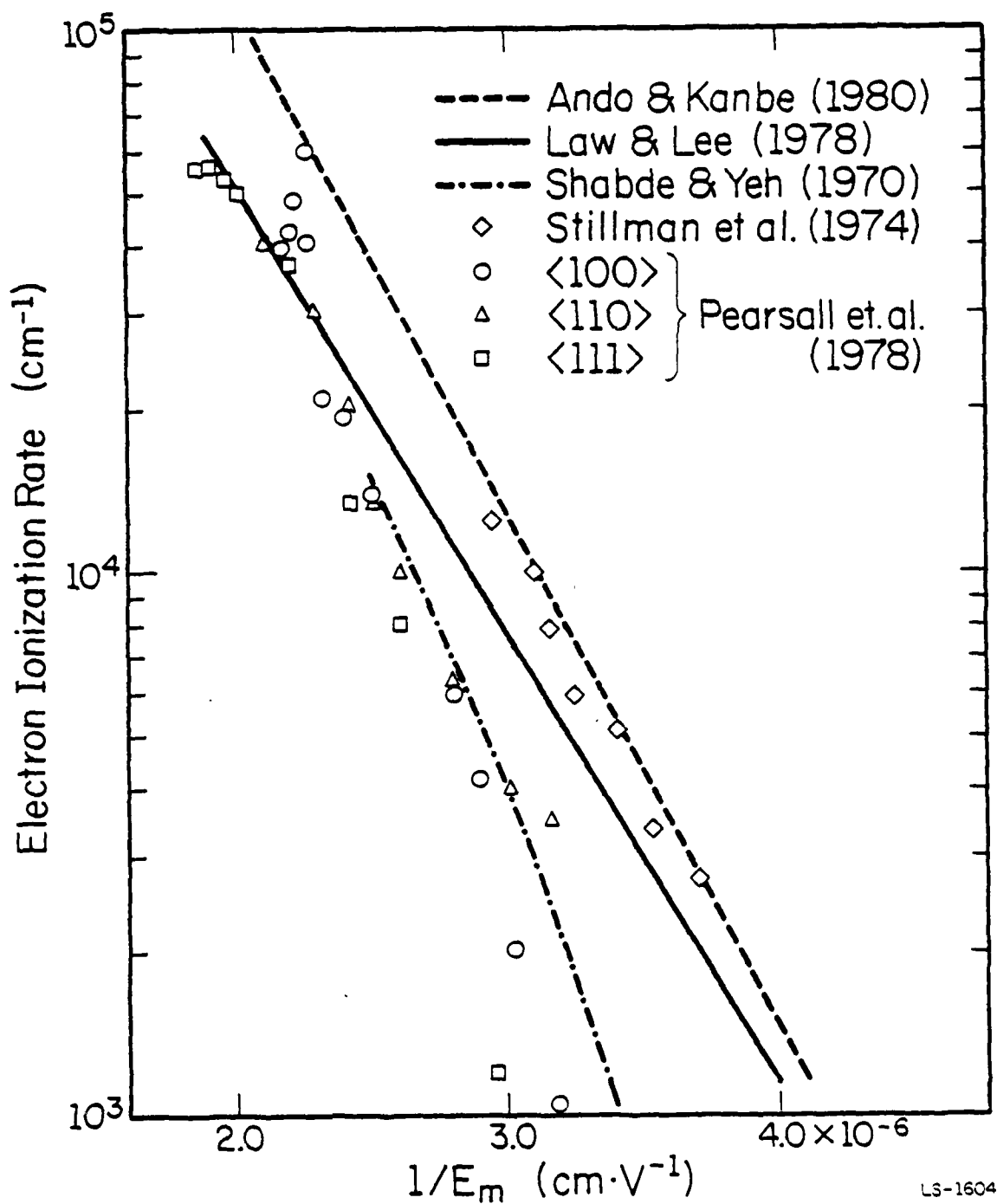


Fig. 3.1. Experimental ionization rates of electrons for GaAs at room temperature [86-90].



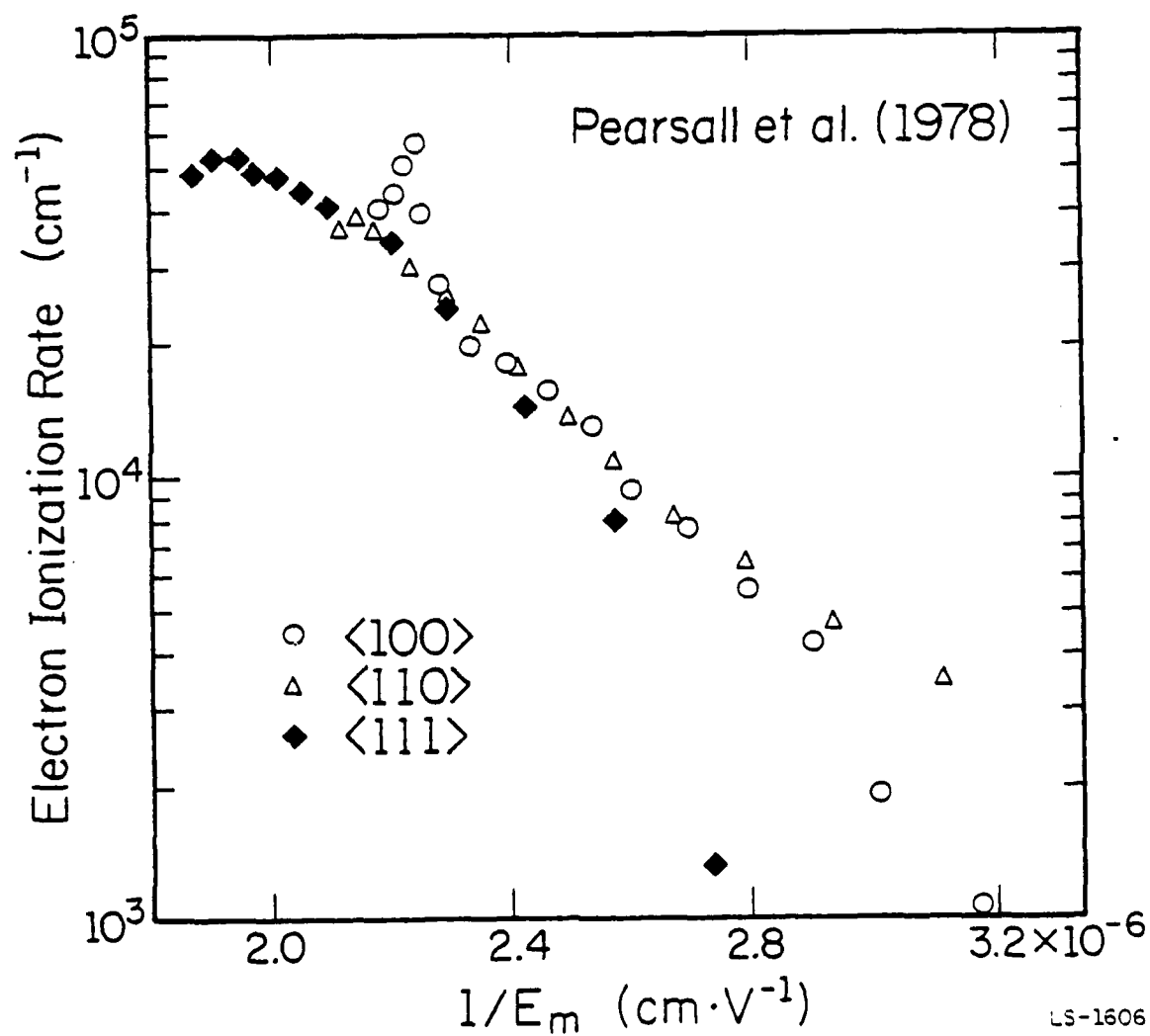


Fig. 3.2. Experimental electron ionization rates by Pearsall et al. [89] as a function of reciprocal electric field for three orientations of electric field.

with theory.

### 3.3 Previous Theories of Impact Ionization

Wolff[74] was the first to calculate the ionization rate in semiconductors. He applied the gas discharge theory to solve the Boltzmann equation taking into account the effect of electron-phonon and pair-producing collisions on the distribution functions. The velocity distribution function was approximated as

$$n(v, \theta) = n_0(v) + n_1(v) \cos \theta, \quad (3.1)$$

where  $v$  is the electron velocity, and  $\theta$  is the angle between the velocity and the electric field. This is an energy diffusion theory, in which the electrons undergo many collisions when moving to higher energies. The Boltzmann equation was then solved to calculate the ionization rate with the result

$$\alpha(F) \sim \exp(-A/F^2), \quad (3.2)$$

where  $F$  is the electric field.

Shockley[75], on the other hand, argued that ionization is mainly due to "lucky" electrons which completely escape phonon scatterings and reach the threshold energy. In this streaming approximation the distribution is a spike in the direction of the electric field. He considered the relative probability of phonon scattering and pair production, and obtained an ionization rate whose dependence on  $F$  is given by:

$$\alpha(F) \sim \exp(-B/F). \quad (3.3)$$

Next, Baraff[76,92] solved the time dependent Boltzmann equation and showed that his result contained Shockley's result as a low field limit, and Wolff's result as a high field limit. His theory gives the "universal" curves with phonon mean free path and ionization threshold energy as parameters, which are adjusted to fit theory to experimental data. However, it does not provide a way to calculate these quantities, nor does it include the band structure.

Recently, Chwang et al.[79] took a different and interesting approach using a finite Markov chain formation. Their method is based on the calculation of a transition matrix which characterizes the transition probability between virtual states defined by small discrete energy intervals. Interesting as it is, their method is unfortunately limited by the analytical formulations. It still requires the same assumptions as Baraff's theory and does not produce much more information. For example, an assumption of a constant mean free path for phonon scattering is still necessary. Moreover, the Markov formulation is only applicable to nonpolar semiconductors.

Nevertheless, Baraff's and Chwang's theories contain some "truth" about the impact ionization mechanism, as does Shockley's or Wolff's approach. How they are related, and how they complement each other will be clear as a result of the Monte Carlo calculation described in this work. This Monte Carlo method includes a realistic band structure. As a result, the orientation dependence of the impact ionization rate can be calculated for the first time.

### 3.4 The Band Structure of GaAs

The band structure of GaAs has been calculated using the empirical pseudopotential method as described by Cohen and Bergstresser[35]. Only the lowest conduction band has been considered. The effect of higher band is briefly discussed in the later sections. Advantage is taken of the 48-fold symmetry of the Brillouin zone of the zinc-blend structure[93]. It is then necessary to examine only that 1/48 th part of the zone indicated in Fig. 3.3. This region is defined by the conditions:

$$0 \leq k_z \leq k_x \leq k_y \leq 1, \quad (3.4)$$

and

$$k_x + k_y + k_z \leq \frac{3}{2}, \quad (3.5)$$

where all the  $k$  components are in units of  $2\pi/a$  ( $a$  is the lattice constant;  $a = 5.64 \text{ \AA}$  for GaAs). Mesh points ( $k_x, k_y, k_z = 0.0, 0.1, \dots$ ) are sampled from this region, and the energy and its gradient (velocity) at each  $k$ -point is calculated. A total of 249 points have been sampled, with 156 points within the sampling region. The extra 93 points outside the region are necessary for the interpolation of energy in the proximity of the surface of the sampling region. Table 3.1 lists the calculated  $E(\vec{k})$  relation for these 249 points. Fig. 3.5 illustrates the isoenergy lines in the cross section of the Brillouin zone shown in Fig. 3.4, with the numbers representing the electron energy from the bottom of the conduction band ( $\Gamma$  point). It can be seen that the  $\Gamma$  valley is nearly isotropic, whereas the  $X$  valleys are more elliptic. A similar plot of isoenergy lines in the cross section shown in Fig. 3.6 is illustrated in Fig. 3.7. The overall electron energy in this cross section is considerably lower than in the

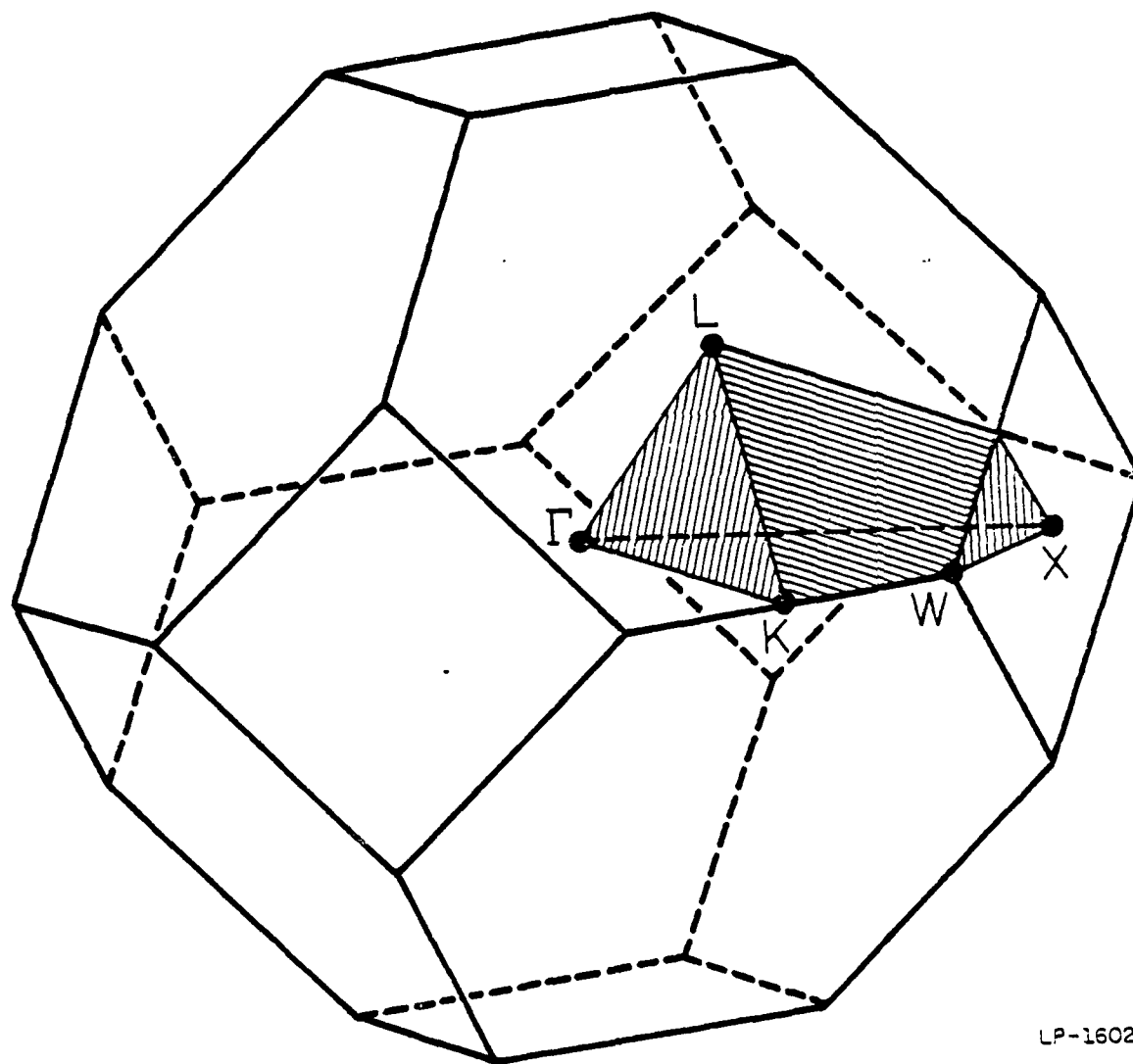


Fig. 3.3. Sampling region for the calculation of the band structure of GaAs. The region is a 1/48 th part of the Brillouin zone.

Table 3.1 (a).  $E(\vec{k})$  relation for the lowest conduction band of GaAs

$k_z$	$k_y$											$k_x$
	0.0	0.1	0.2	0.3	0.4	0.5	0.6	0.7	0.8	0.9	1.0	
0.5				0.9517	0.5256	0.4920	0.8602	1.3776				0.4
					0.4920	0.2352	0.4920					0.5
						0.4920						0.6
0.4			1.2081	0.7419	0.6448	0.9517	1.3836	1.6178	1.5956	1.5174		0.3
				0.6448	0.3333	0.5256	1.0043	1.4160	1.5591			0.4
					0.5256	0.4920	0.8602	1.3787				0.5
						0.8602	1.0043					0.6
0.3		1.5422	1.0875	0.9567	1.2081	1.5525	1.6272	1.4612	1.2645	1.1264	1.0796	0.2
			0.9567	0.6097	0.7419	1.1476	1.4292	1.4058	1.2594	1.1368	1.0937	0.3
				0.7419	0.6448	0.9517	1.3836	1.6178	1.5956	1.5174		0.4
					0.9517	1.0383	1.3776	1.8322	2.1598			0.5
						1.3776	1.4160	1.6178				0.6
							1.6178					0.7
0.2		1.3548	1.2464	1.5422	1.8326	1.7128	1.4302	1.1628	0.9516	0.8188	0.7726	0.1
			1.2442	0.9695	1.0875	1.4402	1.5865	1.4180	1.1596	0.9330	0.7841	0.2
				1.0875	0.9567	1.2081	1.5525	1.6272	1.4612	1.2645	1.1264	0.3
					1.2081	1.2455	1.5404	1.8999	2.0175	1.9071	1.7938	0.4
						1.5404	1.5737	1.7734	2.1599	2.6307	2.6858	0.5
							1.7734	1.5591	1.5956	1.9071		0.6
								1.5956	1.2594			0.7



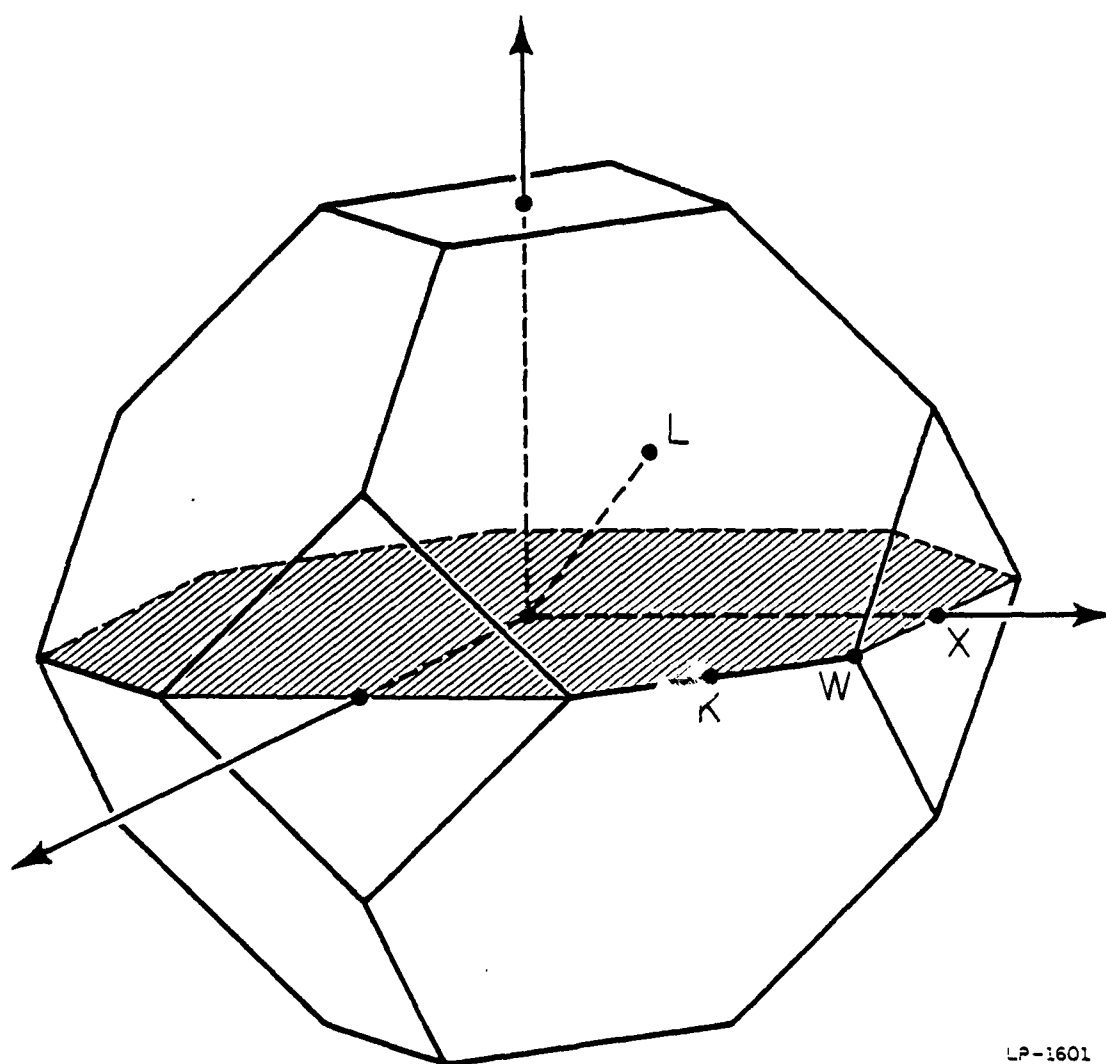
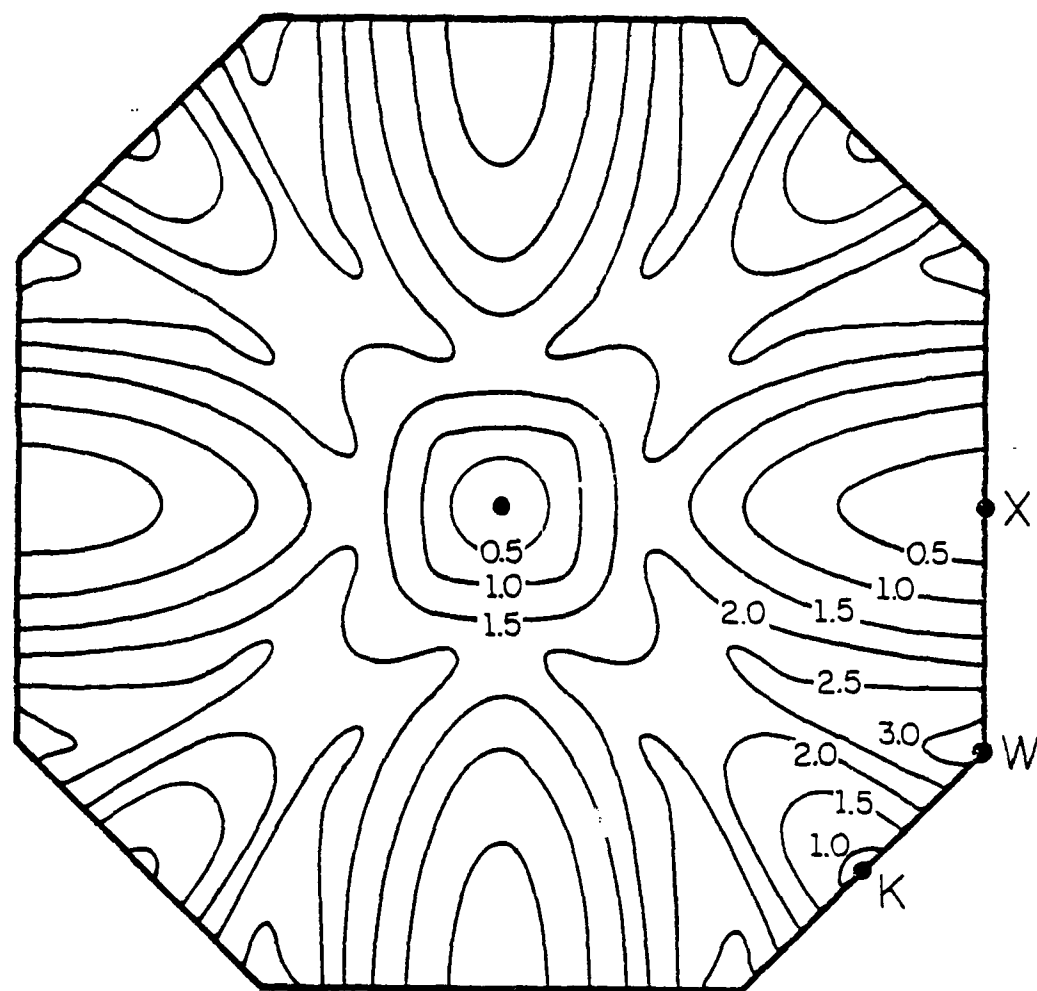


Fig. 3.4. Cross section of the Brillouin zone.





LP-1597

Fig. 3.5. Isoenergy lines of the lowest conduction band of GaAs in the cross section shown in Fig. 3.4. The numbers represent the energies measured from the  $\Gamma$  minimum.

AD-A123 947

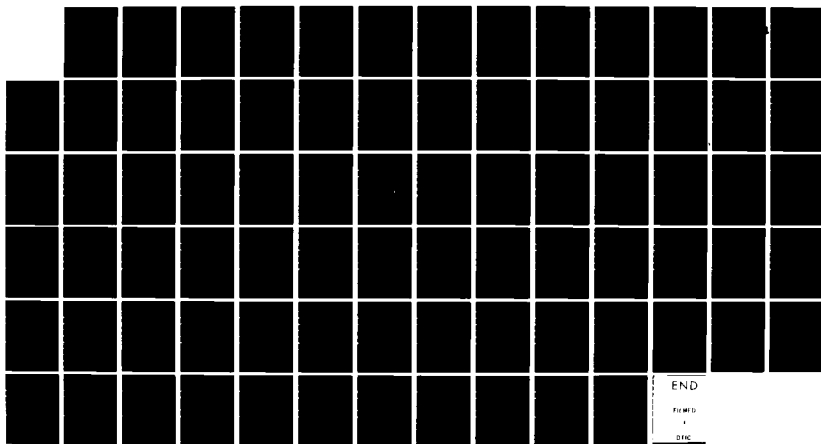
THEORETICAL STUDIES OF HIGH FIELD TRANSPORT IN III-V  
SEMICONDUCTORS(U) ILLINOIS UNIV AT URBANA COORDINATED  
SCIENCE LAB H SMICHIO SEP 88 R-893 N00014-79-C-0424

2/2

UNCLASSIFIED

F/G 20/12

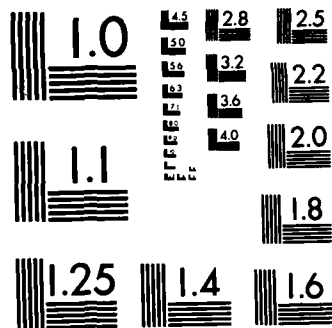
NL



END

FILED

DATE



MICROCOPY RESOLUTION TEST CHART  
NATIONAL BUREAU OF STANDARDS-1963-A

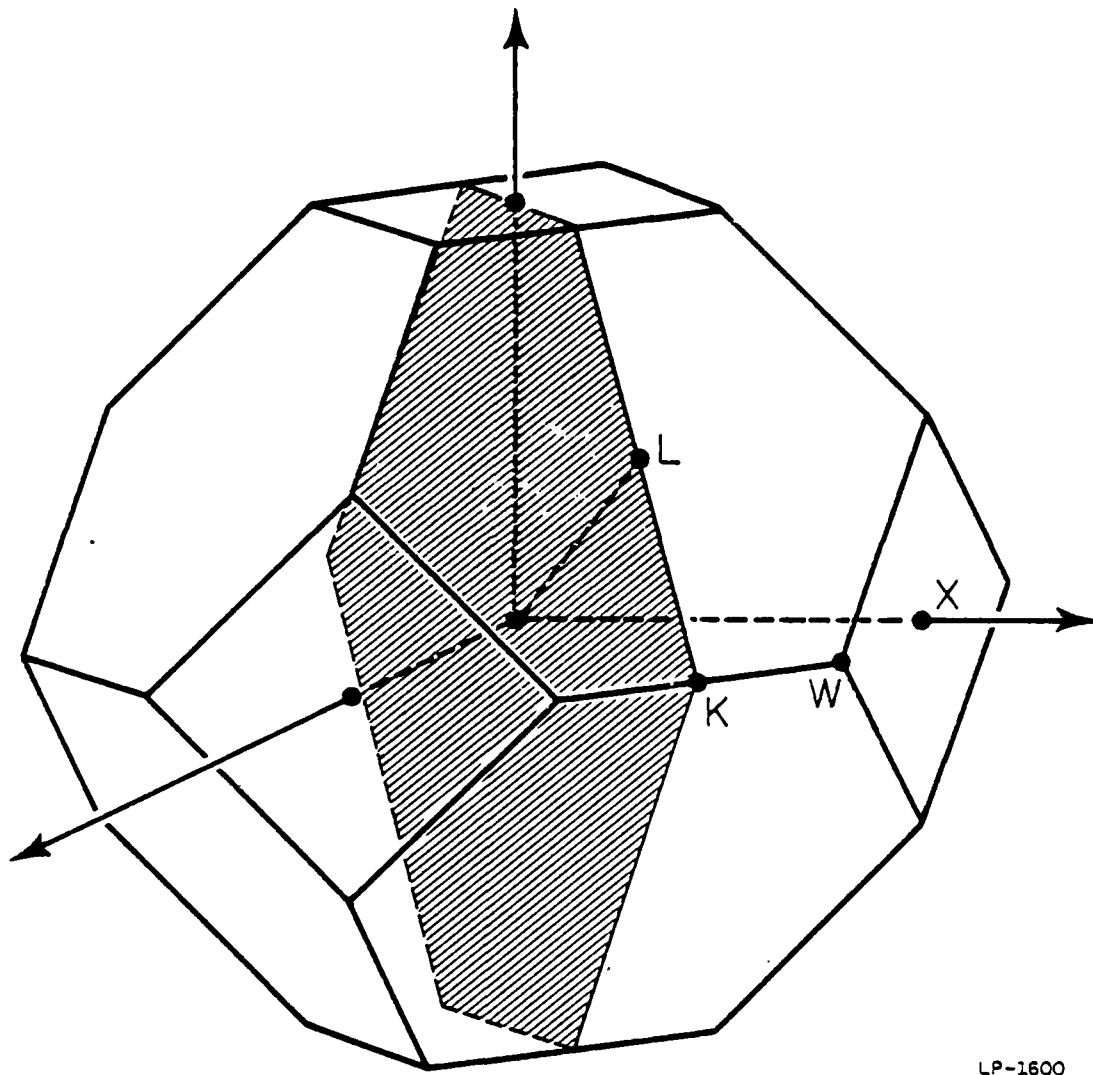
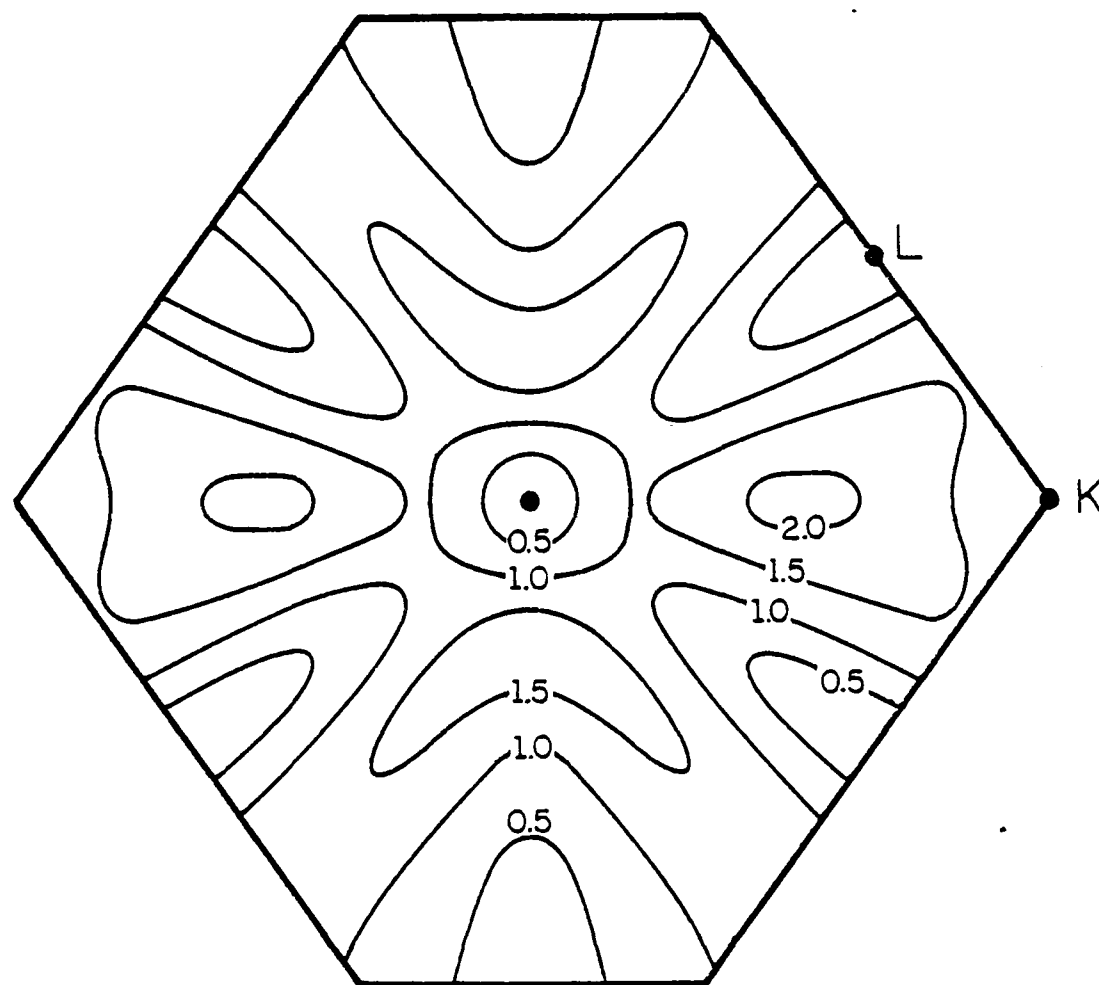


Fig. 3.6. Cross section of the Brillouin zone.



LP-1598

Fig. 3.7. Isoenergy lines of the lowest conduction band of GaAs in the cross section shown in Fig. 3.6. The numbers represent the energies measured from the  $\Gamma$  minimum.

cross section of Fig. 3.4. This band structure is stored in memory, and used in the Monte Carlo simulation which is described in Section 3.6.

In the study of ballistic electron transport in three major crystal directions, i.e., the  $\langle 100 \rangle$ ,  $\langle 110 \rangle$ , and  $\langle 111 \rangle$  directions, extra k-points have been sampled, and the  $E(\vec{k})$  relation is calculated. The result of the calculation is shown in Fig. 3.8. It is obvious from the figure that the use of effective mass and non-parabolicity constant is not valid for electron energies above approximately 1 eV in some directions. In fact, the effective mass defined as

$$\frac{1}{m^*} = \frac{1}{\hbar^2} \frac{\partial^2 E(k)}{\partial k^2} \quad (3.6)$$

goes to negative values at higher energies.

### 3.5 Ballistic Electron Transport and Phonon Scattering

The term "ballistic electrons" is used to denote those electrons which do not suffer phonon scattering. This is equivalent to the "lucky" electron notion in Shockley's theory. Since the possible contribution of ballistic electrons to impact ionization has been suggested[91], the behavior of ballistic electrons has been examined using the pseudopotential band structure[94]. The study has been performed by solving the equations of motion:

$$\hbar \frac{d\vec{k}}{dt} = e\vec{F} \quad (3.7)$$

and

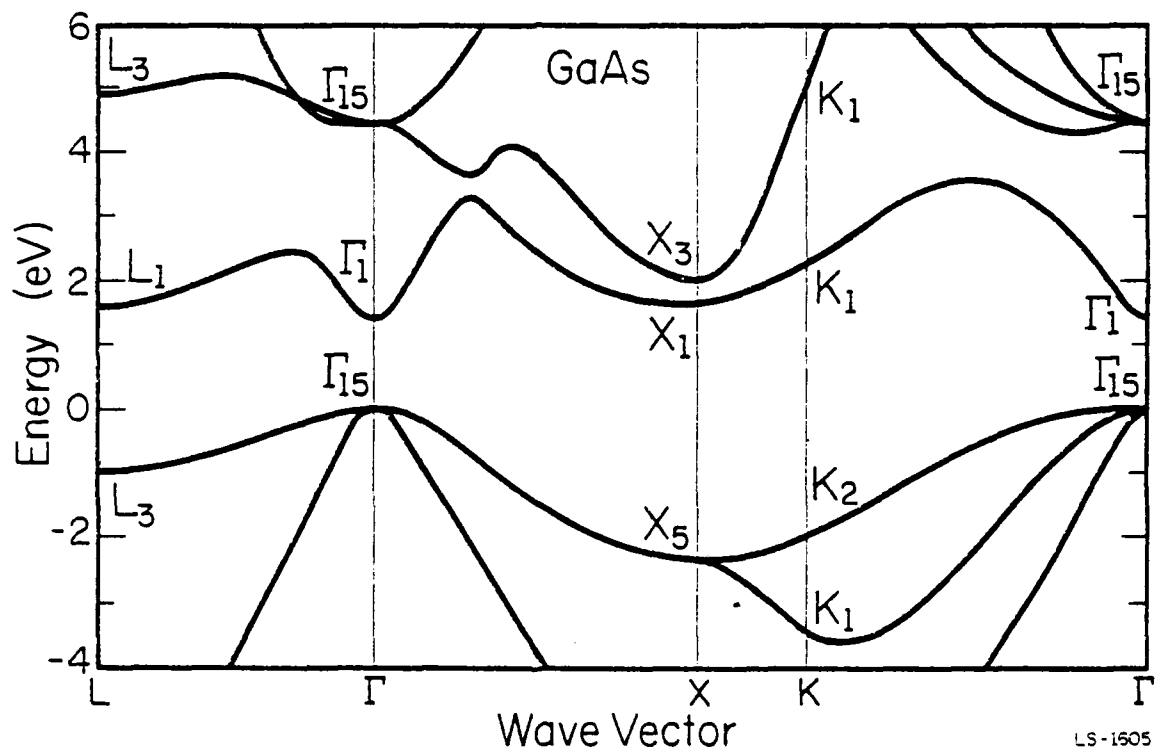


Fig. 3.8. Band structure of GaAs.

$$\vec{v} = \frac{1}{\hbar} \vec{\nabla}_k E(\vec{k}) \quad (3.8)$$

where  $\vec{F}$  is the applied electric field,  $\vec{k}$  is the electron wave vector,  $E$  is the electron energy, and  $\vec{v}$  is the group velocity of the electron. With the initial condition  $\vec{k} = \vec{0}$  at  $t = 0$ , we obtain

$$\hbar \vec{k} = e t \vec{F} . \quad (3.9)$$

The field is assumed to be constant. Eqs. (3.8) and (3.9) are solved simultaneously to express  $v$  and  $E$  as a function of time  $t$ . The results of the calculations are shown in Figs. 3.9 and 3.10 for the three major crystallographic directions. The electric field has been chosen to be 500 kV/cm, a typical field for impact ionization. Fig. 3.9 shows the electron velocity,  $v$ , as a function of time. The orientation dependence of the ballistic behavior is obvious from this figure. The highest peak velocity is reached in the  $\langle 100 \rangle$  direction ( $\sim 1.1 \times 10^8$  cm/sec) and the lowest in the  $\langle 111 \rangle$  direction ( $\sim 0.8 \times 10^8$  cm/sec). Fig. 3.10 shows the variation of electron energy with time as measured from the conduction band edge. The rate of increase is largest in the  $\langle 100 \rangle$  direction and smallest in the  $\langle 111 \rangle$  direction.

In reality, however, ballistic transport must compete with scattering processes. It will be shown by the Monte Carlo simulation that on the average an electron can travel ballistically for only  $\sim 3 \times 10^{-14}$  sec before it suffers a phonon scattering. In the  $\langle 111 \rangle$  direction, the electron can never gain sufficient energy ballistically for impact ionization[39]. In the  $\langle 100 \rangle$  direction, the impact ionization threshold can be reached only if electrons tunnel in  $k$ -space to the next higher band



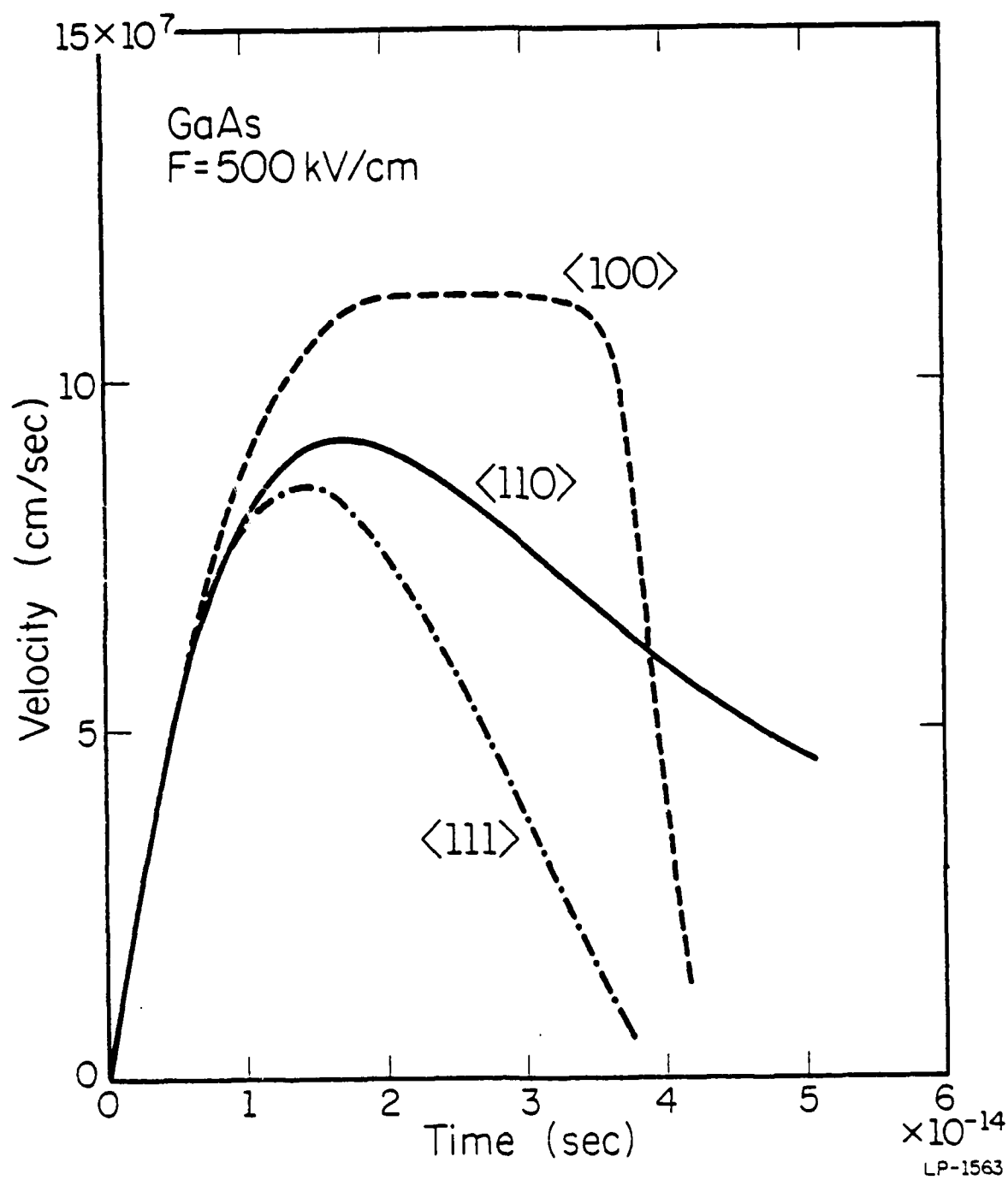


Fig. 3.9. Variation of ballistic electron velocity with time in three crystallographic directions of GaAs.

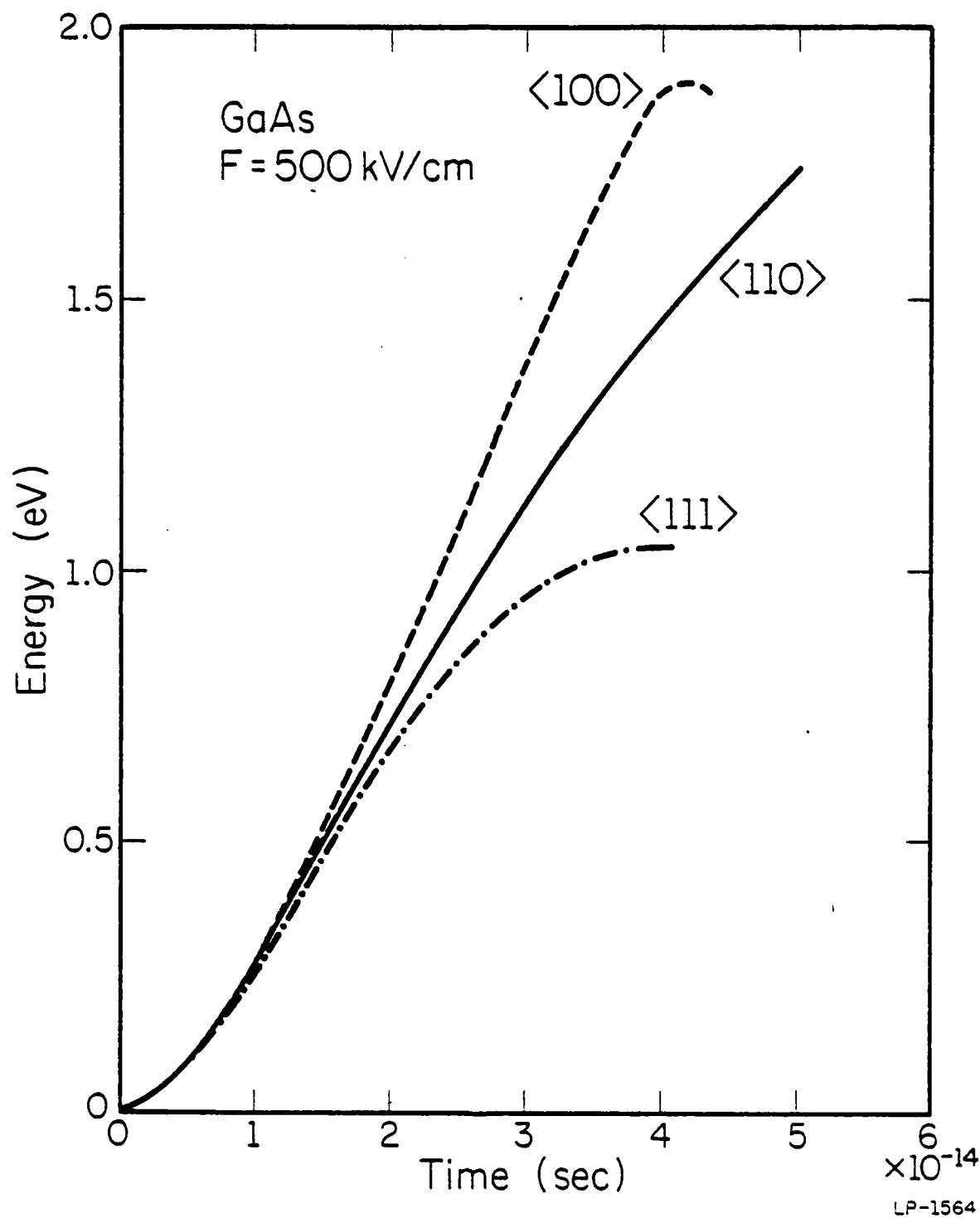
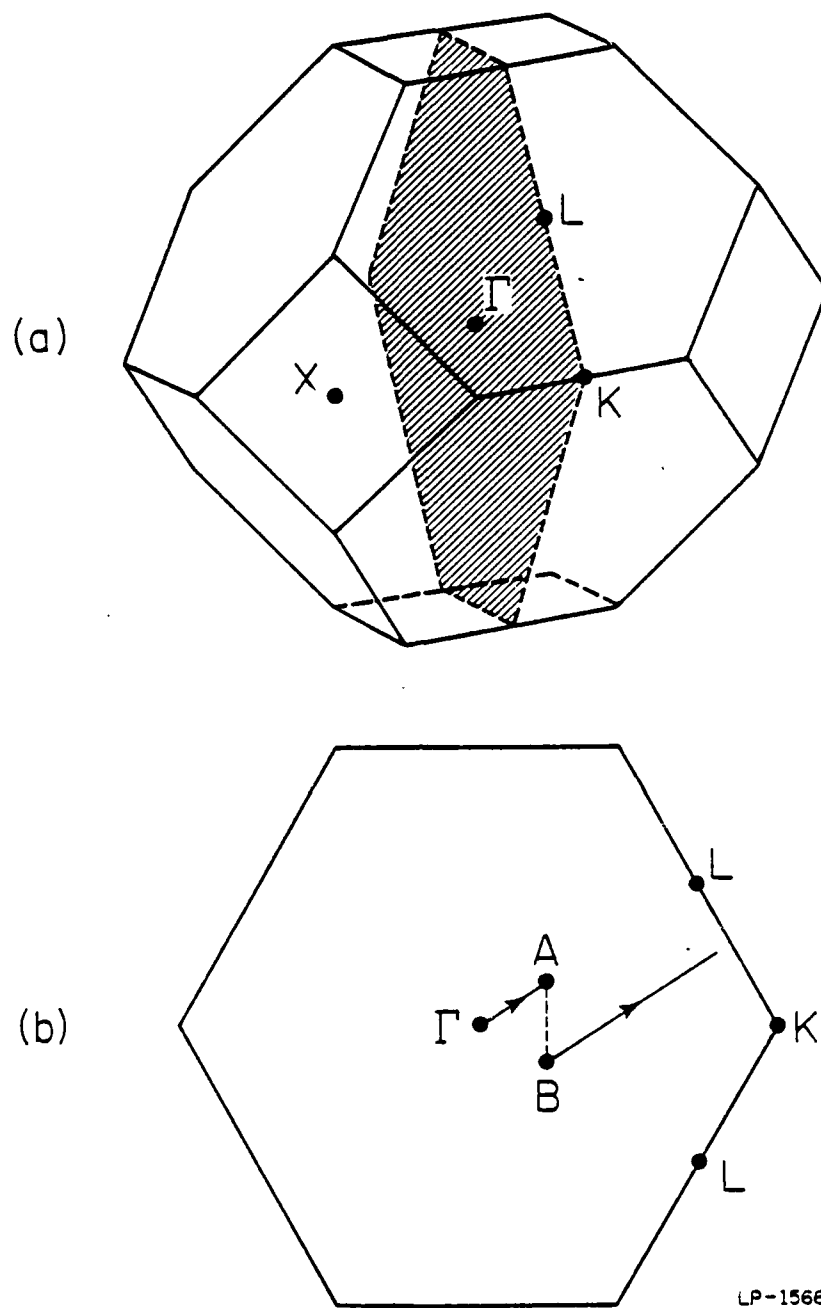


Fig. 3.10. Variation of electron energy with time as measured from the conduction band edge.

~ 0.2 eV above the principal conduction band[39]. Therefore, scattering events become crucial for the occurrence of impact ionization in these directions.

Electrons can be scattered to other regions of the Brillouin zone with a single scattering event being sufficient to permit the electrons to reach threshold energy. This mechanism is illustrated in Figs. 3.11 and 3.12 for an electric field applied in the  $\langle 111 \rangle$  direction. An electron starts at the  $\Gamma$  point and moves along the  $\langle 111 \rangle$  direction. At point A ( $\vec{k} = \frac{\pi}{a}(0.3, 0.3, 0.3)$ ), the energy is at the maximum for this direction, but it is still much less than the threshold energy. Subsequently, the electron can be scattered (by a phonon or impurity) to some other point in the Brillouin zone, point B, for example. Following this scattering event, the  $\langle 111 \rangle$  component of the electron wave vector continues to increase. However, the wave vector points in a direction different from the  $\langle 111 \rangle$  so that the electron can now reach a higher energy. As shown in Fig. 3.12, the electron can actually exceed the threshold energy for impact ionization (~ 2.0 eV).

This is, of course, only one example of an electron trajectory to show the importance of scattering processes to impact ionization. The actual calculation of the impact ionization rate must involve averaging of all the possible electron trajectories until the electron reaches the threshold energy. This is achieved by the Monte Carlo method which is described in the next section.



LP-1566

Fig. 3.11. (a) (110) section of the first Brillouin zone.  
 (b) Wave vector trajectory of electron in this plane under the influence of electric field in the  $\langle 111 \rangle$  direction. Electron is scattered from  $A$  to  $B$ . Energy change in the scattering process has been neglected.

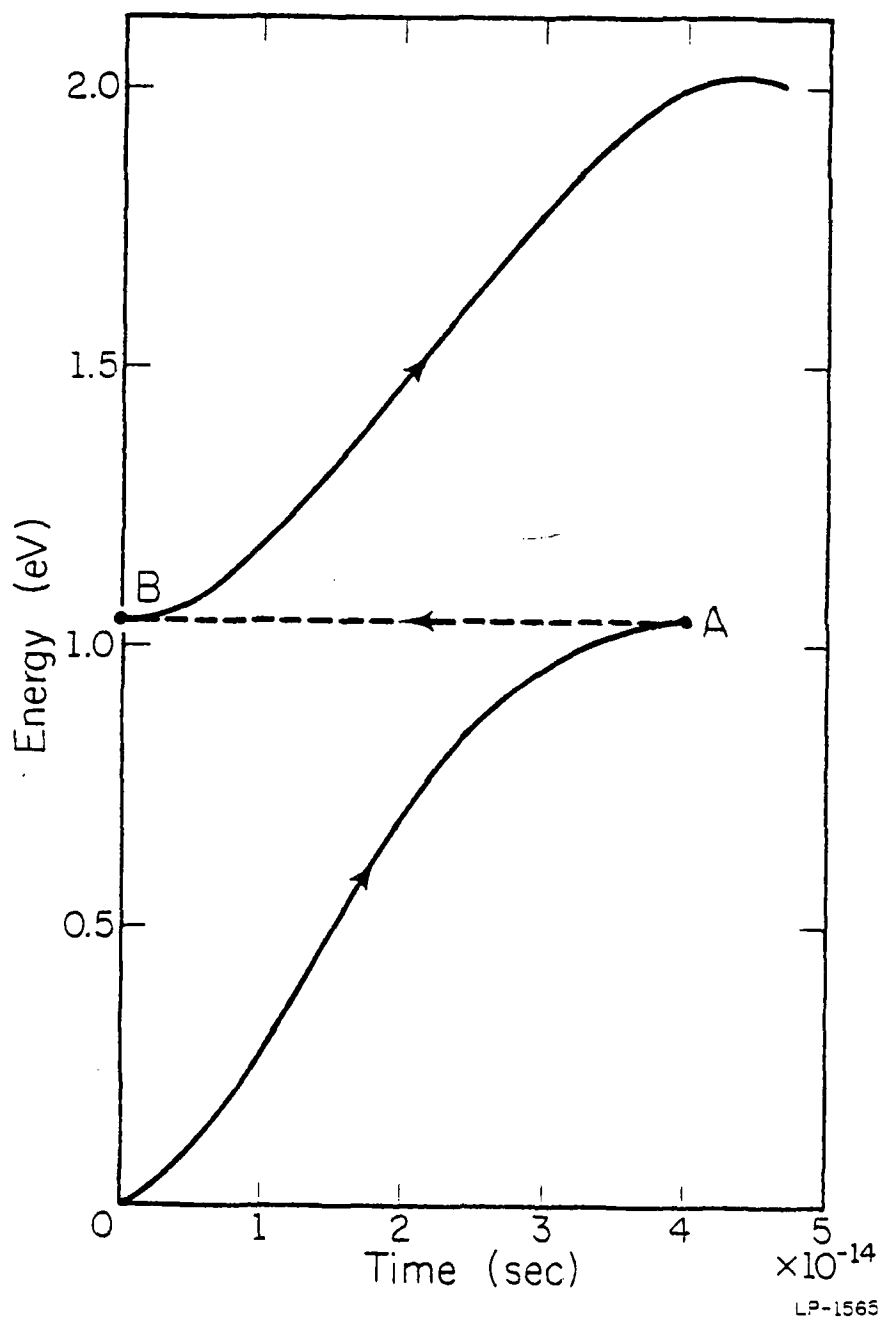


Fig. 3.12. Variation with time of electron energy for the process shown in Fig. 3.11.

### 3.6 Simulation Method

The Monte Carlo simulation keeps track of an electron  $k$ -vector in the Brillouin zone until it reaches the threshold energy for impact ionization. This is done with a knowledge of scattering mechanisms, scattering rates, and band structure in the whole Brillouin zone. The  $E(\vec{k})$  relation for an arbitrary  $k$ -point can be calculated in the following way. First, the  $k$ -point is mapped into the sampling region (Fig. 3.3) by symmetry operations which consist of taking absolute signs and the permutation of wave vector components. The energy is then calculated by quadratic interpolation utilizing the energies and the gradients of the surrounding 8 mesh points. The gradient is interpolated only linearly. Applying the inverse operations on the calculated energy and gradient gives the  $E(\vec{k})$  relation and the gradient at the original  $k$ -point.

Next we need to know the phonon scattering rate. Ideally the scattering rate should be calculated at each  $k$ -point in order to take into account the overlap integral[95] (see Eq. (A1.7) in Append. 1). Also, when the initial or final electron state is not on the symmetry points, the selection rules[96] become less restrictive and may give rise to additional scattering mechanisms. Moreover, even near the bottom of the valleys, it is known that the scattering rates are different in the  $\Gamma$ , L, and X valleys. In spite of these facts, we have assumed the scattering rate to be isotropic (only energy-dependent) for simplicity and because of lack of additional information. We have taken the scattering rate as given for the central valley. This overestimates the scattering rate when the electron is in the satellite valleys. The simplification is partly justified by the fact that the scattering rate of different valleys approach each other at

higher energies. Furthermore, since scattering to upper bands is possible in reality (which increases the scattering rate in the satellite valleys), the overestimation is at least partly compensated.

The values of the parameters for the calculation of the scattering rate are the same as the ones used in the simulation of the real space transfer mechanism, which are known to give a good fit to experimental data of the Gunn effect[34]. Below 0.33 eV only polar optical scattering occurs in the central valley. Above 0.33 eV polar optical scattering occurs only when an electron is in the central valley defined arbitrarily as

$$-0.3 \leq k_x, k_y, k_z \leq 0.3, \quad (3.10)$$

where the components are in units of  $2\pi/a$ . Otherwise intervalley scattering occurs. It is not appropriate to simply extend the scattering rate to higher energies because of the complicated band structure. Because the intervalley scattering rate is proportional to the density of final states, and the density of states in the conduction band decreases nearly quadratically above 1.5 eV[97], we have assumed a quadratically decreasing scattering rate above 1.5 eV. The resultant total scattering rate as a function of electron energy is shown in Fig. 3.13 (solid line). The maximum scattering rate is  $4.5 \times 10^{14} \text{ sec}^{-1}$  at 1.5 eV.

In the  $\langle 100 \rangle$  direction the threshold state for electron initiated ionization lies in the second conduction band[38]. An electron can tunnel through the "pseudo-gap" ( $\sim 0.2 \text{ eV}$ ) between the lowest and the second conduction band to reach threshold. No attempt has been made to simulate this tunneling mechanism. Since the tunneling time is estimated to be on the order of  $1 \times 10^{-13} \text{ sec}$ [38,98], and the intervalley scattering time for

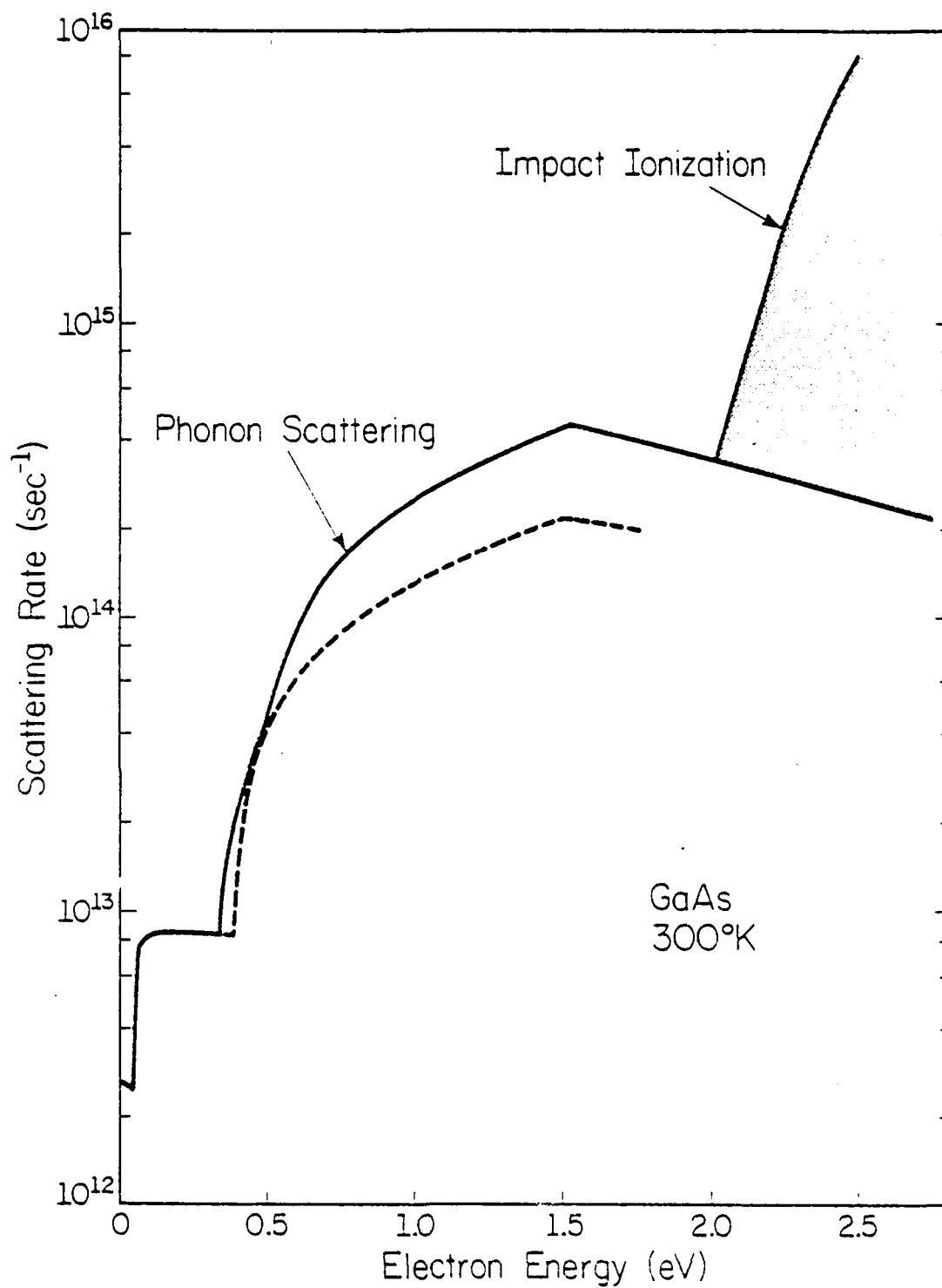


Fig. 3.13. The phonon scattering rate and the impact ionization probability in GaAs as a function of electron energy. The parameters are due to Littlejohn et al (solid line) [34] and Vison et al (broken line) [103].



an electron energy of 2.0 eV is much shorter ( $< 1 \times 10^{-14}$  sec) than this tunneling time, electrons are more likely to be scattered before they can tunnel to the upper band. Therefore, the contribution of these tunneling electrons to impact ionization is expected to be small.

The final state of the scattering process is determined in the following way. Since polar optical scattering is dominant only at low energies in the central valley, the usual formula (see Append. 1) with effective mass and non-parabolicity terms is used to choose a candidate for the final k-point. The energy at this k-point is then recalculated using the exact band structure to check if it is within an allowed range (typically 30 meV) around the final energy (for example,  $E + \hbar\omega_0$  in the case of phonon absorption). If it is outside this range, a different final state is chosen and the process is repeated until a proper state within the correct energy range is found. Intervalley scattering is known to be completely randomizing[26]. For this mechanism, once the final energy is calculated, those mesh points whose energies are within the allowed range are tabulated. One of them is then randomly selected as the final state.

Our treatment of phonon scattering processes represents a compromise between accuracy and numerical tractability. For a finite number of mesh points, the energy separation between any two k-points is finite. For example, for our 156 mesh points this energy separation can be as large as 60 meV. The allowed energy range during the scattering must be large enough to bridge this gap in order to assure the continuity of the energy band. In the limit of infinitely fine mesh points, the allowed range for final energy can be infinitely small. The number of k-points in this energy range for a given final energy is proportional to the density of

states at each region of  $k$  space with this final energy. Therefore, the procedure is basically correct, since the scattering rate for deformation potential scattering is proportional to the final density of states.

The impact ionizing collision is treated as an additional scattering mechanism. We assume an isotropic threshold energy of 2.0 eV. Anderson and Crowell[30] have shown that the threshold energy actually depends on the  $k$ -vector. However, their graphical procedure is almost impossible to perform in three-dimensional momentum space. A more systematic approach may be possible[99]. If the threshold energy is calculated for each  $k$ -point, it can be easily included in this simulation procedure. The impact ionization probability can be calculated from the matrix element for the screened Coulomb interaction[34,100,101]. However, here we use a simpler model demonstrated by Keldysh[77,102] and used by others[79]. According to Keldysh the probability of impact ionization can be represented as

$$\frac{1}{\tau_i(E)} = \frac{1}{\tau(E_i)} P \left[ \frac{E - E_i}{E_i} \right]^2 \quad (3.11)$$

where  $E$  is the electron energy,  $E_i$  is the threshold energy,  $1/\tau(E_i)$  is the scattering rate at  $E = E_i$ , and  $P$  is a dimensionless constant which is usually much larger than unity. This formula is valid for semiconductors with large dielectric constants. We take  $P$  as a parameter.  $P = 50 \sim \infty$  has been used by Chwang et al.[79]. As shown by Baraff[76], and then by Chwang[79] the impact ionization rate does not strongly depend on this parameter as long as  $P$  is large compared with unity. The energy dependence of impact ionization probability for  $P = 400$  is illustrated in Fig. 3.13.

Once the scattering rate and the ionization probability are determined, the rest of the simulation procedure is similar to the one described for the real space transfer mechanism, except that instead of determining the drift time by the integral (Eq. (2.14)), the scattering probability ( $\Delta t/\tau(E)$ ) is calculated at each time interval,  $\Delta t$ , and compared with a random number. This is necessary because of the complicated  $E(\vec{k})$  relation.  $\Delta t$  is taken to be approximately 1/10 th the average drift time. The simulation starts by releasing an electron with zero energy at the bottom of the central valley. The energy and the  $k$  vector of the electron are traced. When impact ionization occurs, the energy is reinitialized to zero to start a new history. This is justified by the fact that the resultant electron after ionization lies very close to the bottom of the central valley[30]. The impact ionization rate can be obtained by averaging each distance that an electron travels until impact ionization occurs over a sufficient number of ionizations. The distance,  $\Delta x$ , traveled during each drift is calculated either by accumulating a differential distance,  $v\Delta t$ , or by utilizing the relation

$$\Delta E = eF\Delta x, \quad (3.12)$$

where  $\Delta E$  is the energy gained during the drift. The velocity  $v$  is calculated from the gradient of  $E(\vec{k})$  relation.

### 3.7 Results

#### 3.7.1 Contribution of ballistic electrons

By terminating the simulation after the first scattering the electron suffers, the behavior of ballistic electrons can be studied. Additionally, we can determine the extent which these ballistic electrons contribute to

impact ionization. Since there is no electron initiated threshold state in the  $\langle 100 \rangle$  or the  $\langle 111 \rangle$  direction[89], we only consider the  $\langle 110 \rangle$  direction. We have also changed the threshold energy to 1.7 eV, which is the correct threshold energy in this direction[80]. Typically 100,000 trials have been done for each electric field.

The result of the calculation shows that an electron travels on the average approximately 200 Å, for an average time of  $3 \times 10^{-14}$  sec before the first scattering event. These numbers differ slightly for different orientations. By counting those electrons which cause impact ionization instead of scattering, we can estimate the contribution of ballistic electrons to the impact ionization rate. If the same scattering rate is used as shown in Fig. 3.13 (known to give a good fit to the Gunn effect[34]), we find no electrons (less than 0.001 %) causing impact ionization. There may be some uncertainties in the scattering rate, particularly in the values for the effective masses or the deformation potential constants. To find the maximum possible contribution of ballistic electrons to impact ionization, a smaller scattering rate has been tried. We have used the values given by Vinson et al.[103]:  $E_{\Gamma-X} = 0.4$  eV;  $E_{\Gamma-L} = 0.38$  eV;  $D_{\Gamma-X} = 1.1 \times 10^9$  eV/cm; and  $D_{\Gamma-L} = 2.8 \times 10^8$  eV/cm. This gives the scattering rate shown by the broken line in Fig. 3.13. This rate is approximately half of the previous value. Using this scattering rate in our calculation we obtain the results shown in Fig. 3.14. This figure shows the probability that an electron causes impact ionization prior to its scattering by a phonon as a function of electric field. As can be seen, even at the maximum (500 kV/cm for  $P = \infty$ ), only 0.2 % of the electrons causing impact ionization are "ballistic". Therefore we conclude that the contribution of ballistic electrons to impact ionization is

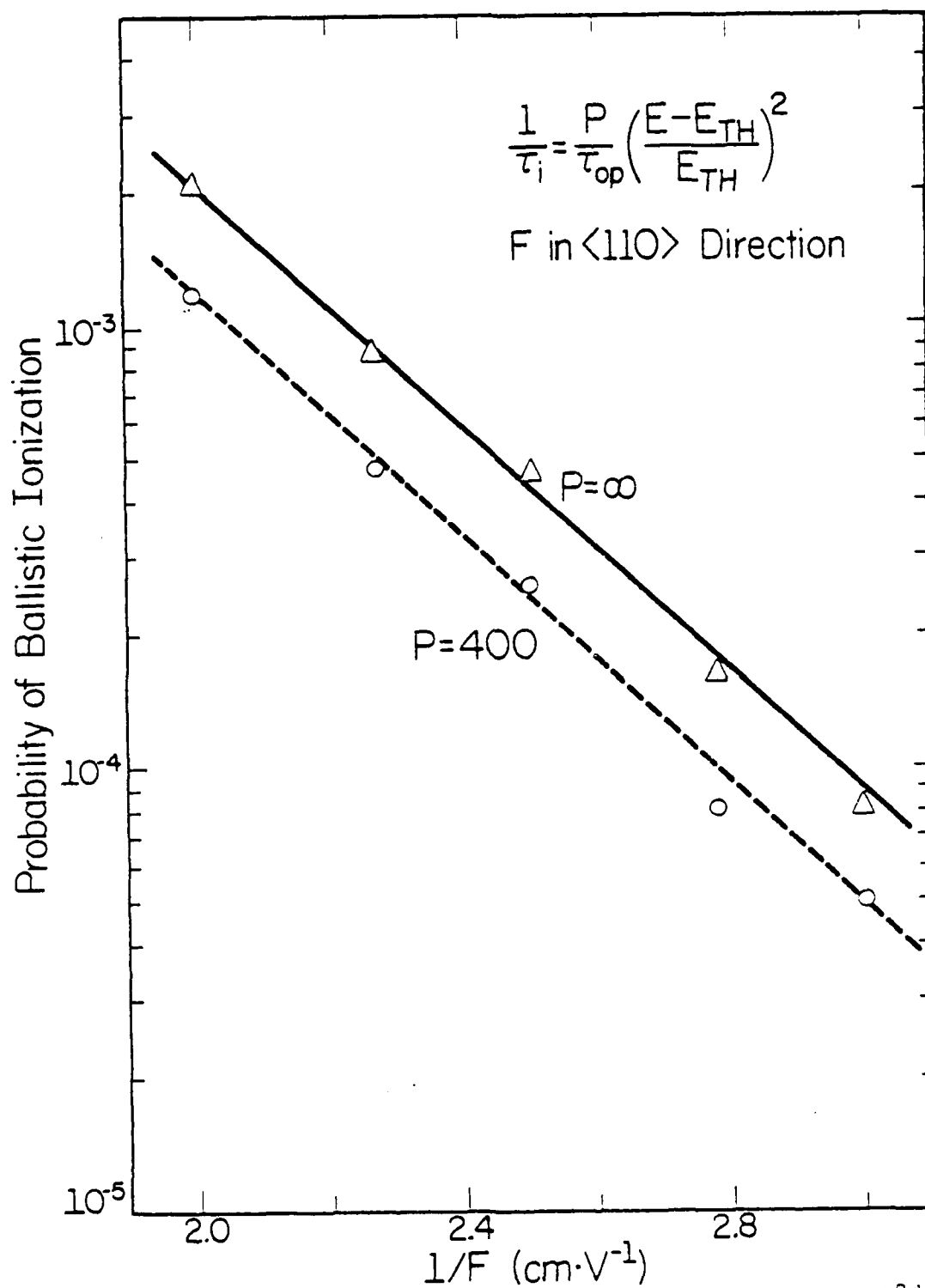


Fig. 3.14. Probability of ballistic electron causing impact ionization as a function of a reciprocal electric field.

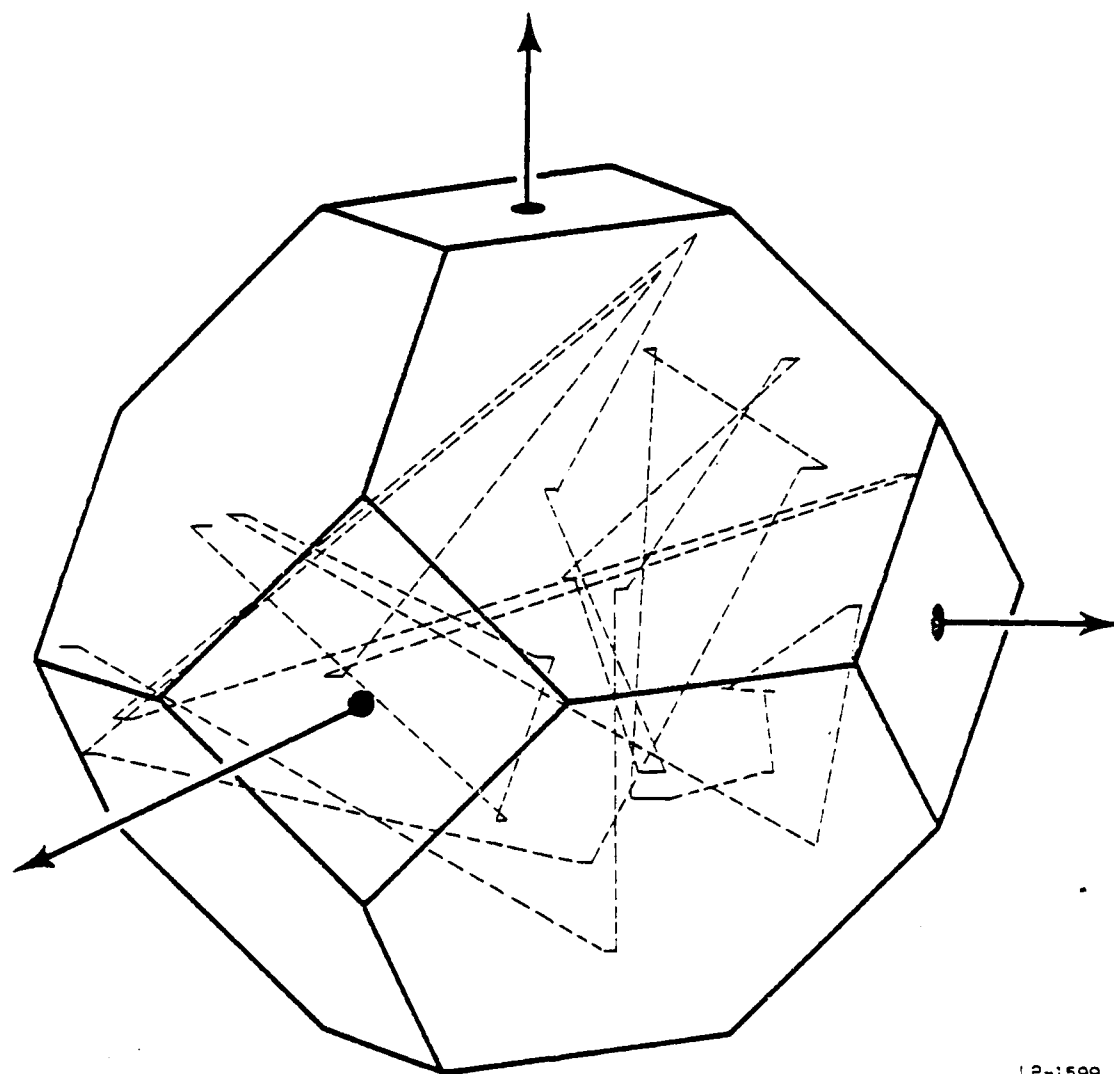
LP-1714

negligibly small if our present understanding of the scattering rate is correct. This conclusion negates the considerations by Capasso et al.[91] who suggested that ballistic electrons give a non-negligible contribution to the total ionization rate.

These "ballistic" electrons were discussed by Shockley who called them "lucky" electrons[75]. We have shown that Shockley's theory gives ionization rate that are too small. It is interesting to note, however, that the two curves in Fig. 3.14 show the correct  $1/E$  dependence as in Shockley's theory inspite of the more complicated band structure and scattering rate that we used.

### 3.7.2 Transport properties and ionization rate

In the calculation of the impact ionization rate a typical simulation consists of approximately 200,000 to 400,000 scattering events. Depending on electric field this would give 40 - 300 impact ionization events. Fig. 3.15 shows a typical trajectory of the  $k$  vector in the Brillouin zone for an electric field of 500 kV/cm in the  $\langle 100 \rangle$  direction. The solid lines represent the drift of the electron, and the broken lines represent the scatterings from one end to the next. When the  $k$  vector lies outside of the Brillouin zone, it is placed back inside the zone to the equivalent point. This is done by adding the appropriate reciprocal lattice vector to the original  $k$  vector. As seen from the figure the drift time is very short because of the high scattering rate at higher energies. The electron is frequently scattered over practically the entire Brillouin zone.



LP-1599

Fig. 3.15. Typical trajectory of the electron  $k$  vector in the Brillouin zone for an electric field of 500 kV/cm. The solid lines represent the drift and the broken lines represent the scatterings from one point to the next.

Fig. 3.16 shows how the calculated drift velocity converges as the number of scatterings is increased. Following some initial fluctuations, the velocity seems to "settle down" after approximately 2000 scatterings. Therefore, 200,000 scatterings should give a good estimate of the drift velocity. Similar curves are shown in Fig. 3.17 for the ionization rate. Because of the limited CPU time it has not been possible to take averages over more than 300 ionizations. However, the convergence is fairly good after 10 ionizations. From this figure the statistical fluctuation is estimated to be approximately 20 %. The problem of statistical fluctuation can be overcome by repeating the simulation only for the high energy tail[104]. This has not been attempted in this work.

Fig. 3.18 shows the average electron energy as a function of the electric field. The reason for the steeper increase beyond 100 kV/cm is not known, but may be related to the band structure. Fig. 3.19 shows the electron mean free path as a function of electric field. In the electric field range where impact ionization occurs, the mean free path changes from 50 Å to 30 Å. This is in good agreement with the experimental data[9,105] and the conventional Monte Carlo calculation[31]. The reason that our calculation agrees in this respect with the conventional method which does not include a realistic band structure is that the mean free path is mainly determined by the average electron energy, which is still small enough ( $\sim 0.8$  eV) for effective mass and non-parabolicity corrections to be sufficient.

The calculated electric field dependence of the electron drift velocity is shown in Fig. 3.20. The broken curve represents the experimental data by Ruch and Kino[106] at low electric field ( $< 11$  kV/cm),



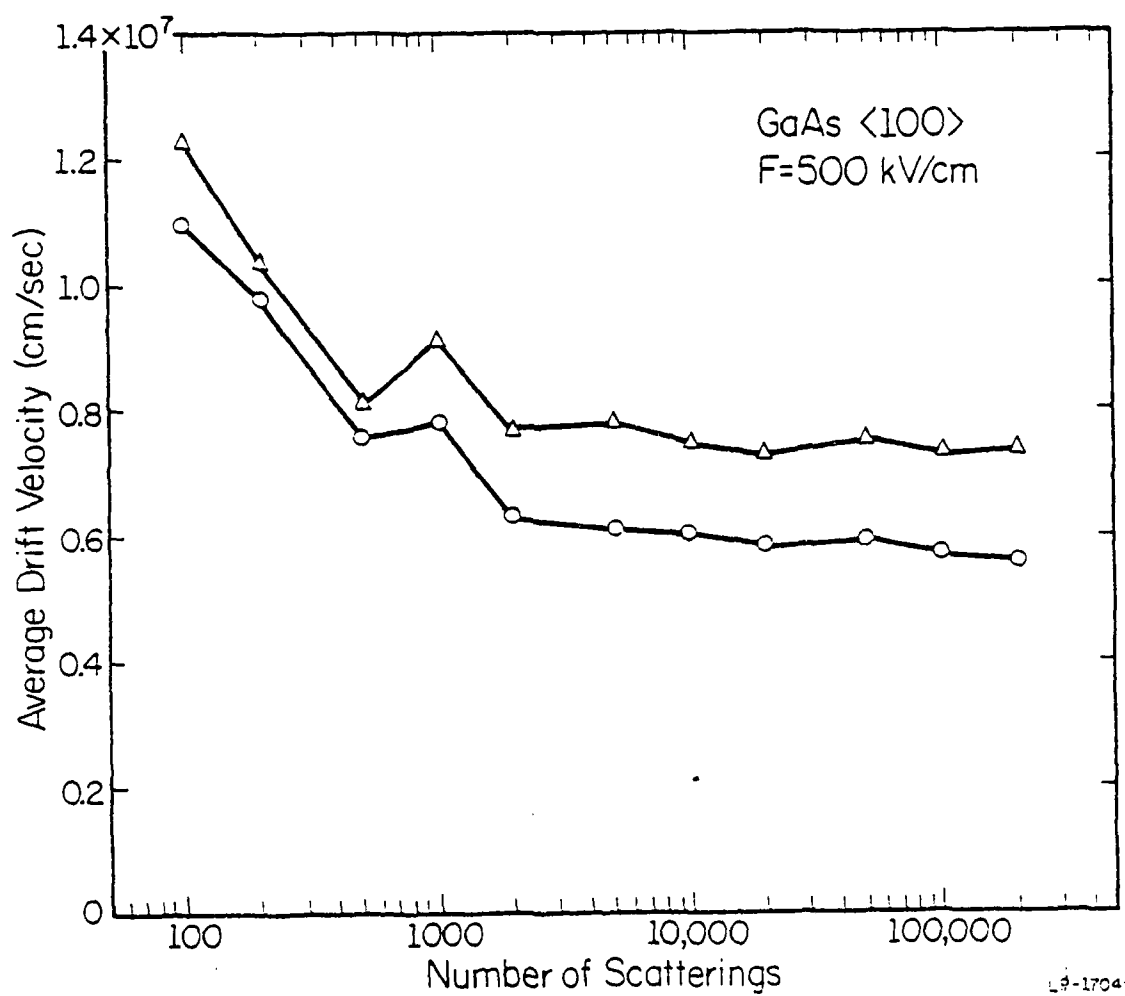


Fig. 3.16. Electron drift velocity in GaAs as a function of the number of scattering events obtained with a Monte Carlo simulation. The velocity is calculated from the slope of the  $E(k)$  curve ( $\Delta$ ) or from Eq. (3.12) (o).

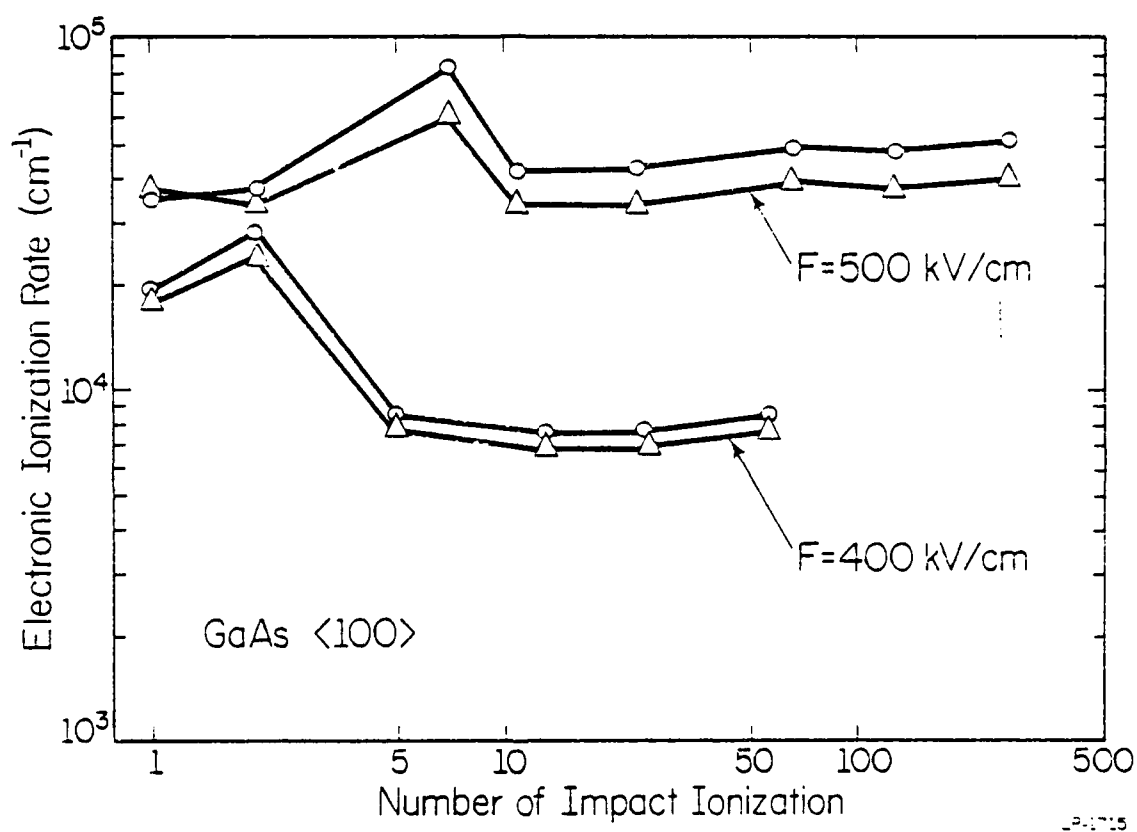


Fig. 3.17. Impact ionization rate in GaAs as a function of the number of ionizations obtained with a Monte Carlo simulation. The calculation is from the slope of the  $E(\vec{k})$  curve ( $\Delta$ ) or from Eq. (3.12) (o).

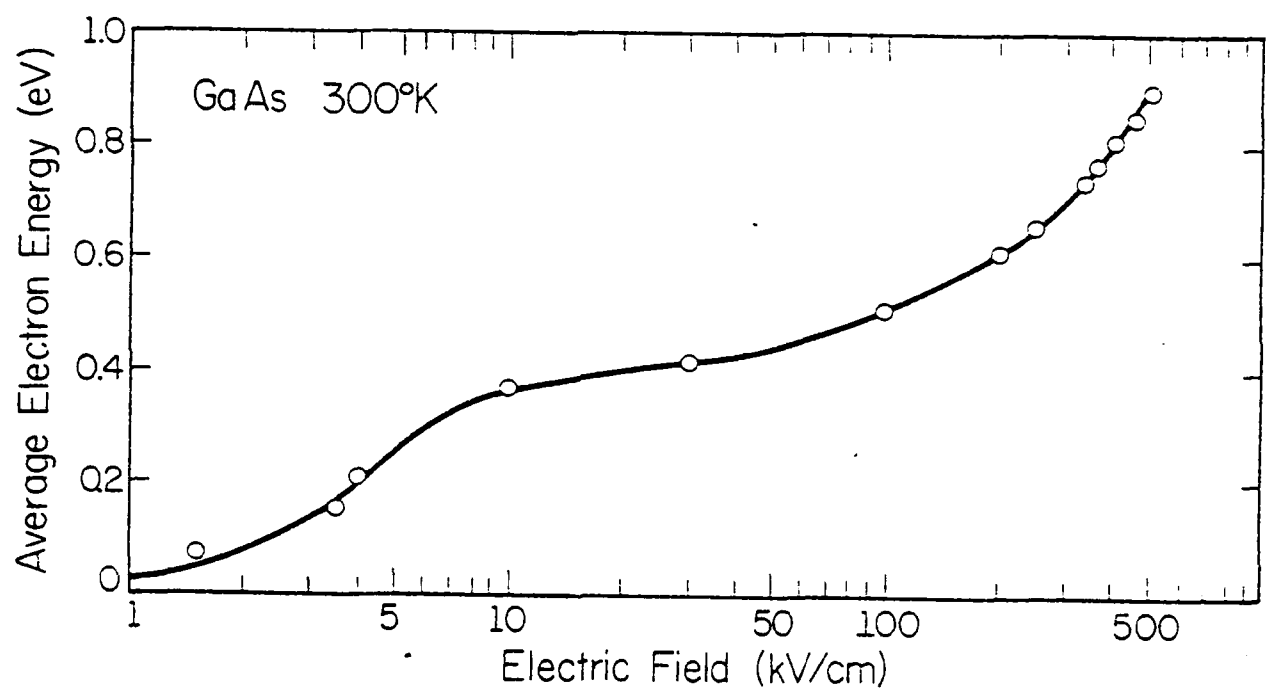
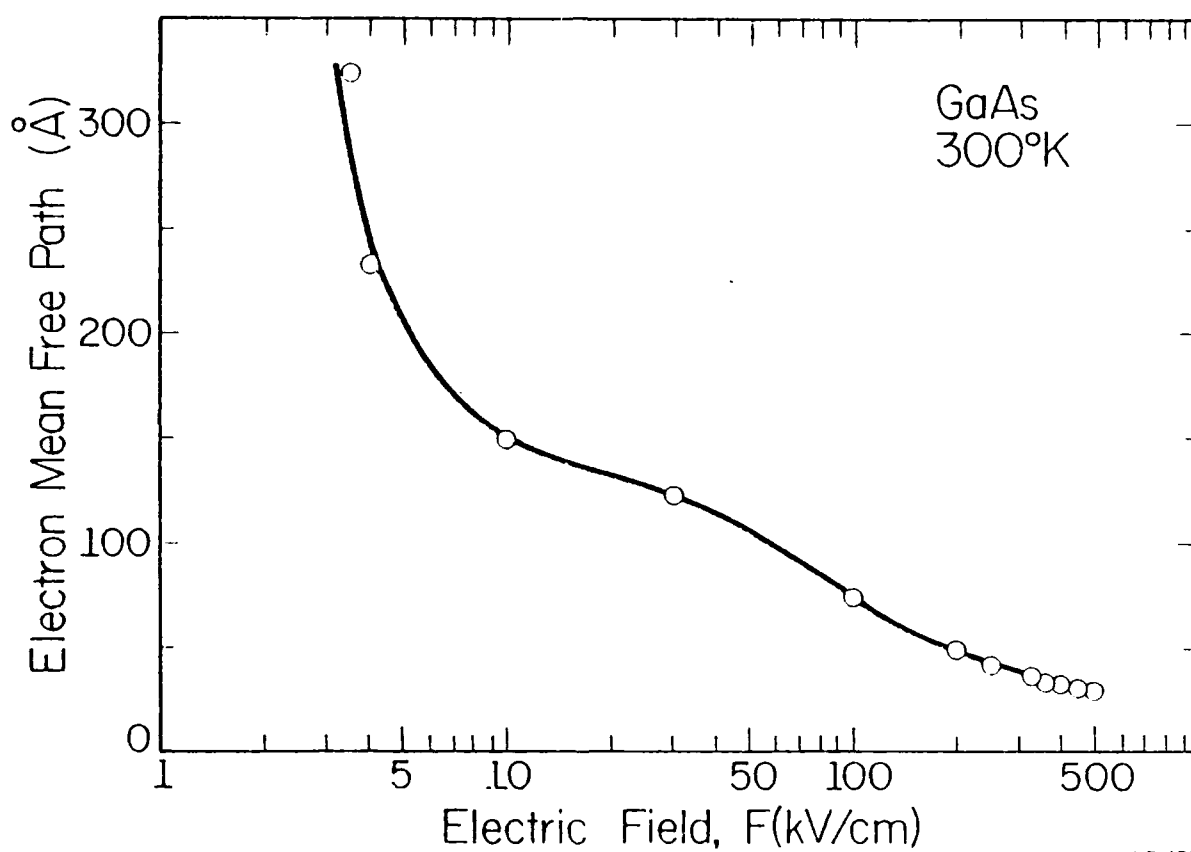
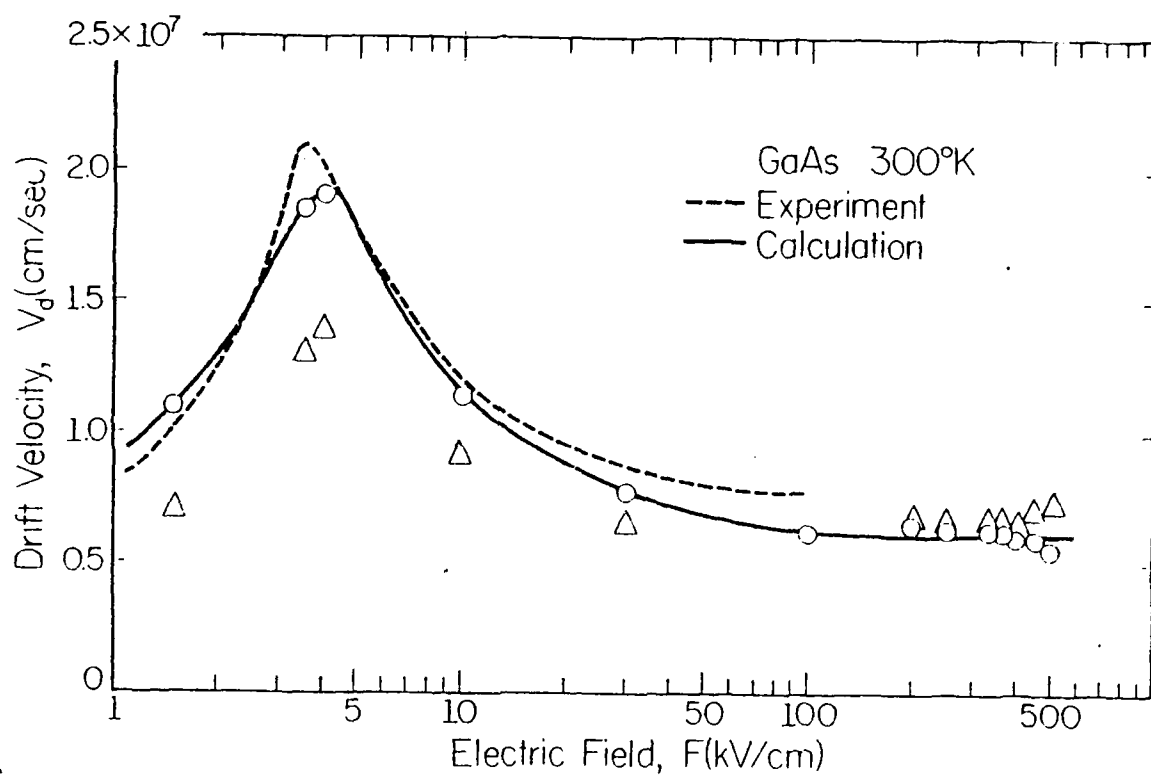


Fig. 3.18. Average electron energy in GaAs as a function of electric field calculated by a Monte Carlo simulation.



10 1717

Fig. 3.19. Electron mean free path in GaAs as a function of electric field calculated by a Monte Carlo simulation.



IP-171A

Fig. 3.20. Calculated electron drift velocity in GaAs at room temperature compared with the experimental data [100,107]. The calculated values are from the slope of the  $E(k)$  curve ( $\Delta$ ) or from Eq. (3.12) ( $o$ ).

and by Houston and Evans[107] at high field (20 ~ 100 kV/cm). The agreement is good over the entire range of electric fields experimentally investigated. The result using Eq. (3.11) gives much better fit than the result using the slopes of the  $E(\vec{k})$  relation. It is suspected that the accumulation of numerical errors in the slope calculation is responsible for the discrepancy. The slight deviations between theory and experiment at higher fields are believed to be mainly due to the pseudopotential band structure which gives the satellite valley effective masses larger than are usually measured. In Fig. 3.20 it can also be seen that the calculations describe quantitatively the Gunn effect. This means that the method can simulate polar optical scattering as well as intervalley scattering, and that the transition from polar optical scattering (low energy region) to intervalley scattering (high energy region) is accomplished smoothly.

Fig. 3.21 shows the calculated electric field dependence of the impact ionization rate in GaAs for three different crystal orientations. We have assumed  $P = 400$ . The shaded region indicates the range covered by the experimental data (Section 3.2). The agreement is fair, considering the uncertainty in the scattering rate at higher energies. The inclusion of upper bands is expected to increase the calculated ionization rate slightly, and therefore to improve the fit to the experimental data. Note, however, that the calculation shows within statistical fluctuations (~ 20 %) no orientation dependence for the ionization rate. This contradicts the experimental data by Pearsall et al.[39](Fig. 3.2). Another way to calculate the orientation dependence is by rotating the electric field direction from one axis to another. The result is shown in Fig. 3.22 for an electric field of 400 kV/cm when the field is rotated from the  $\langle 110 \rangle$  to

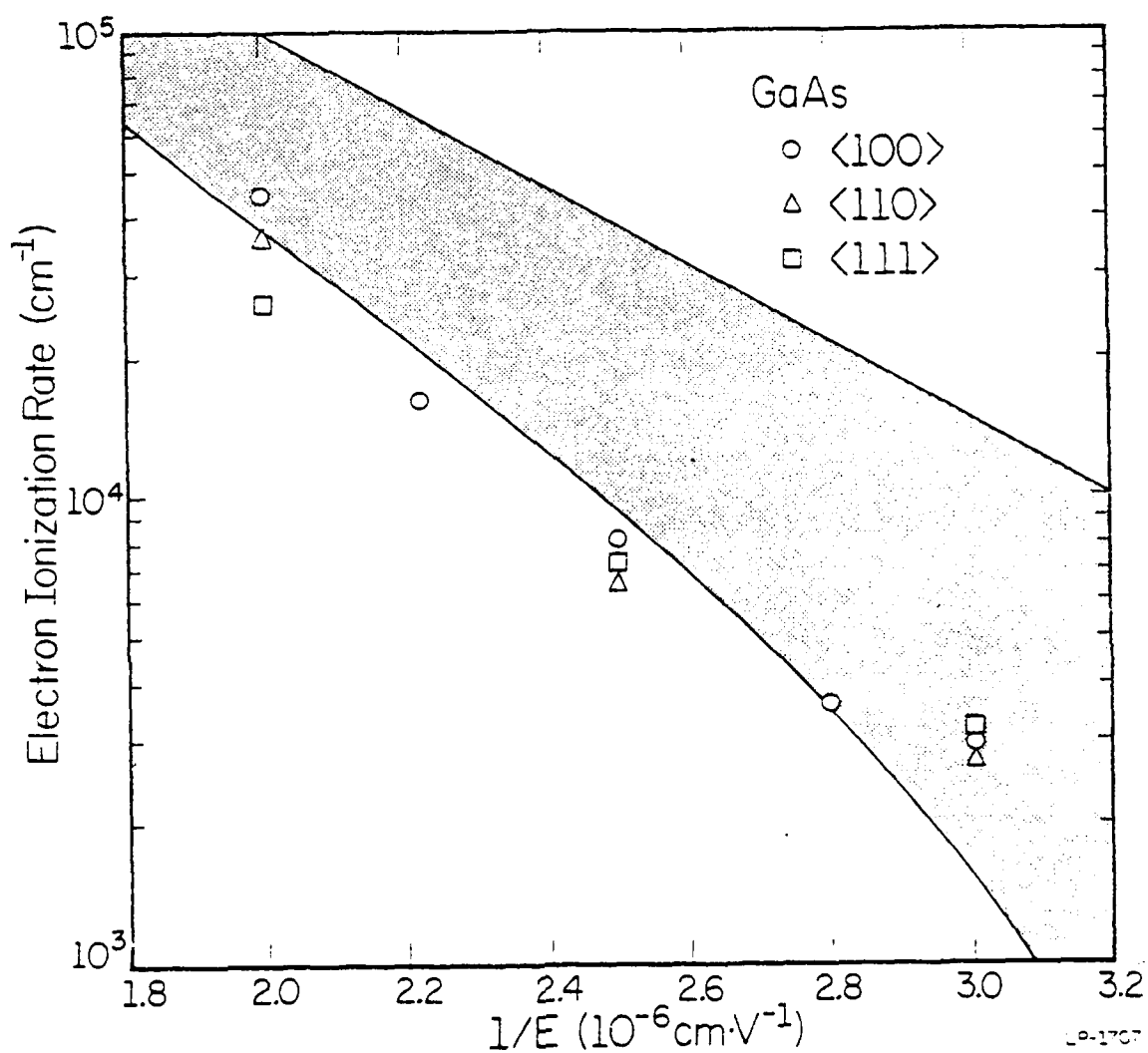


Fig. 3.21. Calculated impact ionization rate of an electron in GaAs with an electric field in three crystallographic directions as a function of a reciprocal field. The shaded region indicates the range of available experimental data (Fig. 3.1). Within statistical error, we do not see any orientation dependence.

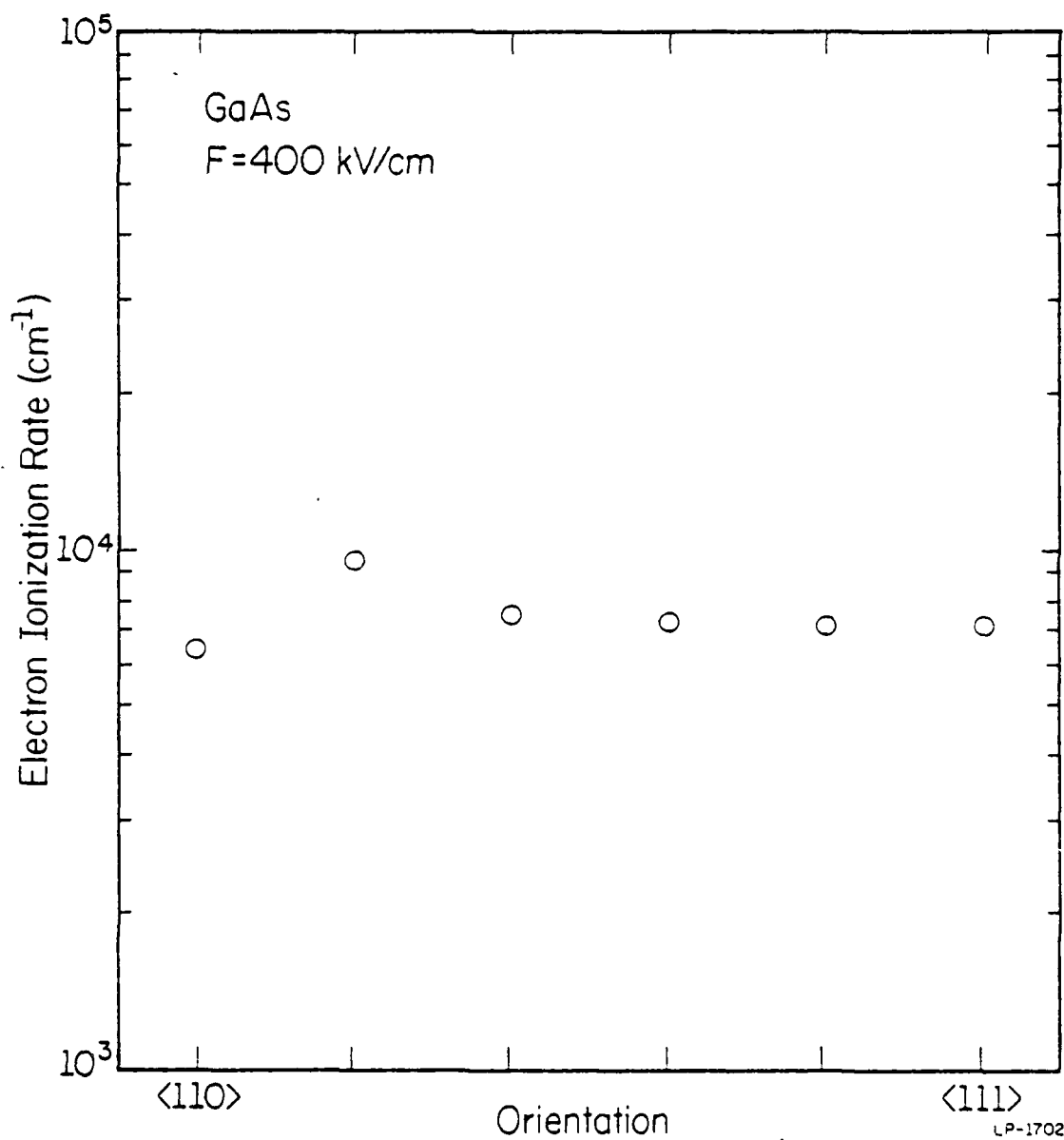


Fig. 3.22. Calculated impact ionization rate of an electron with an electric field of 400 kV/cm in several directions between the  $\langle 110 \rangle$  and  $\langle 111 \rangle$  directions.



$\langle 111 \rangle$  direction. Again we do not see any orientation dependence within the statistical error. A solution including this rotation of the electric field can be obtained only by the Monte Carlo method.

The effect of changing the value of  $P$  has been also examined. The result is shown in Fig. 3.23 for the case of  $P = 100, 400$ , and  $1600$  (the different definition from Chwang[79] has been used.  $P = 100$  in our case corresponds to  $P = 50$  in their paper). All the cases give practically the same impact ionization rate. This confirms the result by Baraff[76] and Chwang that the ionization rate is insensitive to the ionization probability as long as it is much larger than the probability of phonon scattering.

Due to the nature of the Monte Carlo principle, the calculation of the effective threshold energy[108] is trivial. The effective threshold energy is defined as the energy at which impact ionization actually takes place. It is usually slightly larger than the threshold energy because of the finite cross section for pair production. The result of this Monte Carlo simulation is shown in Fig. 3.24. The effective threshold energy is nearly independent of the electric field for large values of  $P$ , and a slightly increasing function of the field for smaller values of  $P$  in agreement with others[79,109]. This also agrees with the result[106] that on the average the impact ionization event takes place at  $0.6 \pm 0.2$  of  $qE\lambda_{op}$  above the threshold energy ( $\lambda_{op}$  is the mean free path for optical phonon scattering).

For a better understanding of how the electrons acquire the high energies, and how impact ionization is actually accomplished, we show in Figs. 3.25 and 3.26 the variation of electron energy after each scattering event for electric fields of  $500 \text{ kV/cm}$  and  $100 \text{ kV/cm}$  respectively. In the

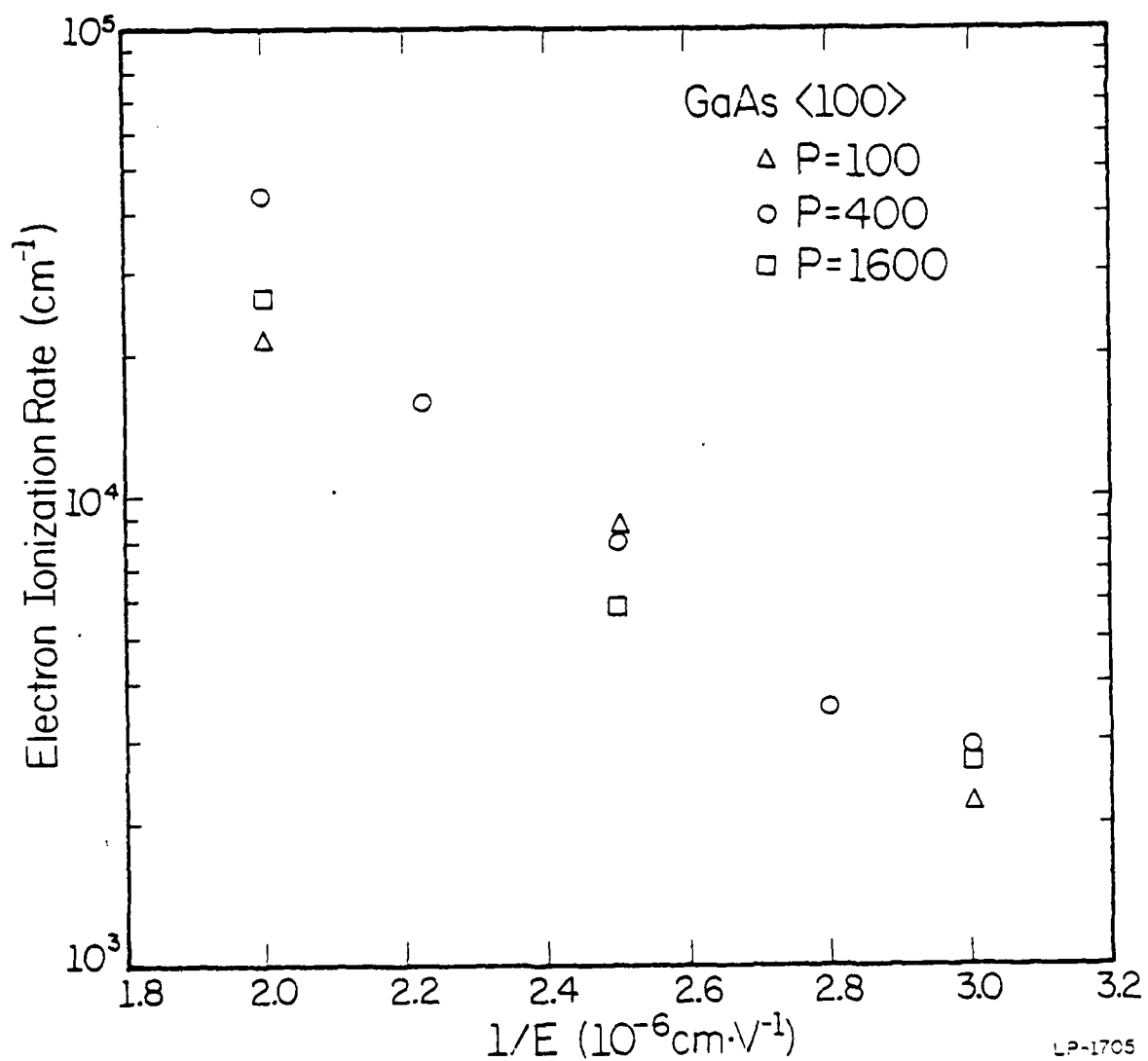


Fig. 3.23. Calculated impact ionization rate of an electron for several values of  $P$  (see Eq. (3.11)).

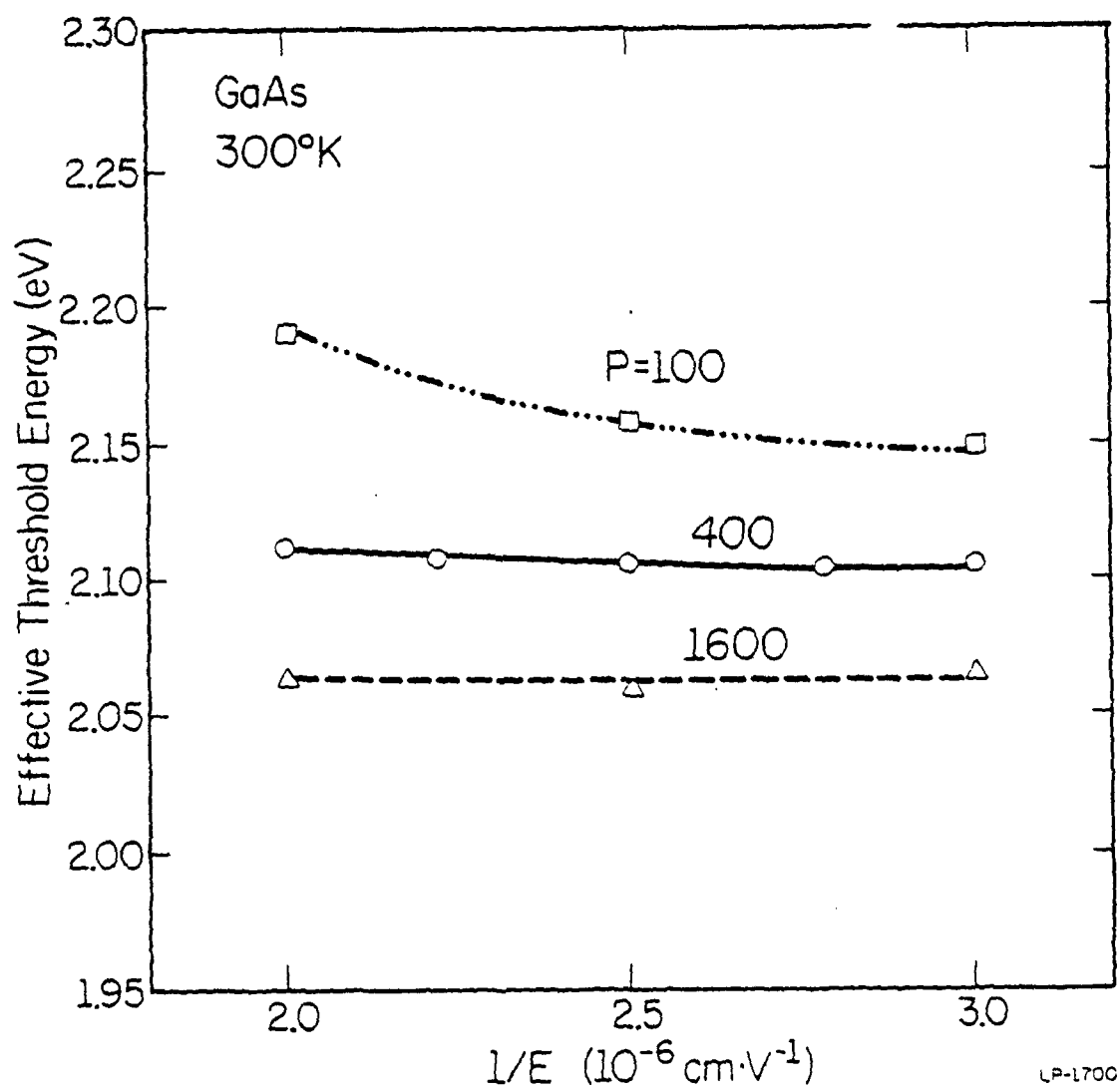


Fig. 3.24. Effective threshold energy as a function of a reciprocal electric field with  $P$  as a parameter.

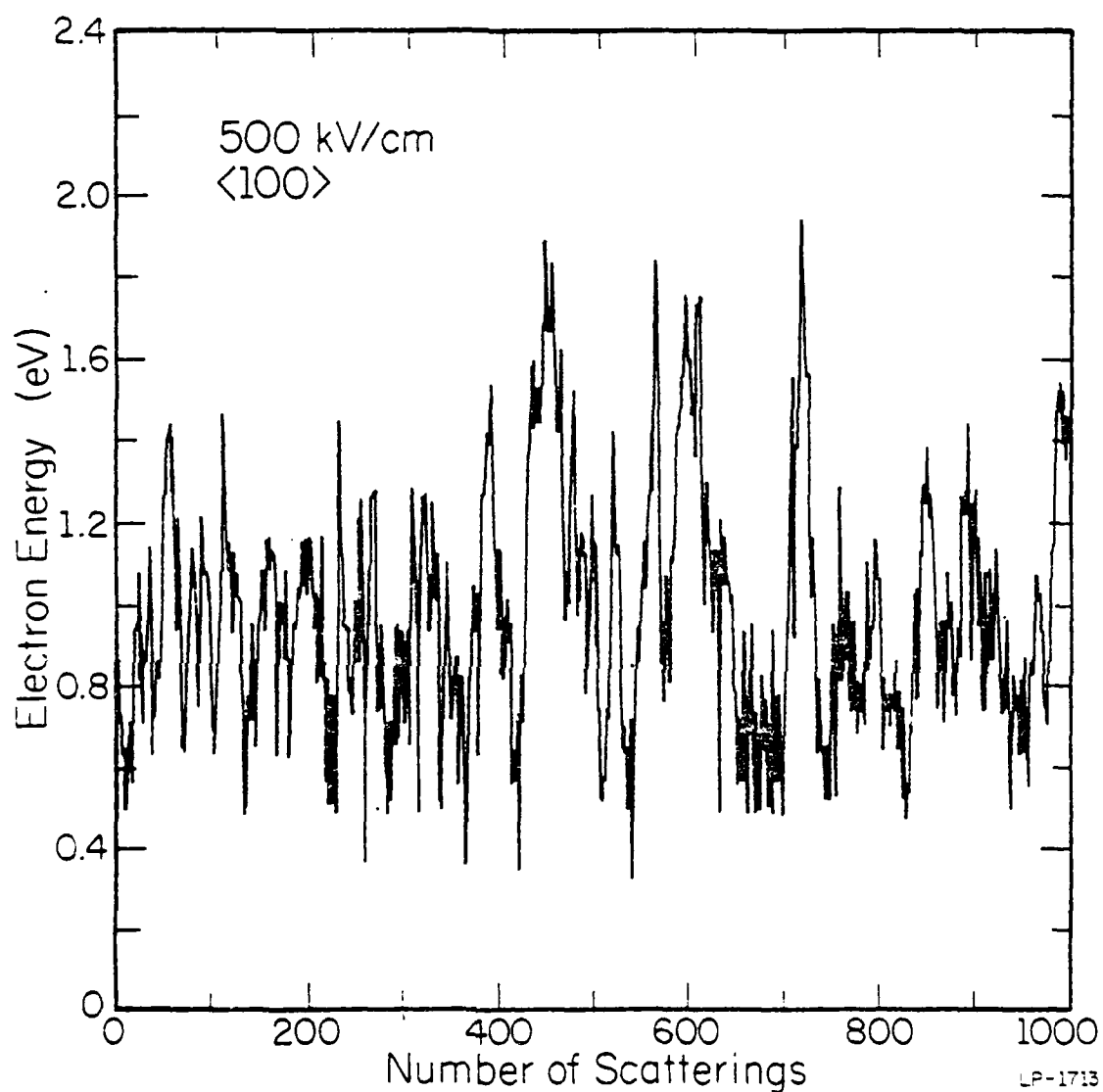


Fig. 3.25. Variation of electron energy after each scattering event for an electric field of 500 kV/cm obtained with a Monte Carlo simulation.

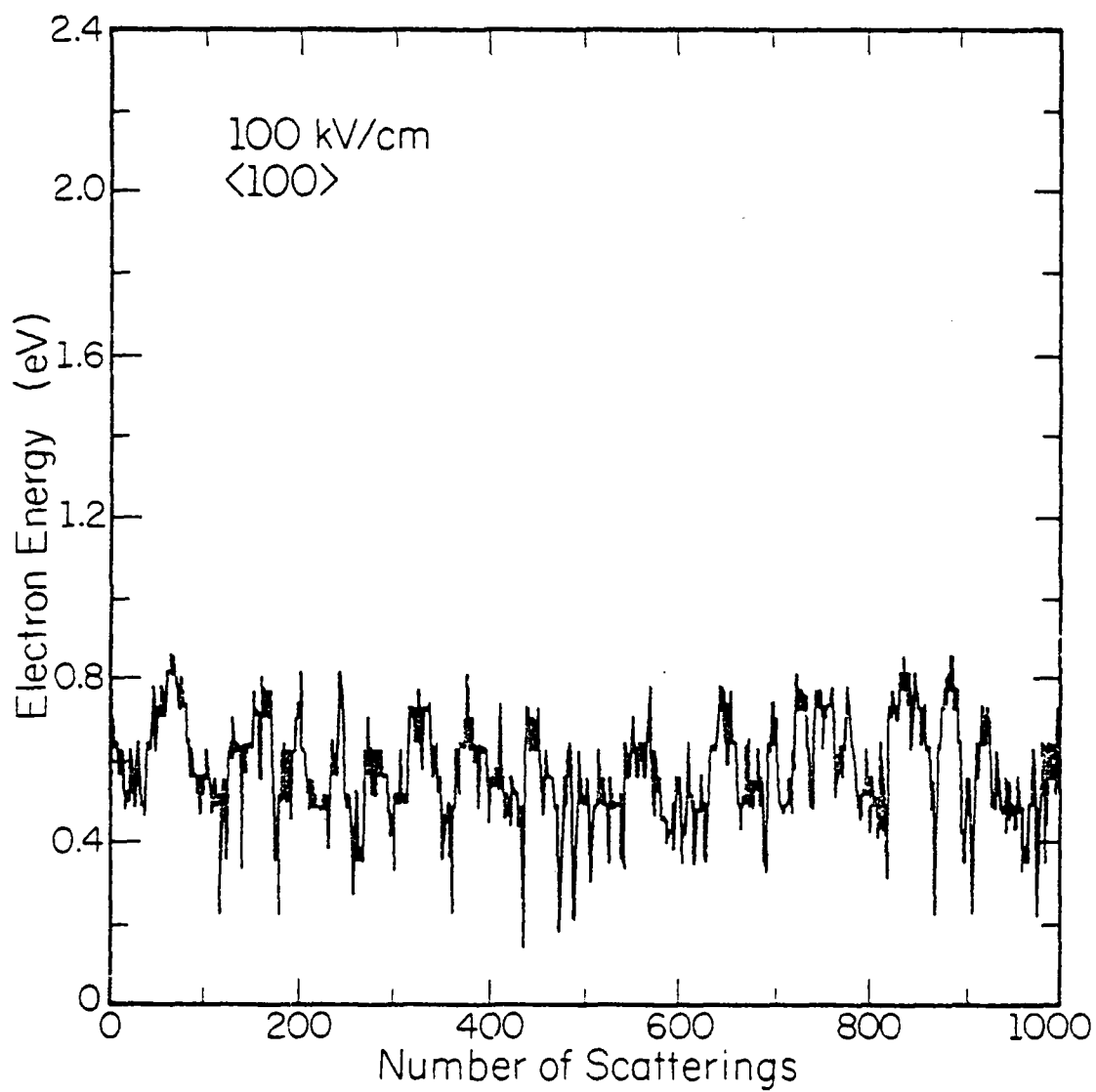


Fig. 3.26. Variation of electron energy after each scattering event for an electric field of 100 kV/cm.

case of 500 kV/cm, the electron energy stays around 0.7 ~ 1.2 eV most of the time, but the electron occasionally escapes phonon scattering and moves up to higher energies. In Fig. 3.25 we can see 4 ~ 5 spikes which reach to ~ 1.8 eV. When an electron reaches 2.0 eV, it causes impact ionization. We can think of these electrons as the "lucky electrons" in Shockley's theory, and those electrons around the average energy as the diffusing (in energy) electrons in Wolff's theory. However, as seen in the figure this classification is not very distinct. Even those electrons in the spikes suffer several scatterings before they reach the peak energies. Our results, therefore, contain Shockley's and Wolff's notions of ionizing electrons as does Baraff's theory, but under much more general conditions. Using Baraff's word[76], the notion of ballistic electrons by Shockley and diffusing electrons of Wolff are "complementary" in determining the impact ionization rate. This is due to the fact that the height of spikes (in Fig. 3.25) depends on the average energy of electrons. It is also important to note the difference between our ionizing electrons and Shockley's "lucky" electrons. Shockley's "lucky" electrons start from zero energy, escape the phonon scattering completely, and impact ionize. The ionizing electrons of our result start at the average energy and reach ionization threshold after a few scattering events. This explains why Shockley's theory badly underestimates the ionization rate. The actual cause of impact ionization is exactly what Shockley neglected, i.e., those electrons which suffer phonon scattering at intermediate energies and continue upwards in energy.

### 3.8 Summary

A Monte Carlo simulation of high field transport in GaAs employing a realistic band structure has been described. The method has been used to study the impact ionization mechanism in GaAs. The band structure of GaAs has been calculated using the empirical pseudopotential method. Partly due to the lack of information and partly for simplicity, we have made simplifying assumptions on the phonon scattering rates, the ionization threshold energy, and the ionization probability. This, however, is not an inherent limitation of the method. Unlike previous theories of impact ionization, the method requires, in principle, no adjustable parameters as long as the band structure and the scattering mechanism are known. The method has provided new results and increased the understanding of high field transport and impact ionization in GaAs. The calculated drift velocity, the mean free path, and the impact ionization rate are in fair agreement with the experimental data. The inclusion of the higher conduction bands is expected to further improve the fit. We do not expect, however, to obtain the anisotropy measured by Pearsall et al.[39]. In our opinion this anisotropy is not a consequence of the band structure, but is rather caused by crystal defects or other effects not well understood. It is found that the contribution of ballistic electrons to the impact ionization rate is negligibly small. Shockley's theory, therefore, badly underestimates the ionization rate. We have confirmed that the impact ionization rate is rather insensitive to the ionization probability above the threshold energy as long as the probability is much larger than the phonon scattering rate. The effective threshold energy has also been calculated and discussed briefly.

Based on the results of the simulation, a general discussion of impact ionization has been given. We find that typically electrons stay around an average energy and experience a large number of phonon scatterings. Occasionally electrons escape phonon scattering and move up to higher energy. Some reach ionization threshold after a few scattering events. This feature is seen in Fig. 3.25. It can be considered as a combination of Wolff's and Shockley's notion of ionizing electrons, but the distinction is rather vague. The reason for the success of Baraff's theory is that his theory also contains this feature. However, because of his formulation using distribution functions, the physical picture is not as clear as in our results. Moreover, our method includes realistic scattering mechanisms and band structure for the material considered.

Unlike previous theories of impact ionization, the present method can in principle be applied to any semiconductor. The method can be used for both polar and nonpolar materials. This is obvious from the successful simulation of the Gunn effect, which contains the transition from polar optical scattering to intervalley scattering. The calculation of hole initiated ionization rates should also be possible, although presently our understanding for hole transport is not as deep as for electron transport. This implies a tremendous importance for understanding the operation of photodetectors[3], since their performance depends on the ratio of electron and hole initiated ionization rates. It should be understood that the method is quite versatile in its application. A transient Monte Carlo method including the band structure may be used to investigate the orientation dependence of the avalanche response time[110]. The inclusion of the position dependence should enable us to study the effect of the "dark-space"[111].



There are some improvements which should be investigated in the future. First of all, the upper conduction bands, at least the second conduction band, should be included in the simulation. This can be done rather easily if we know (or calculate) the scattering rate between different bands. The inclusion of tunneling is also possible. Next, finer mesh points should be used in the calculation of the band structure to increase the numerical accuracy. Ideally the maximum energy separation between any two points should be much smaller than the phonon energy. Improvement on the scattering rates also seems important. The scattering rates should be assigned at each  $k$  point including the overlap integrals which are available from the band structure calculations.

#### 4. CONCLUSIONS

Two theoretical aspects of high field transport in III-V semiconductors have been studied. One occurs in real space (real-space electron transfer), while the other is related to momentum space (band structure). To understand and exploit high field transport, we have to examine it in both real and momentum spaces. Just as the band structure (inhomogeneity in momentum space) makes possible the transfer of electrons, inhomogeneities in real space (heterostructures) lead to interesting transport phenomena. As for our simulation of high field transport utilizing a realistic band structure, we feel this study is still in a preliminary stage. Our ultimate goal is to understand what an electron undergoes at each point in momentum space at high energies, including details of the scattering mechanisms.

I would like to close this thesis work by quoting a statement by E. M. Conwell[26] in 1967, "Our present knowledge of high-field transport in particular materials is limited to regions close to the band edges. In the near future we should be able to penetrate further into the bands, proceeding hand in hand with the detailed studies of band structure now becoming available, and perhaps even contributing to these studies. Such advances should make possible a more detailed understanding of avalanche and perhaps ultimately of the problem that first stimulated interest in these studies, dielectric breakdown." A step toward these goals has been made in this thesis work.

## REFERENCES

1. W. Shockley, "Hot electrons in germanium and ohm's law," Bell Syst. Tech. J., vol. 30, pp. 990-1034, 1951.
2. C. Hilsum, "Historical background of hot electron physics (A look over the shoulder)," Solid-State Electron., vol. 21, pp. 5-8, 1973.
3. B. K. Ridley, "Anatomy of the transferred-electron effect in III-V semiconductors," J. Appl. Phys., vol. 48, pp. 754-764, 1977.
4. L. Esaki and R. Tsu, "Superlattice and negative conductivity in semiconductors," IBM Research Report No. RC-2413, 1969.
5. K. Hess, H. Morkoc, H. Shichijo, and B. G. Streetman, "Negative differential resistance through real-space electron transfer," Appl. Phys. Lett., vol. 35, pp. 469-471, 1979.
6. K. Hess, private communication.  
(The possibility was discussed in 1967 by G. Tschulena, G. Nimtz, and K. Hess, but was not pursued, since an actual mechanism for the transfer in real space and heterojunction layers were unknown to them.)  
Pacha and Paschke also discussed the possibility of real space transfer in Electron. Comm. (AEU), vol. 32, pp. 235-238, 1978. However, their mechanism did not involve layered heterostructures.
7. R. Dingle, H. L. Störmer, A. C. Gossard, and W. Wiegmann, "Electron mobilities in modulation-doped semiconductor heterojunction superlattices," Appl. Phys. Lett., vol. 33, pp. 665-667, 1978.
8. G. E. Stillman and C. M. Wolfe, "Avalanche photodiodes," Semiconductors and Semimetals, (R. K. Willardson and A. C. Beers, eds.), vol. 12, Academic Press, New York, pp. 291-393, 1977.
9. S. M. Sze, Physics of Semiconductor Devices, John Wiley and Sons, New York, 1969.
10. K. Hess and C. T. Sah, "The ultimate limits of CCD performance imposed by hot electron effects," Solid-State Electron., vol. 22, pp. 1025-1033, 1979.
11. B. Hoeneisen and C. A. Mead, "Fundamental limitations in

- microelectronics — I. MOS technology," Solid-State Electron., vol. 15, pp. 819-829, 1972.
12. A. Y. Cho and J. R. Arthur, "Molecular beam epitaxy," Progress in Solid State Chemistry, edited by G. Somerjai and J. McCaldin (Pergamon, New York, 1975), vol. 10, pp. 157-191.
  13. A. Y. Cho, "Growth of periodic structure by the molecular-beam method," Appl. Phys. Lett., vol. 19, pp. 467-468, 1971.
  14. L. L. Chang, L. Esaki, W. E. Howard, and R. Ludeke, "The growth of a GaAs-GaAlAs superlattice," J. Vac. Sci. Technol., vol. 10, pp. 11-16, 1973.
  15. A. E. Blakeslee, "Vapor growth of a semiconductor superlattice," J. Electrochem. Soc., vol. 118, pp. 1459-1463, 1971.
  16. R. D. Dupuis, P. D. Dapkus, N. Holonyak, Jr., E. A. Rezek, and R. Chin, "Room-temperature laser operation of quantum-well  $\text{Ga}_{1-x}\text{Al}_x\text{As}$ -GaAs laser diodes grown by metalorganic chemical vapor deposition," Appl. Phys. Lett., vol. 32, pp. 295-297, 1978.
  17. J. M. Woodall, "Solution grown  $\text{Ga}_{1-x}\text{Al}_x\text{As}$  superlattice structures," J. Cryst. Growth, vol. 12, pp. 32-33, 1972.
  18. E. A. Rezek, N. Holonyak, Jr., B. A. Vojak, G. E. Stillman, J. A. Rossi, D. L. Keune, and J. D. Fairing, "LPE In  $\text{Ga}_x\text{P}_{1-x}\text{As}_z$  ( $x \sim 0.12$ ,  $z \sim 0.26$ ) DH laser with multiple thin-layer ( $\sim 500 \text{ \AA}$ ) active region," Appl. Phys. Lett., vol. 31, pp. 288-290, 1977.
  19. H. C. Casey, Jr. and M. B. Panish, Heterostructure Lasers, Part A, Academic, New York, 1978.
  20. R. Dingle, W. Wiegmann, and C. H. Henry, "Quantum states of confined carriers in very thin  $\text{Al Ga}_{1-x}\text{As}$ -GaAs- $\text{Al Ga}_{1-x}\text{As}$  heterostructures," Phys. Rev. Lett., vol. 33, pp. 327-330, 1974.
  21. H. L. Störmer, R. Dingle, A. C. Gossard, W. Wiegmann, and R. A. Logan, "Electronic properties of modulation-doped  $\text{GaAs-Al Ga}_{1-x}\text{As}$  superlattices," Physics of Semiconductor, 1973, Conference Series Number 43, edited by B. L. H. Wilson (The Institute of Physics, Bristol and London, 1973), pp. 557-560.

22. G. H. Döhler, "Doping superlattices," J. Vac. Sci. Technol., vol. 16, pp. 851-856, 1979.
23. K. Hess, "Impurity and phonon scattering in layered structures," Appl. Phys. Lett., vol. 35, pp. 484-486, 1979.
24. H. Shichijo, K. Hess, and B. G. Streetman, "Real-space electron transfer by thermionic emission in GaAs-Al<sub>x</sub>Ga<sub>1-x</sub>As heterostructures: Analytical model for large layer width," Solid-State Electron., vol. 23, pp. 817-822, 1980.
25. G. Salardi, B. Pellegrini, and T. DiLeo, "Generalization of thermionic emission theory. Temperature dependence of GaAs intervalley gap from measurements on Schottky diodes," Solid-State Electron., vol. 22, pp. 435-441, 1979.
26. E. M. Conwell, "High field transport in semiconductors," Solid State Physics (F. Seitz, D. Turnbull, and H. Ehrenreich, eds.), Suppl. 9, Academic, New York, 1967.
27. K. Seeger, Semiconductor Physics, Springer-Verlag, Berlin, 1973.
28. H. A. Bethe, "Theory of the boundary layer of crystal rectifiers," MIT Rad. Lab. Rep., vol. 43, 1942.
29. R. Stratton, "The influence of interelectronic collisions on conduction and breakdown in polar crystals," Proc. Roy. Soc., vol. 246A, pp. 406-422, 1953.
30. C. Hilsum, "Transferred electron amplifiers and oscillators," Proc. IRE, vol. 50, pp. 185-189, 1962.
31. B. K. Ridley and T. B. Watkins, "The possibility of negative resistance effects in semiconductors," Proc. Phys. Soc., vol. 78, pp. 293-304, 1961.
32. E. M. Conwell and M. O. Vassell, "High-field transport in n-type GaAs," Phys. Rev., vol. 166, pp. 727-821, 1968.
33. W. Fawcett, A. D. Boardman, and S. Swain, "Monte Carlo determination of electron transport properties in gallium arsenide," J. Phys. Chem. Solids, vol. 31, pp. 1963-1990, 1970.

34. M. A. Littlejohn, J. R. Hauser, and T. H. Glisson, "Velocity-field characteristics of GaAs with  $\Gamma_6^c$ - $L_6^c$ - $X_6^c$  conduction-band ordering," J. Appl. Phys., vol. 48, pp. 4587-4590, 1977.
35. J. G. Ruch and W. Fawcett, "Temperature dependence of the transport properties of gallium arsenide determined by a Monte Carlo method," J. Appl. Phys., vol. 41, pp. 3843-3849, 1970.
36. D. E. Aspnes, "GaAs lower conduction-band minima: Ordering and properties," Phys. Rev. B, vol. 14, pp. 5331-5343, 1976.
37. G. B. Stringfellow and H. Kunzel, "Electron mobility in compensated GaAs and  $\text{Al}_x\text{Ga}_{1-x}\text{As}$ ," J. Appl. Phys., vol. 51, pp. 3254-3261, 1980.
38. P. J. Price, "Monte Carlo calculation of electron transport in solids," Semiconductors and Semimetals (R. K. Willardson and A. C. Beers, eds.), vol. 14, Academic, New York, pp. 249-308, 1979.
39. T. H. Glisson, J. R. Hauser, and M. A. Littlejohn, private communication.
40. M. A. Littlejohn, J. R. Hauser, and T. H. Glisson, "Monte Carlo calculation of the velocity-field relationship for gallium nitride," Appl. Phys. Lett., vol. 26, pp. 625-627, 1975.
41. M. A. Littlejohn, J. R. Hauser, and T. H. Glisson, "Velocity-field characteristics of  $\text{Ga}_{1-x}\text{In}_x\text{P}_{1-y}\text{As}_y$  quaternary alloys," Appl. Phys. Lett., vol. 30, pp. 242-244, 1977.
42. R. Stratton, "Diffusion of hot and cold electrons in semiconductor barriers," Phys. Rev., vol. 126, pp. 2002-2014, 1962.
43. K. Hess, "Phenomenological physics of hot carriers in semiconductors," Physics of Nonlinear Transport in Semiconductors, (D. K. Ferry, J. R. Barker, and C. Jacoboni, eds.), Plenum, 1980.
44. R. Dingle, "Confined carrier quantum states in ultrathin semiconductor heterostructures," Festkörper-Probleme XV (Advances in Solid State Physics), pp. 21-43, Pergamon-Vieweg, 1975.
45. H. L. Störmer, R. Dingle, A. C. Gossard, W. Wiegmann, and M. D. Sturge, "Two-dimensional electron gas at differentially doped  $\text{GaAs-Al}_x\text{Ga}_{1-x}\text{As}$

- heterojunction interface," J. Vac. Sci. Technol., vol. 16, pp. 1517-1519, 1979.
46. D. C. Tsui and R. A. Logan, "Observation of two-dimensional electrons in LPE-grown GaAs-Al<sub>x</sub>Ga<sub>1-x</sub>As heterojunctions," Appl. Phys. Lett., vol. 35, pp. 99-101, 1979.
  47. F. Stern, "Quantum properties of surface space-charge layers," CRC Crit. Rev. Solid State Sci., vol. 4, pp. 499-514, 1974.
  48. D. K. Ferry, "Optical and intervalley scattering in quantized inversion layers in semiconductors," Surface Sci., vol. 57, pp. 213-228, 1976.
  49. K. Hess and C. T. Sah, "Hot carriers in silicon surface inversion layers," J. Appl. Phys., vol. 45, pp. 1254-1257, 1974.
  50. C. Kittel, Quantum Theory of Solids, John Wiley and Sons, 1963.
  51. Similar integration has been done in Chapter 6 of Ref. 16.
  52. N. Holonyak, Jr., R. M. Kolbas, W. D. Laidig, B. A. Vojak, K. Hess, R. D. Dupuis, and P. D. Dapkus, "Phonon-assisted recombination and stimulated emission in quantum-well Al<sub>x</sub>Ga<sub>1-x</sub>As-GaAs heterostructures," J. Appl. Phys., vol. 51, pp. 1328-1337, 1980.
  53. F. Stern, "Self-consistent results for n-type Si inversion layers," Phys. Rev. B, vol. 5, pp. 4891-4899, 1972.
  54. D. C. Tsui, H. L. Störmer, A. C. Gossard, and W. Wiegmann, "Two-dimensional electrical transport in GaAs-Al<sub>x</sub>Ga<sub>1-x</sub>As multilayers at high magnetic fields," Phys. Rev. B, vol. 21, pp. 1559-1595, 1980.
  55. J. S. Moore and P. Das, "The transient response of hot electrons in quasi-two-dimensional semiconductors," J. Appl. Phys., vol. 50, pp. 8082-8086, 1979.
  56. P. K. Basu, "High-field drift velocity of silicon inversion layers: A Monte Carlo calculation," J. Appl. Phys., vol. 48, pp. 350-353, 1977.
  57. L. I. Schiff, Quantum Mechanics, McGraw-Hill, 1955.
  58. A. Golilberg, H. M. Schey, and J. L. Schwartz, "Computer-generated motion

- pictures of one-dimensional quantum-mechanical transmission and reflection phenomena," Am. J. Phys., vol. 35, pp. 177-186, 1967.
59. C. M. Wu and E. S. Yang, "Carrier transport across heterojunction interfaces," Solid-State Electron., vol. 22, pp. 241-248, 1979.
  60. G. C. Osbourn and D. L. Smith, "Transmission and reflection coefficients of carriers at an abrupt GaAs-GaAlAs (100) interface," Phys. Rev. B, vol. 19, pp. 2124-2133, 1979.
  61. P. J. Price, "Transmission of Bloch waves through crystal interfaces," in Proceedings of the International Conference on the Physics of Semiconductors, Exeter, pp. 99-103, 1962, edited by A. C. Strickland, (The Institute of Physics and the Physical Society, London, 1962). I would like to thank Dr. Price (IBM) for a copy of this paper.
  62. C. M. Garner, C. Y. Su, and W. E. Spicer, "Interface studies of  $\text{Al Ga}_{1-x}\text{As-GaAs}$  heterojunctions," J. Vac. Sci. Technol., vol. 16, pp. 1521-1524, 1979.
  63. G. C. Osbourn and D. L. Smith, "Carrier transport coefficients across GaAs-GaAlAs (100) interfaces," J. Vac. Sci. Technol., vol. 16, pp. 1529-1532, 1979.
  64. T. H. Glisson, J. R. Hauser, M. A. Littlejohn, K. Hess, B. G. Streetman, and H. Shichijo, "Monte Carlo simulation of real-space electron transfer in GaAs-AlGaAs heterostructures," to be published in J. Appl. Phys.
  65. J. Bardeen, private communication.
  66. C. K. Kim and M. Lenzlinger, "Charge transfer in charge-coupled devices," J. Appl. Phys., vol. 42, pp. 3586-3594, 1971.
  67. T. J. Maloney and J. Frey, "Transient and steady-state electron transport properties of GaAs and InP," J. Appl. Phys., vol. 48, pp. 781-787, 1977.
  68. K. Hess, B. G. Streetman, H. Morkoç, U. S. patent pending.
  69. M. Keever, H. Shichijo, K. Hess, S. Banerjee, L. Witkowski, H. Morkoç, and B. G. Streetman, "Measurements of hot electron conduction and real-space transfer in GaAs-Al  $\text{Ga}_{1-x}\text{As}$  heterojunction layers," submitted



to Appl. Phys. Lett.

70. T. H. Ning, "Hot-electron emission from silicon into silicon dioxide," Solid-State Electron., vol. 21, pp. 273-282, 1978.
71. K. Hess and H. Shichijo, "The charge-handling capacity of buried-channel structures under hot-electron conditions," IEEE Trans. Electron Devices, vol. ED-27, pp. 503-504, 1980.
72. L. F. Eastman and M. S. Shur, "Substrate current in GaAs MESFETs," IEEE Trans. Electron Devices, vol. ED-26, pp. 1359-1361, 1979.
73. J. W. Harrison and J. R. Hauser, "Alloy scattering in ternary III-V compounds," Phys. Rev. B, vol. 13, pp. 5347-5350, 1976.
74. P. A. Wolff, "Theory of electron multiplication in silicon and germanium," Phys. Rev., vol. 95, pp. 1415-1420, 1954.
75. W. Shockley, "Problems related to p-n junctions in silicon," Solid-State Electron., vol. 2, pp. 35-67, 1961.
76. G. A. Baraff, "Distribution functions and ionization rates for hot electrons in semiconductors," Phys. Rev., vol. 128, pp. 2507-2517, 1962.
77. L. V. Keldysh, "Concerning the theory of impact ionization in semiconductors," Sov. Phys. JETP, vol. 21, pp. 1135-1144, 1965.
78. W. P. Dumke, "Theory of avalanche breakdown in InSb and InAs," Phys. Rev., vol. 167, pp. 783-789, 1968.
79. R. Chwang, C. W. Kao and C. R. Crowell, "Normalized theory of impact ionization and velocity saturation in nonpolar semiconductors via a Markov chain approach," Solid-State Electron., vol. 22, pp. 599-620, 1979.
80. C. L. Anderson and C. R. Crowell, "Threshold energies for electron-hole pair production by impact ionization in semiconductors," Phys. Rev. B, vol. 5, pp. 2267-2272, 1972.
81. J. R. Hauser, "Avalanche breakdown voltages for III-V semiconductors," Appl. Phys. Lett., vol. 33, pp. 351-353, 1978.

82. E. O. Kane, "The k p method," Semiconductors and Semimetals, (R. K. Willardson and A. C. Beers, eds.), vol. 1, Academic Press, New York, pp. 75-100, 1966.
83. P. A. Lebwohl and P. J. Price, "Hybrid method for hot electron calculations," Solid State Commun., vol. 9, pp. 1221-1224, 1971.
84. R. C. Curby and D. K. Ferry, "Impact ionization in narrow gap semiconductor," Phys. Status Solidi A, vol. 15, pp. 319-328, 1973.
85. M. L. Cohen and T. K. Bergstresser, "Band structure and pseudopotential form factors for fourteen semiconductors of the diamond and zinc-blend structures," Phys. Rev., vol. 141, pp. 789-796, 1966.
86. S. N. Shabde and C. Yeh, "Ionization rate in  $(\text{Al}_{1-x}\text{Ga}_x)\text{As}$ ," J. Appl. Phys., vol. 41, pp. 4743-4744, 1970.
87. G. E. Stillman, C. M. Wolfe, J. A. Rossi, and A. G. Foyt, "Unequal electron and hole impact ionization coefficients in GaAs," Appl. Phys. Lett., vol. 24, pp. 471-474, 1974.
88. H. D. Law and C. A. Lee, "Interband scattering effects on secondary ionization coefficients in GaAs," Solid-State Electron., vol. 21, pp. 331-340, 1978.
89. T. P. Pearsall, F. Capasso, R. E. Nahory, M. A. Pollack, and J. R. Chelikowsky, "The band structure dependence of impact ionization by hot carriers in semiconductors: GaAs," Solid-State Electron., vol. 21, pp. 297-302, 1978.
90. H. Ando and H. Kanbe, "Ionization coefficient measurement in GaAs by using multiplication noise characteristics," unpublished.
91. F. Capasso, R. E. Nahory, and M. A. Pollack, "Hot electron dynamics in GaAs avalanche devices: competition between ballistic behavior and intervalley scattering," Solid-State Electron., vol. 22, pp. 977-979, 1979.
92. G. A. Baraff, "Maximum anisotropy approximation for calculating electron distributions; application to high field transport in semiconductors," Phys. Rev., vol. 133, pp. A26-A33, 1964.

93. D. Brust, "Electronic spectra of crystalline germanium and silicon," Phys. Rev., vol. 134, pp. A1337-A1353, 1964.
94. H. Shichijo, K. Hess, and G. E. Stillman, "Orientation dependence of ballistic electron transport and impact ionization," Electron. Lett., vol. 16, pp. 208-210, 1980.
95. D. Matz, "Effect of nonparabolicity on non-ohmic transport in InSb and InAs," Phys. Rev., vol. 168, pp. 843-849, 1968.
96. J. L. Birman, M. Lax, and R. Loudon, "Intervalley-scattering selection rules in III-V semiconductors," Phys. Rev., vol. 145, pp. 620-622, 1966.
97. J. R. Chelikowsky and M. L. Cohen, "Nonlocal pseudopotential calculations for the electronic structure of eleven diamond and zinc-blend semiconductors," Phys. Rev. B, vol. 14, pp. 556-532, 1976.
98. T. P. Pearsall, private communication.
99. P. T. Landsberg and D. J. Robbins, "Impact ionization thresholds as generalization of van Hove singularities," J. Phys. C, vol. 10, pp. 2717-2739, 1977.
100. E. Antončík, "Quantum efficiency and overlap integrals in InSb," Czech. J. Phys. B, vol. 17, pp. 735-756, 1967.
101. D. J. Robbins, "Aspects of the theory of impact ionization in semiconductors (I)," Phys. Status Solidi B, vol. 97, pp. 9-50, 1980.
102. L. V. Keldysh, "Kinetic theory of impact ionization in semiconductors," Sov. Phys. JETP, vol. 10, pp. 509-513, 1960.
103. P. J. Vinson, C. Pickering, A. R. Adams, W. Fawcett, and G. D. Pitt, "The band structure of GaAs from transferred electron effects at high pressures," Proceedings of 13th International Conference on Physics of Semiconductors, pp. 1243-1246, Rome, 1976.
104. P. J. Price, private communication.
105. H. Kressel and G. Kupsky, "The effective ionization rate for hot carriers in GaAs," Int. J. Electron., vol. 20, pp. 535-543, 1966.

106. J. G. Ruch and G. S. Kino, "Transport properties of GaAs," Phys. Rev., vol. 174, pp. 921-931, 1968.
107. P. A. Houston and A. G. R. Evans, "Electron drift velocity in n-GaAs at high electric fields," Solid-State Electron., vol. 20, pp. 197-204, 1977.
108. R. Chwang and C. R. Crowell, "Effective threshold energy for pair production in nonpolar semiconductors," Solid State Commun., vol. 20, pp. 169-172, 1976.
109. C. W. Kao and C. R. Crowell, "Impact ionization by electrons and holes in InP," Solid-State Electron., vol. 23, pp. 881-891, 1980.
110. J. J. Berenz, J. Kinoshita, T. L. Hierl, and C. A. Lee, "Orientation dependence of n-type GaAs intrinsic avalanche response time," Electron. Lett., vol. 15, pp. 150-152, 1979.
111. Y. Okuto and C. R. Crowell, "Ionization coefficients in semiconductors: A nonlocalized property," Phys. Rev. B, vol. 10, pp. 4284-4296, 1974.

## APPENDIX 1

Total Scattering Rates and Angular Dependences  
of Various Scattering Mechanisms

In this appendix formulas for the total scattering rates and the angular dependences of various scattering mechanisms for charge carriers with wave vector  $\vec{k}$  are summarized. These equations are needed for the Monte Carlo calculations described in the text.

In general the transition rate from wave vector  $\vec{k}$  to  $\vec{k}'$  is given by the golden rule:

$$S(\vec{k}, \vec{k}') = \frac{2\pi}{\hbar} |H_{fi}|^2 \delta(E_f - E_i) \quad (A1.1)$$

where  $H_{fi}$  is the matrix element of the perturbing potential  $H$  between the initial and final states. The angular dependence of  $S(\vec{k}, \vec{k}')$  gives directly the angular dependence of the scattering. The total scattering rate out of the state  $\vec{k}$  is obtained by summing over all the final state  $\vec{k}'$ .

Therefore,

$$\frac{1}{\tau} = \frac{V}{(2\pi)^3} \int_0^\infty dk' \int_0^\pi d\beta \int_0^{2\pi} d\alpha S(\vec{k}, \vec{k}') k'^2 \sin\beta \quad (A1.2)$$

where  $V$  is the volume of the crystal, and  $\beta$  is the angle between  $\vec{k}$  and  $\vec{k}'$ .

Wherever possible, the effect of non-parabolic bands and the admixture of p-type valence band wave functions in the  $\Gamma$  valley will be included in the formalism. All the figures include non-parabolicity, but not the admixture of p-type wave functions. Non-parabolicity is defined by the relationship

$$\frac{\hbar^2 k^2}{2m^*} = \gamma(E) = E(1 + \alpha E). \quad (A1.3)$$

### 1. Polar Optical Scattering [33]

The transition rate for polar optical scattering is given by

$$S_o(\vec{k}, \vec{k}') = \frac{2\pi}{\hbar} B_o(\vec{k}, \vec{k}') \times \begin{cases} N_o \delta[E(k') - E(k) - \hbar\omega_o] & (\text{absorption}) \\ (N_o + 1) \delta[E(k') - E(k) + \hbar\omega_o] & (\text{emission}) \end{cases} \quad (\text{A1.4})$$

where

$$B_o(\vec{k}, \vec{k}') = \frac{2\pi e^2 \hbar \omega_o}{4\pi \epsilon_o V |\vec{k} - \vec{k}'|^2} \left( \frac{1}{\epsilon_o} - \frac{1}{\epsilon_\infty} \right) G(\vec{k}, \vec{k}') \quad (\text{A1.5})$$

In these expressions  $\omega_o$  is the optical phonon frequency and  $N_o$  is the thermodynamic average value of the optical phonon number, which is in equilibrium:

$$N_o = \frac{1}{\exp(\hbar\omega_o/k_B T) - 1} \quad (\text{A1.6})$$

$$G(\vec{k}, \vec{k}') = \frac{1}{2} \sum_{\mu, \mu'} \int d\vec{r} u_{\mu, \vec{k}'}^*(\vec{r}) u_{\mu, \vec{k}}(\vec{r}) \quad (\text{A1.7})$$

is the overlap integral between the periodic parts of the Bloch functions at  $\vec{k}$  and  $\vec{k}'$  summed over the doubly degenerate final spin states and averaged over the initial spin states. It is given by

$$G(\vec{k}, \vec{k}') = (a_k a_{k'} + c_k c_{k'} \cos \beta)^2 \quad (\text{A1.8})$$

where

$$a_k = \left[ \frac{1 + \alpha E(k)}{1 + 2\alpha E(k)} \right]^{\frac{1}{2}} \quad (\text{A1.9})$$

$$c_k = \left[ \frac{\alpha E(k)}{1 + 2\alpha E(k)} \right]^{\frac{1}{2}} \quad (\text{A1.10})$$

For s-type wave functions we let  $\alpha \rightarrow 0$  and  $G(\vec{k}, \vec{k}') = 1$ .

The total scattering rate is calculated as

$$\frac{1}{\tau_{po}} = \frac{em^* \omega_o}{4\pi\epsilon_o \sqrt{2} \hbar} \left( \frac{1}{\epsilon_\infty} - \frac{1}{\epsilon_o} \right) \frac{(1+2\alpha E')}{\gamma^{1/2}(E)} F_o(E, E') \times \frac{N_o}{(N_o+1)} \quad (A1.11)$$

where

$$E' = \begin{cases} E + \hbar\omega_o & (\text{absorption}) \\ E - \hbar\omega_o & (\text{emission}) \end{cases} \quad (A1.12)$$

and

$$F_o(E, E') = C^{-1} \left\{ A \ln \left| \frac{\gamma^{1/2}(E) + \gamma^{1/2}(E')}{\gamma^{1/2}(E) - \gamma^{1/2}(E')} \right| + B \right\} \quad (A1.13)$$

$$A = [2(1+\alpha E)(1+\alpha E') + \alpha \{\gamma(E) + \gamma(E')\}]^2 \quad (A1.14)$$

$$B = -2\alpha \gamma^{1/2}(E) \gamma^{1/2}(E') [4(1+\alpha E)(1+\alpha E') + \alpha \{\gamma(E) + \gamma(E')\}] \quad (A1.15)$$

$$C = 4(1+\alpha E)(1+\alpha E')(1+2\alpha E)(1+2\alpha E') . \quad (A1.16)$$

To recover the result for non-parabolic bands without taking account of the admixture of p-functions we let  $\alpha \rightarrow 0$  in A, B and C, then  $A=C=4$  and  $B=0$ . Quite often an "effective field strength" defined as

$$E_o = \frac{m^* e \hbar \omega_o}{4\pi\epsilon_o \hbar^2} \left( \frac{1}{\epsilon_\infty} - \frac{1}{\epsilon_o} \right) \quad (A1.17)$$

is used in the total scattering rate. It has the value of  $E_o = 5.95$  kV/cm for the  $\Gamma$  valley of GaAs.

From Eqs. (A1.5) and (A1.8) we obtain the angular dependence of the scattering

$$P(\beta)d\beta \sim \frac{\left[ \sqrt{\frac{1+\alpha E}{1+2\alpha E}} \sqrt{\frac{1+\alpha E'}{1+2\alpha E'}} + \sqrt{\frac{\alpha E}{1+2\alpha E}} \sqrt{\frac{\alpha E'}{1+2\alpha E'}} \cos \beta \right]^2}{[\gamma(E) + \gamma(E') - 2\gamma^{\frac{1}{2}}(E)\gamma^{\frac{1}{2}}(E') \cos \beta]} \sin \beta d\beta. \quad (A1.18)$$

To realize this probability distribution using uniformly distributed random numbers, von Neumann's rejection method can be used [33,38]. For parabolic bands with  $\alpha = 0$ , we have

$$P(\beta)d\beta \sim \frac{\sin \beta d\beta}{[E+E' - 2\sqrt{EE'} \cos \beta]}. \quad (A1.19)$$

In this case using random numbers,  $r$ , equally distributed between 0 and 1 gives

$$r = \int_0^\beta P(\beta)d\beta \quad (A1.20)$$

or

$$\cos \beta = [(1+f) - (1+2f)^r] / f \quad (A1.21)$$

where

$$f = 2\sqrt{EE'} / (\sqrt{E} - \sqrt{E'})^2. \quad (A1.22)$$

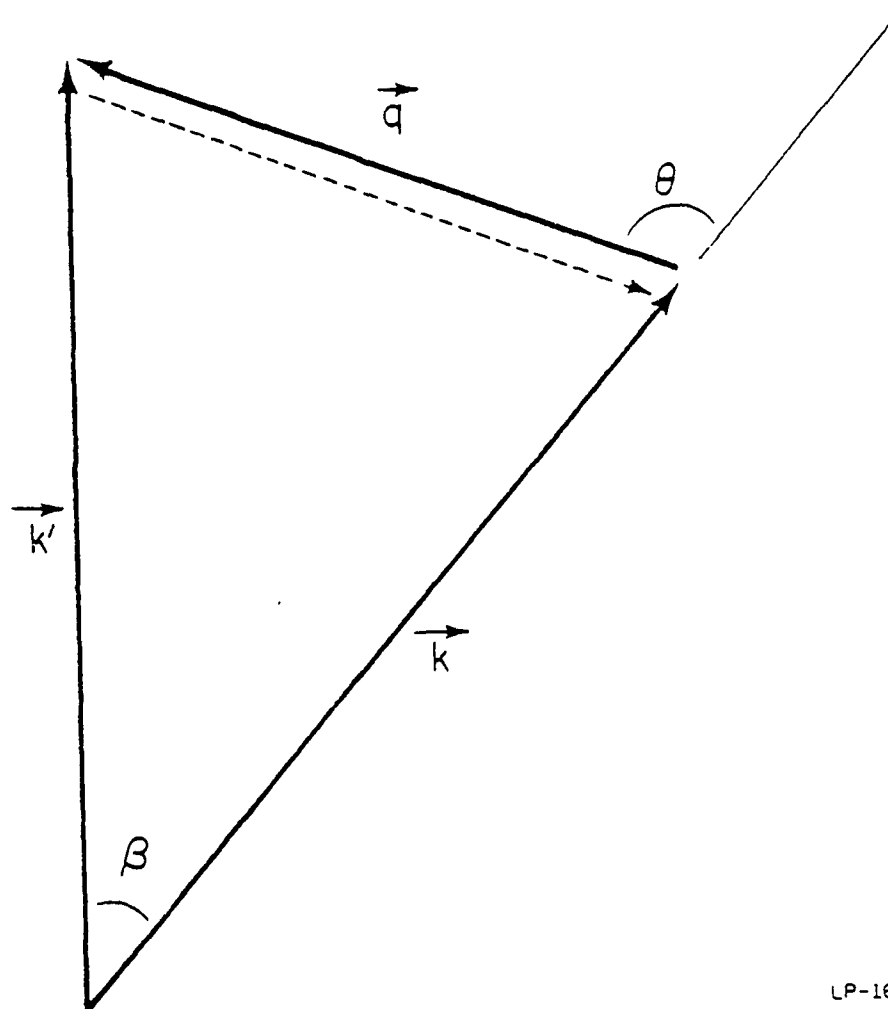
When  $\beta$  has been determined, a further random number determines the azimuthal angle between 0 and  $2\pi$ , and then  $\vec{k}'$  is completely specified.

In actual Monte Carlo calculations, however, it is sometimes more convenient to specify the phonon vector  $q = \vec{k}' - \vec{k}$  (for the case of phonon absorption) by the vector length  $q = |\vec{q}|$  and the angle  $\theta$  between  $\vec{k}$  and  $\vec{q}$  (Fig. A.1). Making use of

$$q^2 = k^2 + k'^2 - 2kk' \cos \beta \quad (A1.23)$$

and Eq. (A1.21) with





LP-1663

Fig. A.1. Vector diagram illustrating momentum balance in a scattering process. An electron scatters from state  $\vec{k}$  to state  $\vec{k}'$  with emission (dashed line) or absorption (solid line) of a phonon.

$$f = \frac{2\sqrt{r(E)r(E')}}{[\sqrt{r(E)} - \sqrt{r(E')}]^2} \quad (\text{A1.24})$$

appropriate for s-type wave functions, it is possible to show that

$$q = \frac{\sqrt{\frac{2m^*}{\hbar}}}{\hbar} |\sqrt{\gamma(E')} - \sqrt{\gamma(E)}| \cdot \left| \frac{\sqrt{r(E')} + \sqrt{r(E)}}{\sqrt{r(E')} - \sqrt{r(E)}} \right|^r. \quad (\text{A1.25})$$

Once  $q$  has been determined,  $\cos \theta$  is calculated from

$$k'^2 = q^2 + k^2 \pm 2qk \cos \theta \quad (\text{A1.26})$$

with the result

$$\cos \theta = \frac{\frac{\frac{2m^*}{\hbar^2} \cdot \hbar \omega_o [1 + \alpha(2E \pm \hbar \omega_o)] \pm q^2}{2q \cdot \frac{1}{\hbar} \sqrt{\frac{2m^*}{\hbar} \gamma(E)}}}{\quad} \quad (\text{A1.27})$$

where upper and lower signs correspond to absorption and emission of a phonon respectively. Using random azimuthal angles relative to  $\vec{k}$  as before,  $\vec{k}'$  again can be specified.

In Fig. A.2 the energy dependence of the polar optical scattering rate in the  $\Gamma$  valley of GaAs at 300°K is shown. Fig. A.3 shows the angular dependence of the scattering probability for electron energies of 0.1 eV and 0.4 eV.

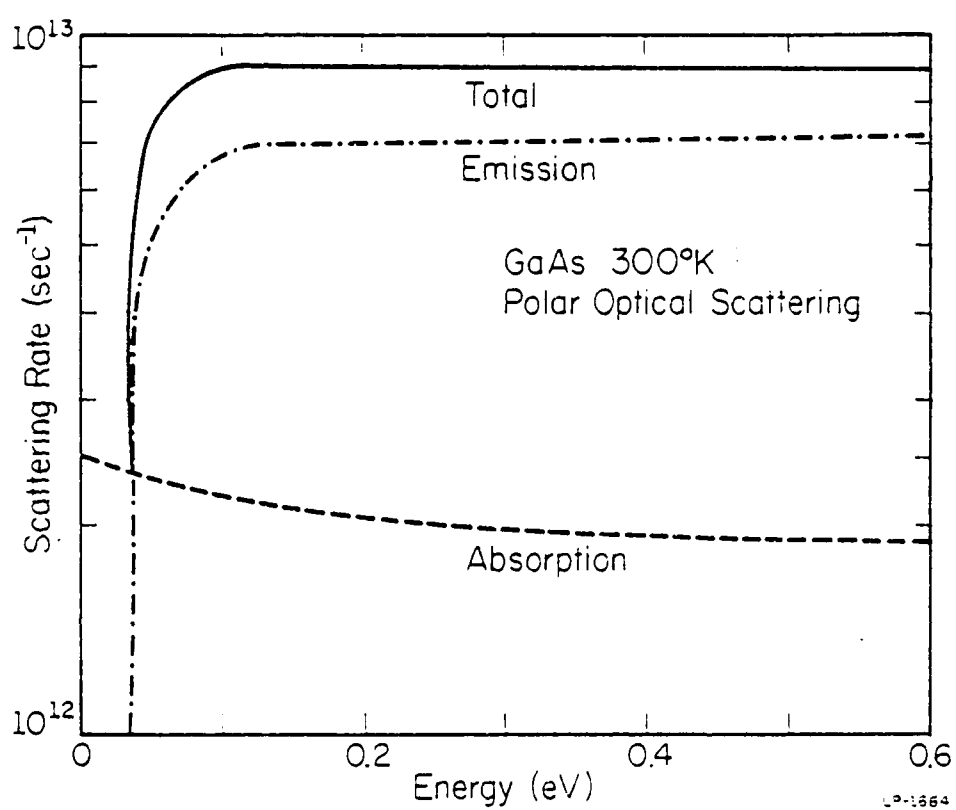


Fig. A.2. Energy dependence of the polar optical scattering rate for the  $\Gamma$  valley of GaAs (300 K).

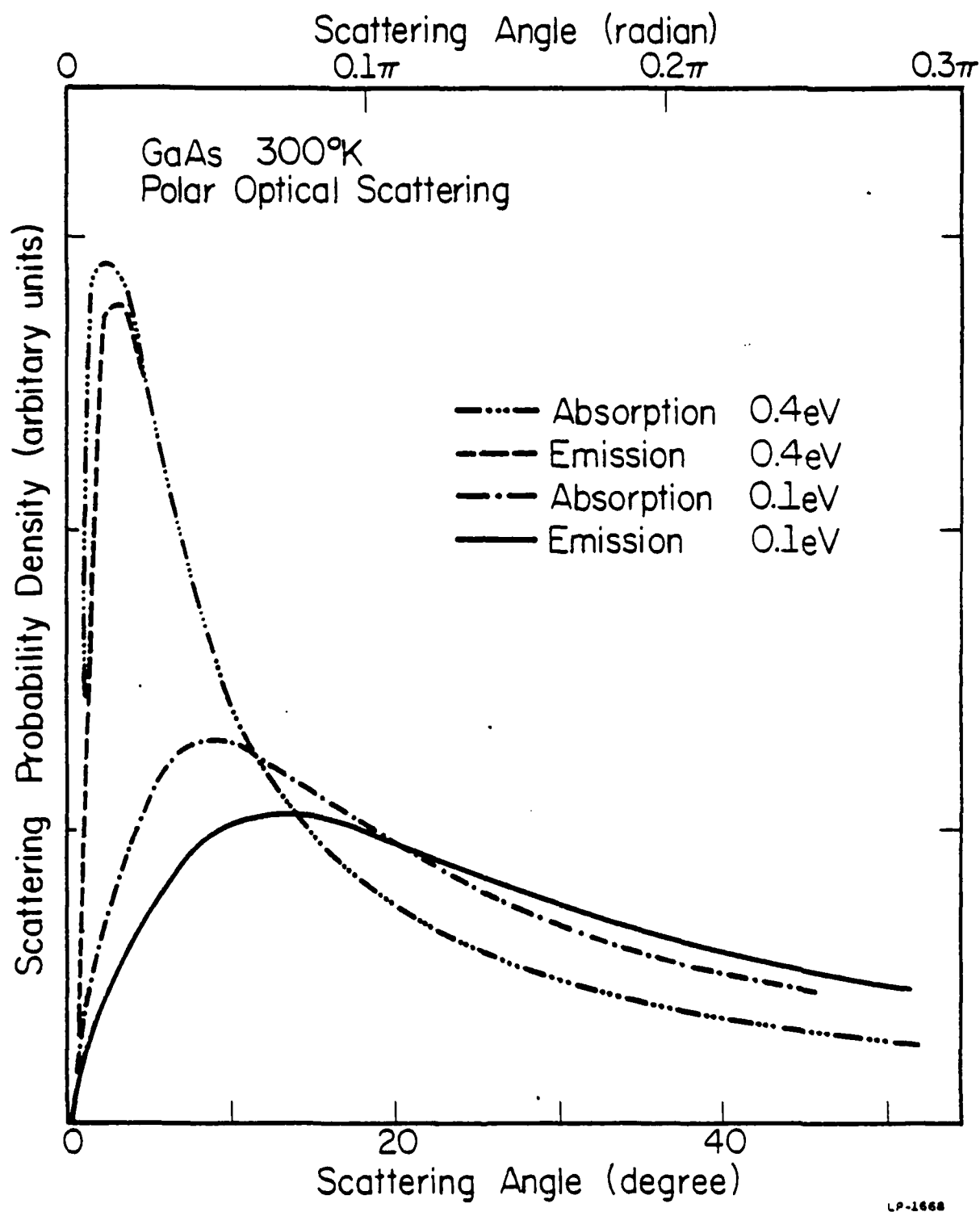


Fig. A.3. Angular distribution of the polar optical scattering probability for electrons with energies of 0.1 or 0.4 eV.

## 2. Non-equivalent Intervalley Scattering [33]

We distinguish two types of valleys by suffices  $i$  and  $j$ . The transition rate from  $\vec{k}$  in valley  $i$  to  $\vec{k}'$  in valley  $j$  is

$$S_{ij}(\vec{k}, \vec{k}') = \frac{2\pi}{\hbar} B_{ij}(\vec{k}, \vec{k}') \times \begin{cases} N_{ij} \delta [E_j(k') - E_i(k) + \Delta_j - \Delta_i - \hbar\omega_{ij}] \\ (N_{ij}+1) \delta [E_j(k') - E_i(k) + \Delta_j - \Delta_i + \hbar\omega_{ij}] \end{cases} \quad (A1.28)$$

where

$$B_{ij}(\vec{k}, \vec{k}') = Z_j \frac{\hbar}{2\rho\omega_{ij}V} D_{ij}^2 G_{ij}(\vec{k}, \vec{k}') \quad (A1.29)$$

and  $\omega_{ij}$  is the intervalley phonon frequency,  $Z_j$  is the number of valleys of type  $j$ ,  $D_{ij}$  is the intervalley deformation potential,  $\rho$  is the density and  $N_{ij}$  is the intervalley phonon occupation number given by the Bose distribution:

$$N_{ij} = \frac{1}{\exp(\hbar\omega_{ij}/k_B T) - 1} \quad (A1.30)$$

The energy is measured from the minimum of the valley which is denoted by  $\Delta_i$  and  $\Delta_j$  for valleys  $i$  and  $j$  respectively. The function  $G_{ij}(\vec{k}, \vec{k}')$  is given by an equation analogous to Eq. (A1.8) but here we ignore the admixture of p-functions and let  $G(\vec{k}, \vec{k}') = 1$ . The total scattering rate is then

$$\frac{1}{\tau_{ij}} = \frac{Z_j D_{ij}^2 (m_j^*)^3}{\sqrt{2} \tau_0 \hbar^2 (\hbar\omega_{ij})} \gamma_j^{1/2} (E') (1 + 2\alpha_j E') \times \begin{cases} N_{ij} & \text{(absorption)} \\ (N_{ij}+1) & \text{(emission)} \end{cases} \quad (A1.31)$$

where

$$E' = \begin{cases} E_i - \Delta_j + \Delta_i + \hbar\omega_{ij} & (\text{absorption}) \\ E_i - \Delta_j + \Delta_i - \hbar\omega_{ij} & (\text{emission}) \end{cases} \quad (\text{A1.32})$$

All the intervalley scattering processes including equivalent intervalley scattering (explained in the next section) are completely randomizing, i.e. there is no dependence on the scattering direction. Therefore using random numbers,  $r$ , we have

$$r = \frac{1}{2} \int_0^\beta \sin\theta d\theta \quad (\text{A1.33})$$

or

$$\cos\beta = 1 - 2r. \quad (\text{A1.34})$$

Fig. A.4 shows the energy dependence of the intervalley scattering rates from the  $\Gamma$  valley to the L and X valleys of GaAs at 300°K.

### 3. Equivalent Intervalley Scattering [33]

The transition rate is given by

$$S_e(\vec{k}, \vec{k}') = \frac{2\pi}{\hbar} B_e(\vec{k}, \vec{k}') \times \begin{cases} N_e \delta[E(k') - E(k) - \hbar\omega_e] \\ (N_e + 1) \delta[E(k') - E(k) + \hbar\omega_e] \end{cases} \quad (\text{A1.35})$$

where

$$B_e(\vec{k}, \vec{k}') = (Z_e - 1) \frac{\hbar}{2\rho\omega_e V} D_e^2 \quad (\text{A1.36})$$

and  $\omega_e$  is the intervalley phonon frequency,  $D_e$  is the deformation potential,

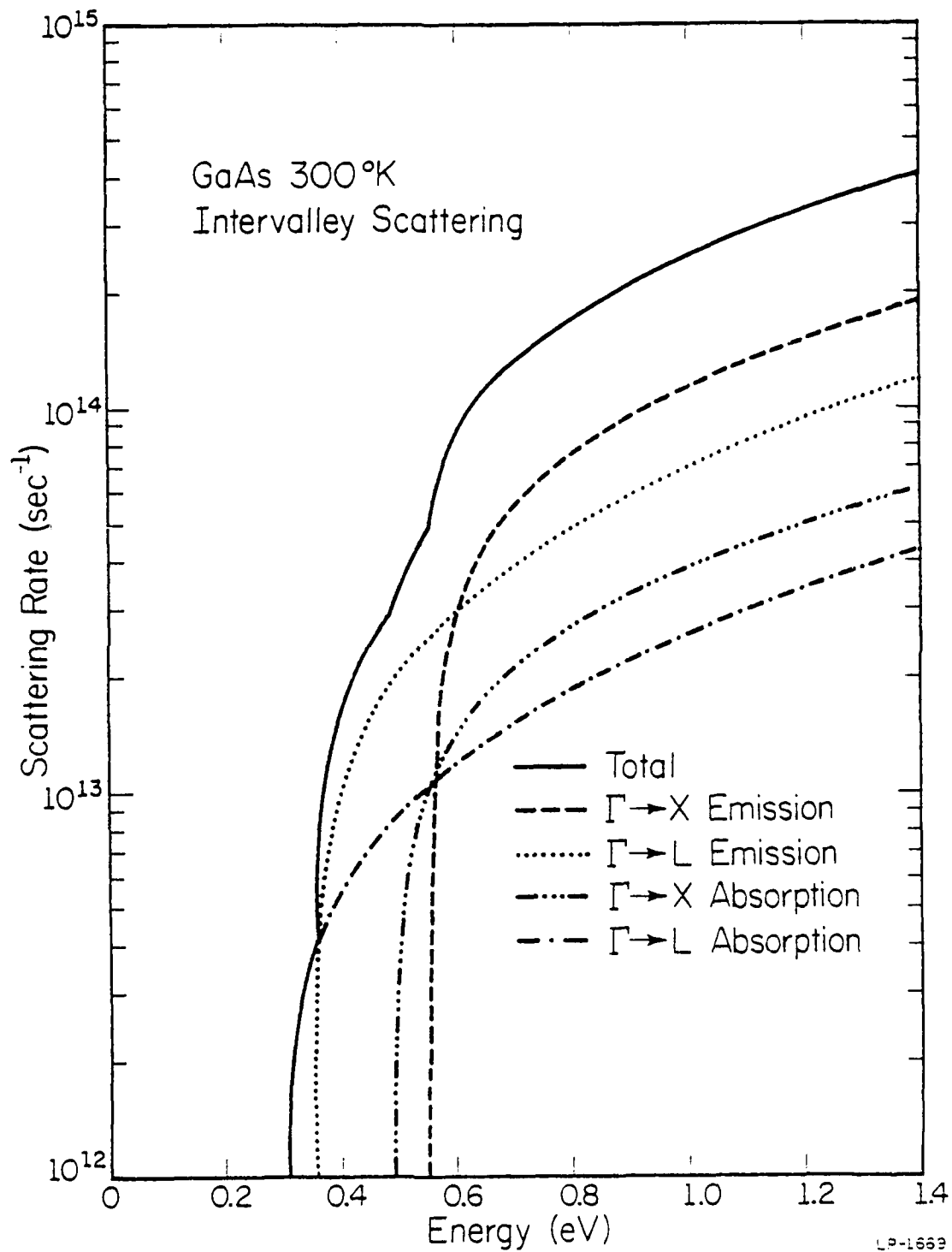


Fig. A.4. Energy dependence of the intervalley scattering rate in the  $\Gamma$  valley of GaAs (300 K). The L and X valleys are 0.33 and 0.522 eV away from the  $\Gamma$  band edge respectively.

and  $Z_e$  is the number of equivalent valleys.  $N_e$  is the thermal equilibrium number of phonons per mode given by

$$N_e = \frac{1}{\exp(\hbar\omega_e/k_B T) - 1} \quad (A1.37)$$

The total scattering rate is calculated as

$$\frac{1}{\tau_e} = (Z_e - 1) \frac{(m^*)^{3/2} D_e^2}{\sqrt{2} \pi \rho \hbar^2 (\hbar\omega_e)} \gamma^{1/2}(E') (1 + 2\alpha E') \begin{cases} N_e \\ (N_e + 1) \end{cases} \quad (A1.38)$$

where

$$E' = \begin{cases} E(k) + \hbar\omega_e & (\text{absorption}) \\ E(k) - \hbar\omega_e & (\text{emission}) \end{cases} \quad (A1.39)$$

In Fig. A.5 the energy dependence of the equivalent and non-equivalent (L valley to  $\Gamma$  valley) scattering rates in the L valley of GaAs at 300°K is shown.

#### 4. Acoustic Phonon Scattering [33]

We assume that the energy of the acoustic phonon is negligible compared with  $k_B T$ , and neglect the change in the electron energy during the scattering. Including both absorption and emission, we have

$$S_a(\vec{k}, \vec{k}') = \frac{2\pi}{\hbar} B_a(\vec{k}, \vec{k}') N_a \delta[E(k') - E(k)] \quad (A1.40)$$

where

$$B_a(\vec{k}, \vec{k}') = 2 \frac{\hbar \Xi_a^2}{2\rho sV} |\vec{k} - \vec{k}'| G(\vec{k}, \vec{k}') \quad (A1.41)$$



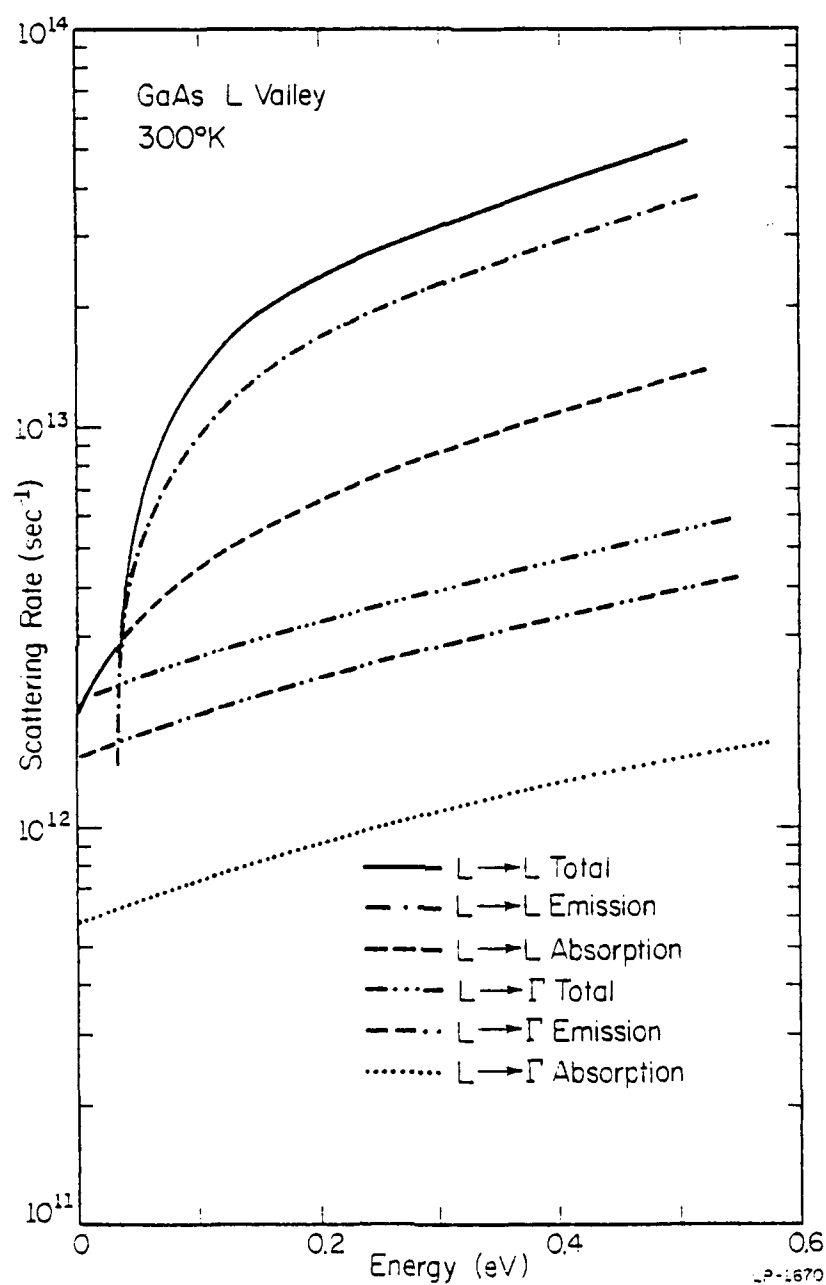


Fig. A.5. Energy dependence of the equivalent (L to L) and non-equivalent (L to  $\Gamma$ ) intervalley scattering rate in the L valley of GaAs (300 K).

and

$$N_a = \frac{1}{\exp\left(\frac{\hbar s |\vec{k} - \vec{k}'|}{k_B T}\right) - 1} \cong \frac{k_B T}{\hbar s |\vec{k} - \vec{k}'|} \quad (\text{equipartition}). \quad (\text{A1.42})$$

$G(\vec{k}, \vec{k}')$  is given by Eq. (A1.8). In these expressions  $\rho$  is the density,  $s$  is the velocity of sound, and  $\Xi_a$  is the deformation potential.

The total scattering rate is given by

$$\frac{1}{\tau_a} = \frac{(2m^*)^{3/2} k_B T \Xi_a^2}{2\pi \rho s \hbar^4} \gamma^{1/2}(E) (1+2\alpha E) F_a(E) \quad (\text{A1.43})$$

where

$$F_a(E) = \frac{(1+\alpha E)^2 + \frac{1}{3}(\alpha E)^2}{(1+2\alpha E)^2}. \quad (\text{A1.44})$$

To recover the result for a non-parabolic band alone we set  $\alpha = 0$  in  $F_a(E)$ .

The angular dependence is obtained from Eqs. (A1.18), (A1.38), (A1.39) and (A1.40) with the result

$$P(\beta) d\beta \sim [(1+\alpha E) + \alpha E \cos \beta]^2 \sin \beta d\beta. \quad (\text{A1.45})$$

With random numbers,  $r$ , the angle  $\beta$  can be determined by

$$\cos \beta = \frac{[(1+2\alpha E)^3(1-r)+r]^{1/3} - (1+\alpha E)}{\alpha E}. \quad (\text{A1.46})$$

When  $\alpha = 0$ , the scattering is completely randomizing.

In Figs. A.6 and A.7 the energy dependence of the scattering rate and the angular dependence are shown for the  $\Gamma$  valley of GaAs at 300°K. As seen from Fig. A.6 the acoustic phonon scattering rate is negligible compared with polar optical scattering rate and intervalley scattering rate in polar

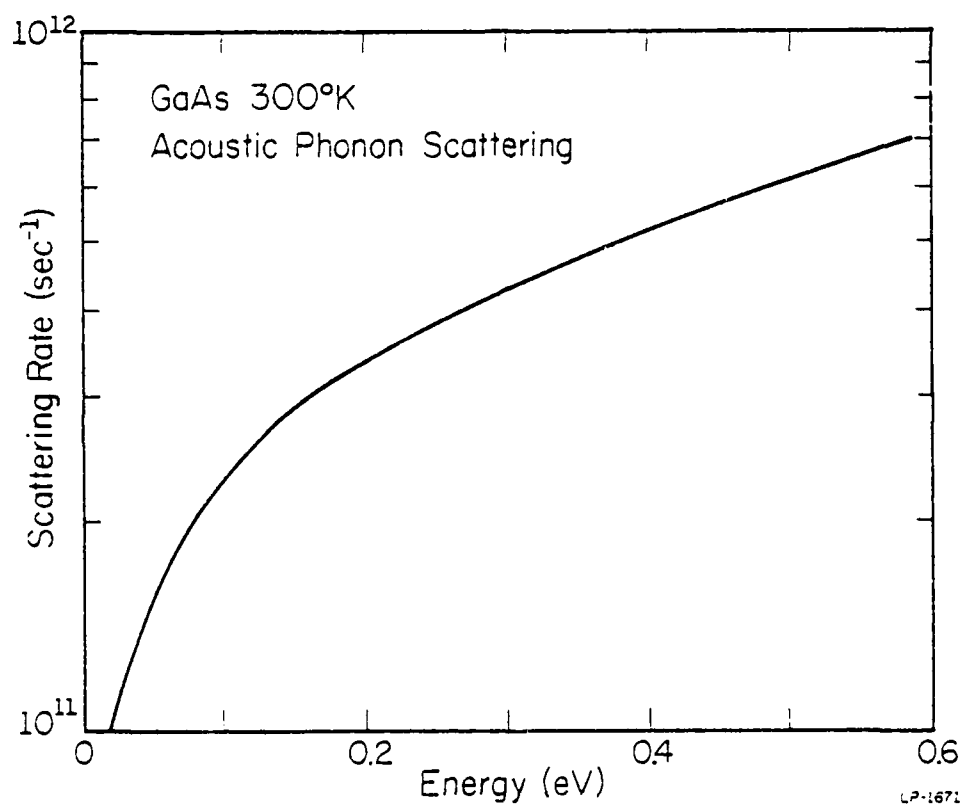


Fig. A.6. Energy dependence of the acoustic phonon scattering rate in the valley of GaAs (300 K).

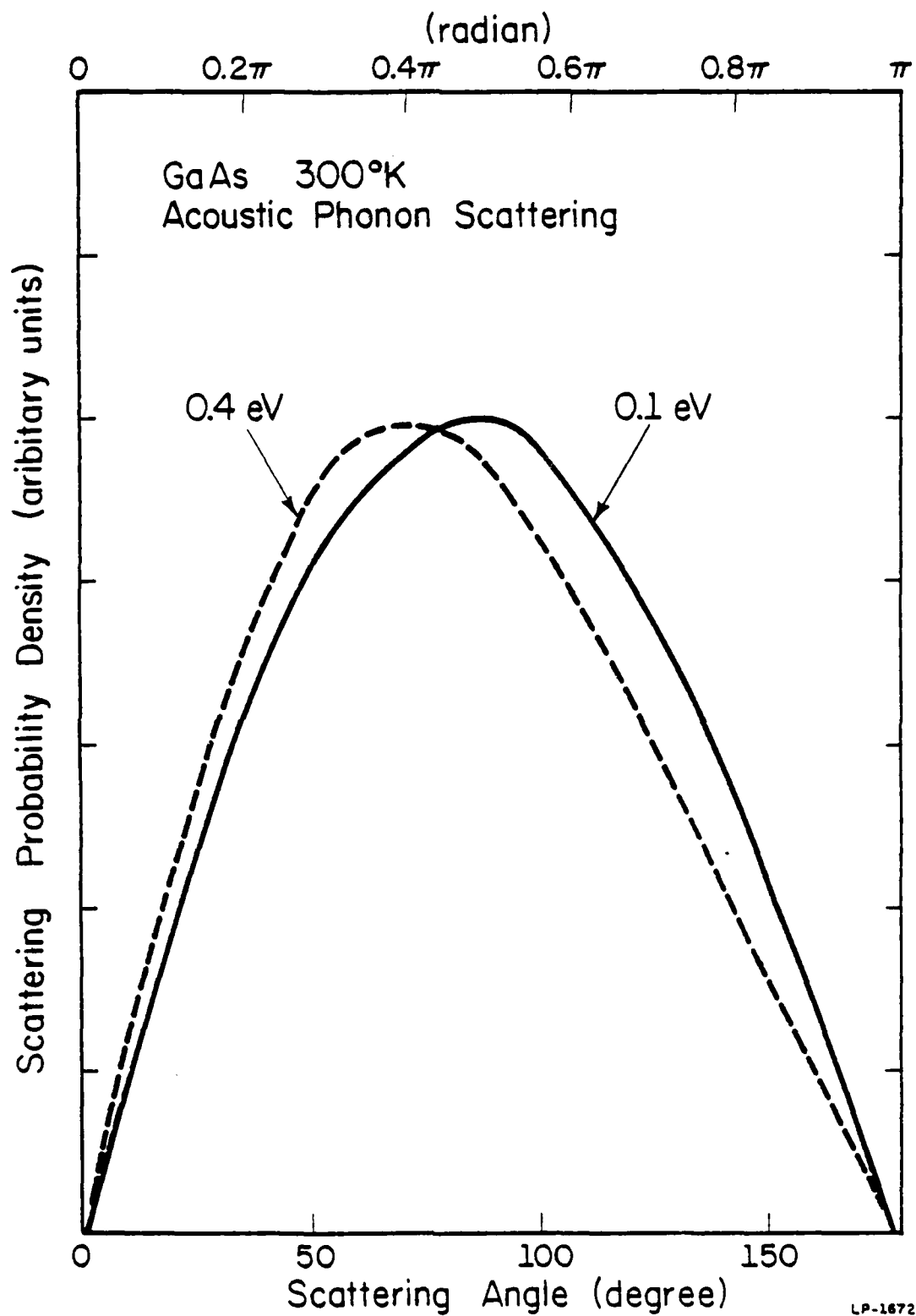


Fig. A.7. Angular distribution of scattering by acoustic phonons for electrons with energies of 0.1 and 0.4 eV.

materials.

### 5. Intravalley Non-polar Optical Scattering [33]

In non-polar materials the hamiltonian matrix element of non-polar optical scattering vanishes for s-like band minima. This is also true for the III-V semiconductors with their s-like conduction bands. Consequently, this process needs only be considered at high energies. At these energies it is probable that intervalley scattering dominates in most of the III-V semiconductors. Therefore, non-polar optical scattering is commonly neglected.

The formula for non-polar optical scattering is very similar to the one for intervalley scattering. The total scattering rate is given by

$$\frac{1}{\tau_o} = \frac{D_o^2 (m^*)^{3/2}}{\sqrt{2}\pi\hbar^2 \rho (\hbar\omega_o)} \gamma^{1/2}(E') (1+2\alpha E') \times \begin{cases} N_o \\ (N_o+1) \end{cases} \quad (A1.47)$$

where

$$E' = \begin{cases} E + \hbar\omega_o & (\text{absorption}) \\ E - \hbar\omega_o & (\text{emission}) \end{cases} \quad (A1.48)$$

and

$$N_o = \frac{1}{\exp(\hbar\omega_o/k_B T) - 1} \quad (A1.49)$$

$D_o$  is the optical deformation potential.

### 6. Piezoelectric Scattering [27]

In cubic crystals lacking inversion symmetry, the piezoelectric stress tensor is nonvanishing and electrons are scattered by the piezoelectric fields. However, piezoelectric scattering is important only at

low temperatures in high-purity materials. Taking into account screening, the transition rate can be written as

$$S(\vec{k}, \vec{k}') = \frac{2\pi}{\hbar} \left( \frac{eP_z}{\epsilon\epsilon_0} \right)^2 \frac{k_B T}{2VC_\ell} \frac{G(\vec{k}, \vec{k}')}{|\vec{k} - \vec{k}'| + 1/L_D^2} \delta(E - E') \quad (A1.50)$$

where  $P_z$  is the piezoelectric constant,  $C_\ell = \rho s^2$  is the longitudinal elastic constant, and  $L_D$  is the Debye length given by

$$L_D = \sqrt{\frac{\epsilon\epsilon_0 k_B T}{e^2 n}}. \quad (A1.51)$$

To calculate the total scattering rate, we let  $G(\vec{k}, \vec{k}') = 1$  and integrate over the final state  $\vec{k}'$ . Including both phonon absorption and emission, we get

$$\frac{1}{\tau_{pz}} = \frac{m^*}{4\pi\hbar^2} \left( \frac{eP_z}{\epsilon\epsilon_0} \right)^2 \frac{k_B T}{C_\ell} \frac{1 + 2\alpha E}{\sqrt{2m^*} \gamma(E)} \ln \left[ 1 + \frac{8m^* L_D^2}{\hbar^2} \gamma(E) \right]. \quad (A1.52)$$

From Eq. (A1.50) the angular dependence is given by

$$P(\beta) d\beta \sim \frac{\sin\beta d\beta}{\left[ \gamma(E) + \frac{\hbar^2}{4m^* L_D^2} - \gamma(E) \cos\beta \right]}. \quad (A1.53)$$

Using random numbers,  $r$ , we can realize this distribution as

$$\cos\beta = 1 + \frac{\hbar^2}{4m^* L_D^2 \gamma(E)} \left\{ 1 - \left[ 1 + \frac{8m^* L_D^2}{\hbar^2} \gamma(E) \right]^r \right\}. \quad (A1.54)$$

If one wishes to determine the phonon wave vector  $\vec{q} = \vec{k}' - \vec{k}$  first,

it is given by

$$q = \frac{1}{L_D} \sqrt{1 + \frac{8m^* L_D^2 \gamma(E) \gamma - 1}{h^2}} \quad (\text{A1.55})$$

and  $\cos\theta$  is calculated as in Eq. (A1.27).

### 7. Ionized Impurity Scattering [35]

The transition rate is given by

$$S(\vec{k}, \vec{k}') = \frac{32\pi^3 (8e^2)^2 N_I}{(4\pi\epsilon\epsilon_0)^2 \hbar v} \frac{G(\vec{k}, \vec{k}')}{(|\vec{k} - \vec{k}'|^2 + \lambda^2)^2} \delta(E - E') \quad (\text{A1.56})$$

where  $N_I$  is the impurity concentration and  $\lambda = 1/L_D$  is the inverse screening distance.  $G(\vec{k}, \vec{k}')$  is given by Eq. (A1.8). The total scattering rate is calculated as

$$\frac{1}{\tau_{im}} = \frac{2\pi (Ze^2)^2 N_I}{(4\pi\epsilon\epsilon_0)^2 m^{*1/2}} \cdot \frac{1 + 2\alpha E}{E^{3/2} (1 + \alpha E)^{3/2}} \times \left\{ \frac{[1 + 2c_k^2 (\lambda/2k)^2]^2}{4(\lambda/2k)^2 [1 + (\lambda/2k)^2]} + c_k^2 [1 + 2c_k^2 (\frac{\lambda}{2k})^2] \ln \left[ \frac{(\lambda/2k)^2}{1 + (\lambda/2k)^2} \right] + c_k^4 \right\} \quad (\text{A1.57})$$

where  $c_k$  is given by Eq. (A1.10). In most cases of interest  $(2k/\lambda)^2 \gg c_k^2$ . Therefore, we get

$$\frac{1}{\tau_{im}} = \frac{N_I}{32\pi\sqrt{2m^*}} \left( \frac{Ze^2}{\epsilon\epsilon_0} \right)^2 \frac{1}{(\lambda/2k)^2 [1 + (\lambda/2k)^2]} \frac{1 + 2\alpha E}{E^{3/2} (1 + \alpha E)^{3/2}} \quad (\text{A1.58})$$

For the angular dependence of scattering we let  $G(\vec{k}, \vec{k}) = 1$ .

Then, from Eq. (A1.56), we have

$$P(\beta) d\beta \sim \frac{\sin\beta d\beta}{(4k^2 \sin^2 \frac{\beta}{2} + \lambda^2)^2} \quad (\text{A1.59})$$

By using random numbers,  $r$ , we get

$$\cos\beta = 1 - \frac{2(1-r)}{1 + r (4k^2/\lambda^2)} \quad (\text{A1.60})$$

In terms of  $\vec{q} = \vec{k}' - \vec{k}$ , this can be rewritten as

$$q = \frac{2k \sqrt{1-r}}{\sqrt{1 + r (4k^2/\lambda^2)}} \quad (\text{A1.61})$$

and  $\cos\theta$  is given by

$$\cos\theta = -q/2k. \quad (\text{A1.62})$$

Fig. A.8 shows the energy dependence of the ionized impurity scattering rate for uncompensated GaAs doped with  $N_D = 1 \times 10^{17} \text{ cm}^{-3}$  and for compensated GaAs doped with  $N_D = 1.1 \times 10^{18} \text{ cm}^{-3}$  and  $N_A = 1 \times 10^{18} \text{ cm}^{-3}$  which gives an electron density of  $1 \times 10^{17} \text{ cm}^{-3}$ . In uncompensated material the scattering rate depends very little on the impurity doping density due to screening. Fig. A.9 shows the angular dependence of ionized impurity scattering for electron energies of 0.1 eV and 0.3 eV and two different electron densities,  $1 \times 10^{16} \text{ cm}^{-3}$  and  $1 \times 10^{17} \text{ cm}^{-3}$ . As can be seen from this figure ionized impurity scattering gives small scattering angles.

#### 8. Alloy Scattering [73]

Here we adopt the model developed by Harrison and Hauser. They assume the crystal to have a uniform background potential with square wells of depth  $\Delta E$  and extent  $r \leq r_0$  at random sites associated with one of the alloying constituents. They arbitrarily take  $r_0$  to be the nearest-neighbor



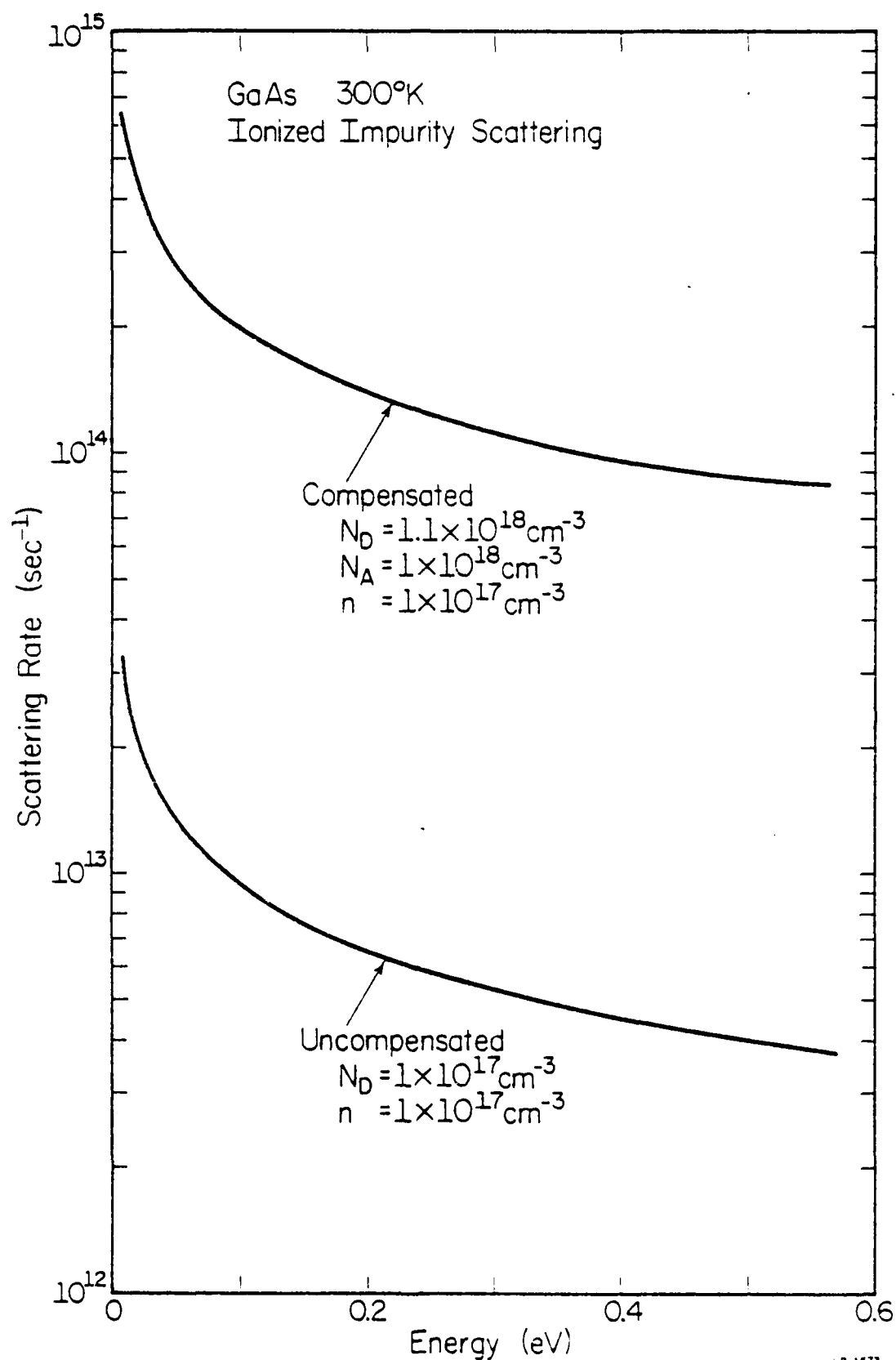


Fig. A.8. Energy dependence of ionized impurity scattering in uncompensated and compensated GaAs (300 K).

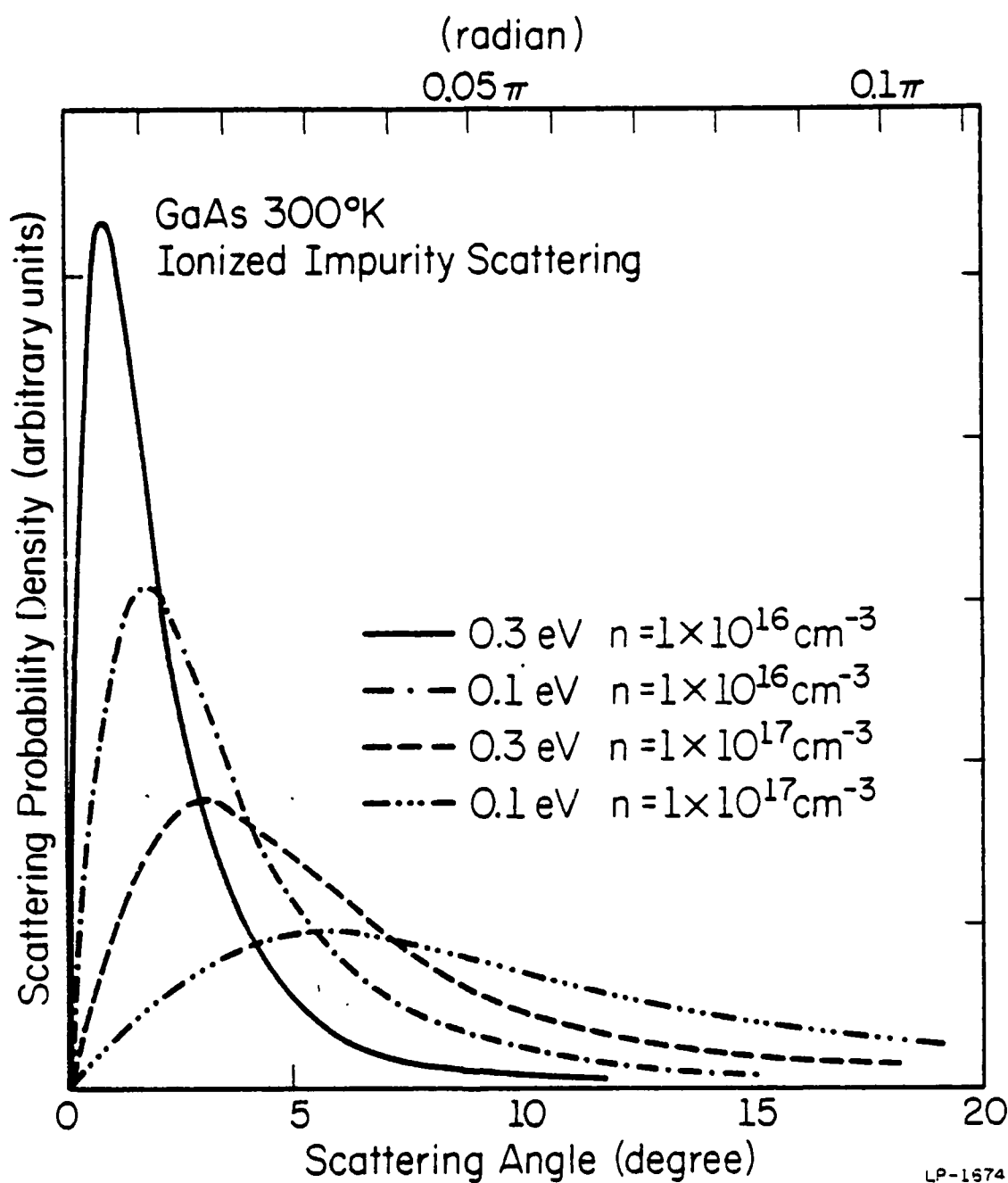


Fig. A.9. Angular distribution of scattering probability by an ionized impurity for electrons with energies of 0.1 and 0.4 eV and electron densities of  $1 \times 10^{16} \text{ cm}^{-3}$  and  $1 \times 10^{17} \text{ cm}^{-3}$ .

separation, or  $\frac{1}{4}\sqrt{3}a$ .  $\Delta E$  is taken to be the electron affinity difference between two end binaries. Assuming the perfectly random case gives, for the transition rate,

$$S(\vec{k}, \vec{k}') = \frac{2\pi}{\hbar} \cdot \frac{3\pi^2}{16N_a V} \cdot x(1-x) (\Delta E)^2 \delta(E-E') \quad (\text{A1.63})$$

where  $N_a$  is the density of alloying sites, and  $x$  is the mole fraction of the binary AC in the ternary alloy  $A_x B_{1-x} C$ .

Integrating over the final states gives the total scattering rate

$$\frac{1}{\tau_{al}} = \frac{3\sqrt{2\pi}}{8\hbar^4 N_a} \cdot x(1-x) (\Delta E)^2 (m^*)^{3/2} (1 + 2\epsilon E)^{1/2}(E) \quad (\text{A1.64})$$

As seen from Eq. (A1.63) alloy scattering is completely randomizing in the first order. Therefore,  $\cos\beta$  is determined by Eq. (A1.34).

Fig. A.10 shows the energy dependence of alloy scattering rate for  $\text{Al}_{0.2}\text{Ga}_{0.8}\text{As}$  ( $x = 0.2$ ) at  $300^\circ\text{K}$ . ( $m^* = 0.0796 m_0$ ,  $\Delta E = 0.55\text{ eV}$  and  $N_a = 2.22 \times 10^{22}\text{ cm}^{-3}$  have been used for the calculations.)

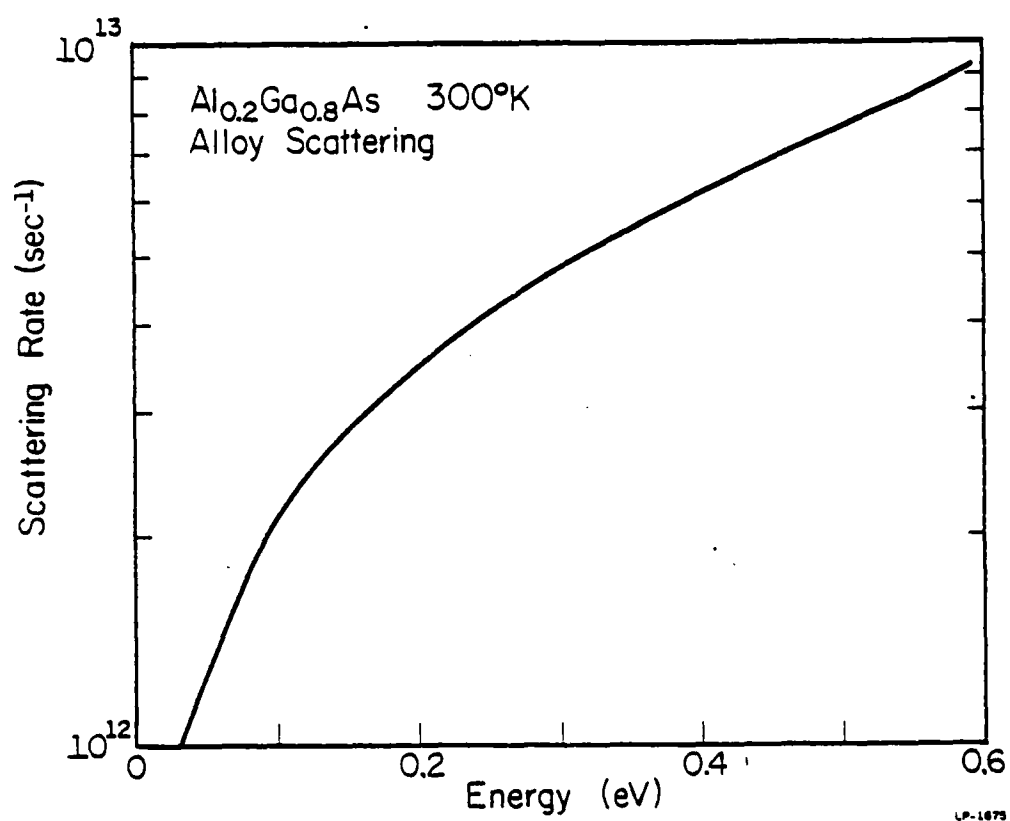


Fig. A.10. Energy dependence of random potential alloy scattering rate in the valley of Al<sub>0.2</sub>Ga<sub>0.8</sub>As (300 K). The model is by Harrison and Hauser [73].

## APPENDIX 2

## Material Parameters used in the calculations [34]

1. GaAsBulk material parameters

Lattice constant	5.642 Å
Density	5.36 g/cm <sup>3</sup>
Electron affinity	4.07 eV
Piezoelectric constant	0.16 C/m <sup>2</sup>
LO phonon energy	0.03536 eV
Longitudinal sound velocity	5.24 x 10 <sup>5</sup> cm/sec
Optical dielectric constant	10.92
Static dielectric constant	12.90

Valley-dependent material parameters

	<u>Γ(000)</u>	<u>L(111)</u>	<u>X(100)</u>
Effective mass ( $m^*/m_0$ )	0.063	0.222	0.58
Nonparabolicity (eV <sup>-1</sup> )	0.610	0.461	0.204
Energy band gap relative to valence band (eV)	1.439 (0)	1.769 (0.33)	1.961 (0.522)
Acoustic deformation potential (eV)	7.0	9.2	9.7
Optical deformation potential (eV/cm)	0	3 x 10 <sup>8</sup>	0
Optical phonon energy (eV)	---	0.0343	---
Number of equivalent valleys	1	4	3

	<u><math>\Gamma(000)</math></u>	<u><math>L(111)</math></u>	<u><math>X(100)</math></u>
Intervalley deformation potential (eV/cm)			
$\Gamma$	0	$1 \times 10^9$	$1 \times 10^9$
L	$1 \times 10^9$	$1 \times 10^9$	$5 \times 10^8$
X	$1 \times 10^9$	$5 \times 10^8$	$7 \times 10^8$
Intervalley phonon energy (eV)			
$\Gamma$	0	0.0278	0.0299
L	0.0278	0.0290	0.0293
X	0.0299	0.0293	0.0299

## 2. $\text{Al}_x\text{Ga}_{1-x}\text{As}$

Effective mass in the  $\Gamma$  valley

$$m^*/m_0 = 0.063 + 0.083x$$

Energy bandgap (eV)

$$E_g^\Gamma = 1.439 + 1.247x$$

Optical dielectric constant

$$\epsilon_\infty = 10.92 - 2.42x$$

Static dielectric constant

$$\epsilon_0 = 12.9 - 2.0x$$

LO phonon energy (eV)

$$\hbar\omega_0 = 0.03535 + 0.01464x$$

## APPENDIX 3

## Wave Vector Relations

In this appendix the vector algebra necessary to determine  $\vec{k}'$  is presented.  $\vec{k}'$  can be determined either directly by specifying the polar coordinates  $(k', \beta, \alpha)$  relative to  $\vec{k}$ , or by specifying  $\vec{q} = \vec{k}' - \vec{k}$ . We write the vector  $\vec{k}$  as (refer to Fig. A.11)

$$\vec{k} = \begin{pmatrix} k_x \\ k_y \\ k_z \end{pmatrix} = \begin{pmatrix} k \sin \theta_1 \cos \phi_1 \\ k \sin \theta_1 \sin \phi_1 \\ k \cos \theta_1 \end{pmatrix} . \quad (\text{A3.1})$$

1.  $\vec{k}'$  specified by the polar coordinates  $(k', \beta, \alpha)$  relative to  $\vec{k}$

The length of  $\vec{k}'$  is determined by energy conservation. We consider an operation which aligns the vector  $\vec{k}$  with the z-axis. This operation can be written as

$$U = Y_{-\theta_1} Z_{-\phi_1} \quad (\text{A3.2})$$

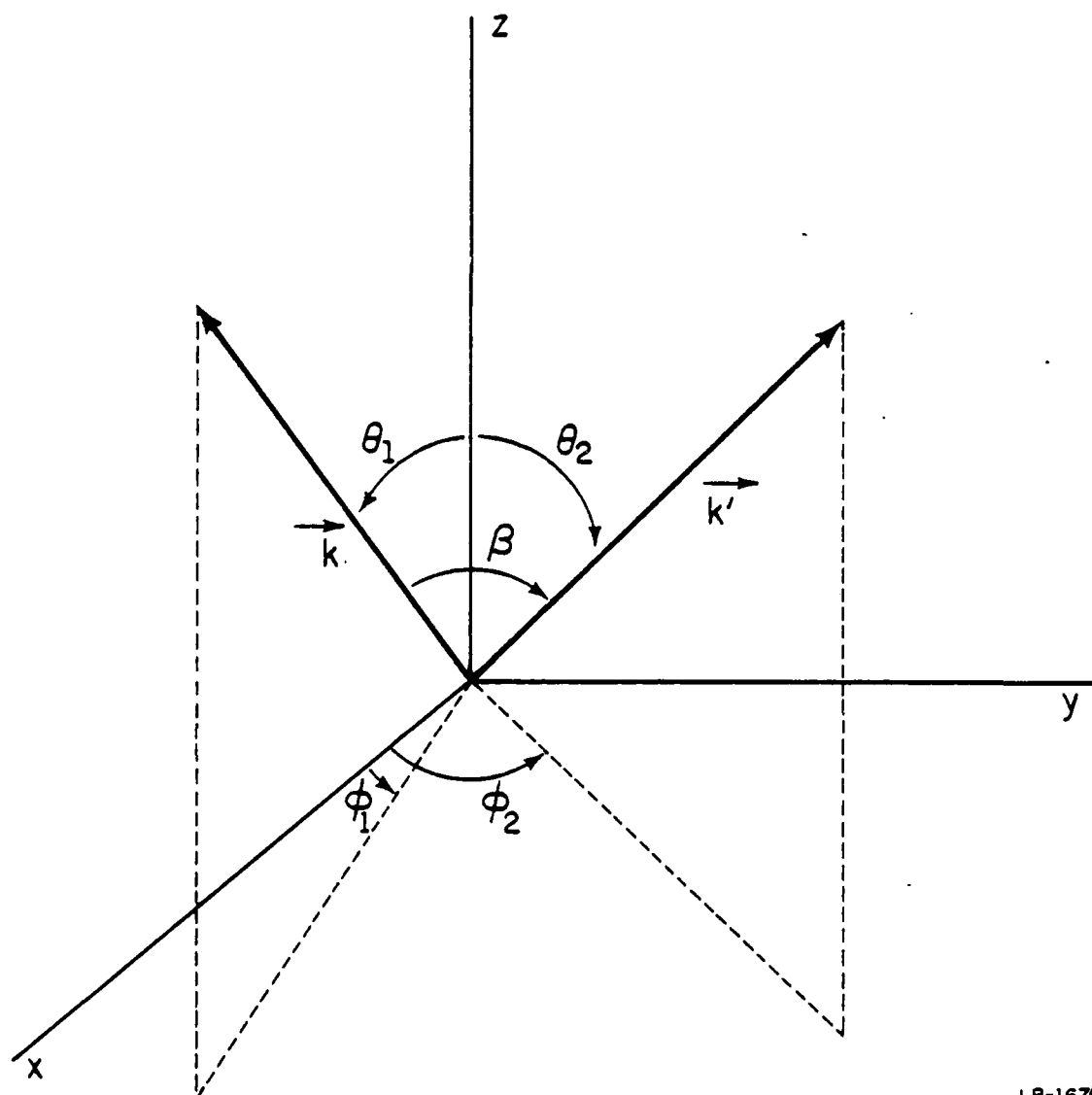
where  $Y_\theta$  represents the rotation around the y-axis with an angle  $\theta$  and  $Z_\phi$  represents the rotation around the z-axis with an angle  $\phi$ . In matrix representations these rotations can be written as

$$Y_\theta = \begin{pmatrix} \cos \theta & 0 & \sin \theta \\ 0 & 1 & 0 \\ -\sin \theta & 0 & \cos \theta \end{pmatrix} \quad (\text{A3.3})$$

$$Z_\phi = \begin{pmatrix} \cos \phi & -\sin \phi & 0 \\ \sin \phi & \cos \phi & 0 \\ 0 & 0 & 1 \end{pmatrix} . \quad (\text{A3.4})$$

Now suppose the angle  $\beta$  between  $\vec{k}$  and  $\vec{k}'$  and the azimuthal angle,  $\alpha$ , are given as in the Monte Carlo calculations. Then  $\vec{k}'$  is given by

$$\vec{k}' = U^{-1} \vec{k}'' = Z_{\phi_1} Y_{\theta_1} \vec{k}'' \quad (\text{A3.5})$$



LP-1676

Fig. A.11. Polar coordinates for electron wave vectors  $\vec{k}$  and  $\vec{k}'$ .  $\beta$  is the angle between the two vectors.



where

$$\vec{k}' = \begin{pmatrix} k' \sin\beta \cos\alpha \\ k' \sin\beta \sin\alpha \\ k' \cos\beta \end{pmatrix} \quad (\text{A3.6})$$

Performing the matrix multiplications, we obtain

$$\begin{aligned} k_x' &= k' (\cos\theta_1 \cos\phi_1 \sin\beta \cos\alpha - \sin\phi_1 \sin\beta \sin\alpha + \sin\theta_1 \cos\phi_1 \cos\beta) \\ k_y' &= k' (\cos\theta_1 \sin\phi_1 \sin\beta \cos\alpha + \cos\phi_1 \sin\beta \sin\alpha + \sin\theta_1 \sin\phi_1 \cos\beta) \\ k_z' &= k' (-\sin\theta_1 \sin\beta \cos\alpha + \cos\theta_1 \cos\beta). \end{aligned} \quad (\text{A3.7})$$

2.  $\vec{k}'$  specified by  $\vec{q} = \vec{k}' - \vec{k}$

Given the length of  $\vec{q}$  and the polar angles,  $\theta$  and  $\phi$ , relative to  $\vec{k}$ ,  $\vec{q}$  can be obtained by operating

$$Z_{\phi_1} Y_{\theta_1} = \begin{pmatrix} \cos\theta_1 \cos\phi_1 & -\sin\phi_1 & \sin\theta_1 \cos\phi_1 \\ \cos\theta_1 \sin\phi_1 & \cos\phi_1 & \sin\theta_1 \sin\phi_1 \\ -\sin\theta_1 & 0 & \cos\theta_1 \end{pmatrix} \quad (\text{A3.8})$$

to

$$q' = \begin{pmatrix} q_x' \\ q_y' \\ q_z' \end{pmatrix} = \begin{pmatrix} q \sin\theta \cos\phi \\ q \sin\theta \sin\phi \\ q \cos\theta \end{pmatrix} \quad (\text{A3.9})$$

Therefore, using  $\vec{k}' = \vec{k} + \vec{q}$ , we have

$$\begin{aligned} k_x' &= q_x' \cos\theta_1 \cos\phi_1 - q_y' \sin\phi_1 + (q_z' + k) \sin\theta_1 \cos\phi_1 \\ k_y' &= q_x' \cos\theta_1 \sin\phi_1 + q_y' \cos\phi_1 + (q_z' + k) \sin\theta_1 \sin\phi_1 \\ k_z' &= -q_x' \sin\theta_1 + (q_z' + k) \cos\theta_1. \end{aligned} \quad (\text{A3.10})$$

## VITA

Hisashi Shichijo was born on October 24, 1952 in Kagawa, Japan. He attended the University of Tokyo, and graduated with a Bachelor of Engineering degree in Electrical Engineering in March, 1976.

He attended the University of Illinois at Urbana-Champaign during the academic year 1974-1975 and returned to the University of Illinois in August, 1976. He received a Master of Science degree in Electrical Engineering in January, 1978. He has served as a teaching assistant in the Department of Electrical Engineering of the University of Illinois, and a research assistant in both the Electrical Engineering Research Laboratory and the Coordinated Science Laboratory of the University of Illinois.

Mr. Shichijo is a member of Phi Kappa Phi, the American Physical Society, the Institute of Electrical and Electronics Engineers, the Japan Society of Applied Physics, and the Physical Society of Japan. He is currently a candidate for the degree of Doctor of Philosophy from the University of Illinois.